

AD-A116 034

VRIJE UNIVERSITEIT BRUSSEL (BELGIUM) DEPT OF FLUID ME--ETC F/6 20/4

TURBULENCE STRUCTURE IN THE WAKE OF AN OSCILLATING AIRFOIL. (U)

NOV 81 J DE RUYCK, C HIRSCH

DAJA37-80-C-0367

UNCLASSIFIED

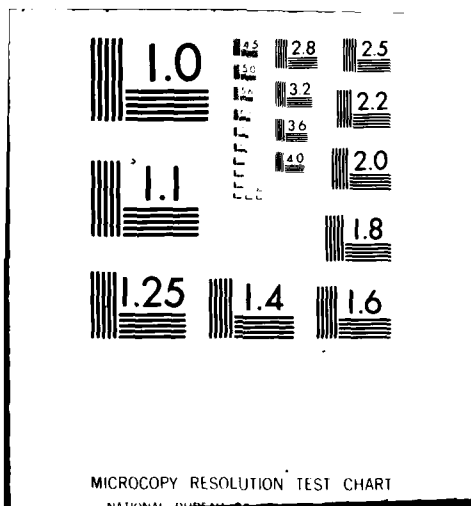
VUB-STR-12

NL

1-1  
A  
0101



END  
DATE  
FILMED  
7-82  
DTIC



AD A116034

DTIC FILE COPY

12

AD

# **TURBULENCE STRUCTURE IN THE WAKE OF AN OSCILLATING AIRFOIL**

Final Technical Report  
by

J. DE RUYCK and Ch. HIRSCH

Report VUB-STR-12

November 1981

DTIC  
ELECTE  
JUN 24 1982  
S D  
B

United States Army

RESEARCH & STANDARDIZATION GROUP (EUROPE)

London, England

Contract number DA-JA-37-80-C-0367

Contractor : Vrije Universiteit Brussel  
Dept. of Fluid Mechanics

Approved for Public Release - Distribution Unlimited

AD

# **TURBULENCE STRUCTURE IN THE WAKE OF AN OSCILLATING AIRFOIL**

**Final Technical Report  
by**

**J. DE RUYCK and Ch. HIRSCH**

**Report VUB-STR-12**

**November 1981**

**United States Army**

**RESEARCH & STANDARDIZATION GROUP (EUROPE)**

**London, England**

**Contract number DA-JA-37-80-C-0367**

**Contractor : Vrije Universiteit Brussel  
Dept. of Fluid Mechanics**

**Approved for Public Release - Distribution Unlimited**

UNCLASSIFIED

SECURITY CLASSIFICATION OF THIS PAGE (When Data Entered)

R&amp;D 2835-AN

REPORT DOCUMENTATION PAGE		READ INSTRUCTIONS BEFORE COMPLETING FORM
1. REPORT NUMBER	2. GOVT ACCESSION NO.	3. RECIPIENT'S CATALOG NUMBER
	AD-A116034	
4. TITLE (and Subtitle)	5. TYPE OF REPORT & PERIOD COVERED	
Turbulence Structure in the Wake of an Oscillating Airfoil	Final Technical Report Jul 80 - Sep 81	
	6. PERFORMING ORG. REPORT NUMBER	
7. AUTHOR(s)	8. CONTRACT OR GRANT NUMBER(s)	
J. De Ruyck and C. Hirsch	DAJA37-80-C-0367	
9. PERFORMING ORGANIZATION NAME AND ADDRESS	10. PROGRAM ELEMENT, PROJECT, TASK AREA & WORK UNIT NUMBERS	
Vrije Universiteit Brussel Belgium	6.11.02A 1T161102BH57-06	
11. CONTROLLING OFFICE NAME AND ADDRESS	12. REPORT DATE	
USARDSG-UK Box 65, FPO NY 09510	November 1981	
	13. NUMBER OF PAGES	
	50	
14. MONITORING AGENCY NAME & ADDRESS (if different from Controlling Office)	15. SECURITY CLASS. (of this report)	
	Unclassified	
	15a. DECLASSIFICATION/DOWNGRADING SCHEDULE	
16. DISTRIBUTION STATEMENT (of this Report)		
Approved for Public Release; distribution unlimited		
17. DISTRIBUTION STATEMENT (of the abstract entered in Block 20, if different from Report)		
18. SUPPLEMENTARY NOTES		
19. KEY WORDS (Continue on reverse side if necessary and identify by block number)		
Non-steady wakes and boundary layers Non-steady turbulence		
20. ABSTRACT (Continue on reverse side if necessary and identify by block number)		
<p>The main objective of the present study is to provide experimental information about turbulence structures in unsteady flow fields.</p> <p>Measurements were made in the wake of a NACA 0012 airfoil oscillating in pitch around an axis at 25% chord distance from the leading edge with a sinusoidal motion. Instantaneous profiles of velocity and all non-zero Reynolds stresses are determined at 48 phase angles within the oscillation.</p>		

UNCLASSIFIED

SECURITY CLASSIFICATION OF THIS PAGE (When Data Entered)

UNCLASSIFIED

SECURITY CLASSIFICATION OF THIS PAGE(When Data Entered)

20. Contd

period. Measurements were made at .7, 2, 5, 10 and 20% chord downstream of the trailing edge. Various incidences, from zero to just above stall limit, various amplitudes and frequencies were considered. The reduced frequency ( $\omega c/2U$ ) ranges from 0 to 1.2 at a chord Reynolds number of 300,000.

An improved rotating slanted hot wire anemometer technique is used for the determination of all non-zero Reynolds stresses.

A micro processor controlled system samples, digitizes and records on tape the hot wire anemometer signal as well as the wing and probe position as functions of time. Instantaneous profiles are reconstructed through ensemble and conditional averaging techniques.

Results are presented and compared with steady state values. Detailed results are made available on magnetic tape.

Accession For	
NTIS GRA&I	<input checked="checked" type="checkbox"/>
DTIC TAB	<input type="checkbox"/>
Unannounced	<input type="checkbox"/>
Justification	
By	
Distribution/	
Availability Codes	
Avail and/or	
Dist	Special
A	

DTIC  
COPY  
INSPECTED  
2

UNCLASSIFIED

SECURITY CLASSIFICATION OF THIS PAGE(When Data Entered)

# TURBULENCE STRUCTURE IN THE WAKE OF AN OSCILLATING AIRFOIL

## ABSTRACT

The main objective of the present study is to provide experimental information about turbulence structures in unsteady flow fields.

Measurements were made in the wake of a NACA 0012 airfoil oscillating in pitch around an axis at 25% chord distance from the leading edge with a sinusoidal motion. Instantaneous profiles of velocity and all non-zero Reynolds stresses are determined at 48 phase angles within the oscillation period. Measurements were made at .7, 2, 5, 10 and 20 % chord downstream of the trailing edge. Various incidences, from zero to just above stall limit, various amplitudes and frequencies were considered. The reduced frequency ( $\omega c/2U$ ) ranges from 0 to 1.2 at a chord Reynolds number of 300,000.

An improved rotating slanted hot wire anemometer technique is used for the determination of all non-zero Reynolds stresses.

A micro processor controlled system samples, digitizes and records on tape the hot wire anemometer signal as well as the wing and probe position as functions of time. Instantaneous profiles are reconstructed through ensemble and conditional averaging techniques.

Results are presented and compared with steady state values. Detailed results are made available on magnetic tape.

## CONTENTS

1. Introduction	2
2. Previous work	3
3. Experimental set up	4
3.1 Introduction	4
3.2 Oscillating airfoil	4
3.3 Probe support	5
3.4 Hot wire apparatus	5
3.5 Data acquisition facility	5
4. Rotating slanted hot wire measurement techn	5
4.1 Introduction	5
4.2 Mean flow parameters	6
4.3 Determination of Reynolds stresses	8
4.4 Optimal probe positioning	10
5. Data reduction	11
5.1 Introduction	11
5.2 Ensemble average	11
5.3 Instantaneous profiles	12
5.4 Conditional averaging	12
5.5 Summary and computer requirements	12
6. Selection of test cases	13
6.1 Oscillation amplitude	13
6.2 Mean incidence	13
6.3 Oscillation frequency	14
7. Results	14
7.1 Output variables	14
7.2 Steady state results	16
7.3 zero mean incidence cases	17
7.4 5 degrees mean incidence cases	17
7.5 Stall onset test cases	18
8. Conclusions and future work	19

# NOMENCLATURE

di	incidence increase
E	hot wire anemometer voltage
H	wake shape factor
i	instantaneous incidence
k	chord frequency coefficient ( $\omega c/2Q_\infty$ )
m	Bruun's power
Q	absolute velocity
Q <sub>eff</sub>	effective cooling velocity
r	distance from oscillation axis
s	Reynolds stress
u	meanstream velocity fluctuation
v	velocity fluctuation normal to meanstream and span
w	spanwise velocity fluctuation
V <sub>c</sub>	chordwise velocity
V <sub>p</sub>	pitchwise velocity
y	pitchwise coordinate
$\alpha_0$	wire slanting angle
$\alpha_{p*}$	probe rotation angle
$\delta$	wake displacement thickness
$\theta$	wake momentum thickness
$\varphi$	probe inclination angle
$\psi$	flow angle, phase angle
$\phi$	yaw angle
'	rms of fluctuations
-	(periodic) time averaged value
(r)	relative

## 1. INTRODUCTION

Unsteady phenomena appear in many fluid-dynamic systems as a basic event or as a perturbation of a steady state situation. In external aerodynamics for example, the flow along airfoils is often strongly unsteady due to the motion or the vibrations (flutter) of the blades (e.g. helicopter blades, propeller flows, Darrieus-type windmills). In such situations the increasing demand for higher performance requires a more basic understanding of the unsteady phenomena in order to be able to improve the existing design methods.

Although many aspects of unsteady flows can be handled by linear, or non-linear inviscid theory, important classes of phenomena are dominated by, or strongly dependent on viscous effects such as dynamic stall, stall flutter or the turbulence structure of wakes from rotating blades in turbomachines, which can strongly influence the flow on the downstream stator.

The actual spectacular development of computational methods to solve steady and unsteady flows has reached a stage where two-dimensional, time averaged Navier-Stokes equations can be solved within reasonable cost and storage requirements, for both steady and unsteady situations [30]. The comparison of calculated Navier-Stokes solutions and experimental data is however still limited mainly by the lack of detailed knowledge of the turbulence input to the equations [20]. More particularly in the case of unsteady boundary layers, the question of the influence of the unsteadiness on the turbulence structure is still unanswered.

At the present time several experiments are undertaken in this field : experiments on flat plates [6-9, 14, 15, 23-26, 31], airfoils [17, 27, 28] or diffusers [29] where the boundary layers are exposed to an oscillating pressure gradient. Several experiments are made on unsteady jets [32] and on pitching or plunging airfoils [4, 12, 13, 18, 19, 22]. In the latter case experiments are mainly dealing with unsteady airloads [4, 22], flow visualisation [18, 19] and to some extent with velocity and turbulence distributions [12, 13].



The objective of our research is therefore to provide detailed information about the turbulence structure in wakes and boundary layers of an oscillating airfoil by comparing mean velocities and all components of the Reynolds stress tensor with the corresponding steady state values.

In order to concentrate on the turbulence properties, the research will be limited to incompressible flows without heat transfer.

In the present report, the measurement and data reduction techniques are detailed and all available results of the experimental work done in the wake of the considered airfoil are presented and discussed.

## 2. PREVIOUS WORK

Some excellent reviews on the subject of unsteady flows can be mentioned : the Freeman lecture by Mc Croskey [21] which is devoted to unsteady flows in general, reviews of Telionis [33] which are mainly devoted to unsteady boundary layers and a recent review of experimental work done in this field by L.W. Carr [3]. The authors insist on the urgent need for experimental data on turbulence effects in unsteady flows both as basic data - comparison with calculations and turbulence models as well as providing insight into the physical mechanism of energy exchange between the random turbulent motion and the organized periodic flow.

In the following, more details are given about past work done which is closely related to the present experiments, namely work done on unsteady boundary layers and/or wakes on flat plates and airfoils.

Most of the flat plate experiments are done on a fixed plate with an external oscillating flow. Detailed experiments are available with and without adverse pressure gradient in unseparated and to some extent in separated flows. Frequency coefficients based on the boundary layer thickness range from 0 to .24 [23] and oscillation amplitudes reach 50% of the outer flow [8]. Data of velocities, two or three Reynolds stresses, static pressure and skin friction are available. Table 1 gives an overview of work done in this field with some details about each experiment. This table is not believed to be complete but it gives an idea of the type of experiments and results available in the open literature.

The flat plate experiments can be considered as a more fundamental research whereas more direct data are needed about current flow types such as flows around common used airfoils. Experiments on unsteady flows around airfoils are in general performed using an oscillating airfoil (pitching or plunging) in a steady free stream, whereas the flat plates are generally fixed. As experiments with a fixed airfoil in an oscillating external flow one can mention the work of Satyarayana [27] and of Saxena et al [28]. Saxena et al made experiments at angles of attack close to the stall limit. In these experiments pressure distributions and velocity profiles are presented, no Reynolds stresses are given.

In the case of an oscillating airfoil extensive experiments were made for the determination of unsteady airloads by Mc Croskey and his collaborators. A summary and discussion of these experiments are given in [22]. Several profile shapes were used for these investigations. Unsteady pressures and airloads are searched for various combinations of Mach number (up to .3), frequency ( $k=2$ ), oscillation amplitude, mean incidence, Reynolds number (up to 4,000,000) and airfoil shape (NACA 0012, Vertol vr-7, NLR 7301). No velocities or detailed turbulences were measured. Four different flow regimes were considered : no stall, stall onset, light and deep dynamic stall.

A second type of experiments on oscillating airfoils is performed by Mc Alister and L.W. Carr [18,19]. The experiments consist in visualisations at low Reynolds number (21,000) of the dynamic stalled flow around a pitching NACA 0012 airfoil. The airfoil oscillated from 0 to 20 degrees incidence at  $k=.25$ .

A last type of experiment which can be mentioned is performed by C.M. Ho and S.H. Chen [12,13]. The purpose of this experiment is to analyse the flow in the vicinity of the trailing edge of a plunging airfoil in a steady free stream.

Measurements were made with 5 X-wires in the wake of the airfoil.

Hence, in the case of a pitching airfoil little or no detailed information about velocity and turbulence is available at the present time. It should be observed that even in the steady state case, such information is not profuse. Data which are closely related with the present investigations are presented by J. C. Yu [34]. In this reference, velocity and three Reynolds stress profiles are presented at 16 chordwise positions in the vicinity of the trailing edge of a NACA 63-012 airfoil ( $x/c$  from .9 to 1.1).

Finally it should be mentioned that methods for the theoretical prediction of the aforementioned flow types are in full development. Some recent works can be mentioned. S. B. R. Kottapalli and G. A. Pierce [17] presented an analytical study of the drag on an oscillating airfoil. The turbulence input was based on the Cebeci-Smith eddy viscosity model. T. Cebeci presented a paper [5] dealing with the calculation of boundary layer characteristics on an oscillating airfoil, including flow reversal. J. Shamroth [30] applied a time dependent compressible turbulent Navier-Stokes analysis to the oscillating flow field problem. The test Reynolds number was 2,600,000. Turbulence models are based on a turbulence energy equation. Close to the present investigations is the work of Baker and Yu [1] where calculated detailed turbulence and velocity profiles are presented and compared with Yu's data [34]. This is however limited to the steady state case.

Although probably incomplete, the present review situates well the present work between previous and actual work done in the field of unsteady aerodynamics. The present detailed data are still rare although required by the actual development of computational techniques.

### 3. EXPERIMENTAL SET UP

#### 3.1 Introduction

The complete experimental set up is summarized on fig 1. The oscillating airfoil with the driving mechanism are represented on top of the figure. A pitot tube is mounted on the probe support close to the hot wire for calibration purposes. A step motor allows for the pitchwise translation of the probe which rotates around its axis through a second step motor. A single 45 degrees slanted hot wire is mounted on the probe support. This rotating wire allows for the determination of mean flow as well as all non-zero Reynolds stresses.

Four signals are controlled from outside the windtunnel, a triggering signal from the driving mechanism, the hot wire signal and the probe translation and rotation controls. The rotational position is kept constant during probe translation and is therefore not recorded continuously but written manually on the tape at beginning of each probe translation. Other signals are recorded.

Sampled and digitized data are simultaneously written on tape, while one of the recorded signals can be observed on a scope after DAC conversion. The obtained records are next forwarded to the computer centre for processing. Measurement of new and processing of previous experiments occur simultaneously, which represents an important time gain.

#### 3.2 Oscillating airfoil

A 60 cm chord NACA 0012 airfoil is used for the experimental set up. This airfoil is mounted in a 2 by 1 meter test section in one of the VUB blowdown windtunnels, where speeds of 17 m/s are reached at a free stream turbulence level less than .5%.

Kraemer's rule was used to design a tripping wire which is fixed at 10% chord distance from the leading edge. The diameter of the wire is  $d = 2$  mm where

$$d > 900 \frac{Q}{V^2} \quad (1)$$

The airfoil is excited by a 300 Watt motor reductor which allows for an oscillating frequency up to 8 Hz at 5 degrees oscillation amplitude. Sinusoidal pulsation is obtained using a crank-connecting rod mechanism, where a 1 meter long connecting rod allows for a motion which is sinusoidal within a few percent distortion. The connecting rod is close to the lower wind tunnel wall. Speed is kept constant within one oscillation period by regulation of the motor shaft velocity (0-5000 rpm). The crank axis delivers a one bit trigger signal which is recorded simultaneously on tape.

### 3.3 Probe support

The rotating hot wire is mounted on a support fixed in the wind tunnel. A step motor allows for a very slow and constant speed translation of the hot wire probe support in the pitchwise direction across the wake area. The resolution of the positioning is less than .002 % chord (.01 mm) in the pitchwise direction and is about .1 % chord in the chordwise direction. The probe itself can rotate around its axis through a 48 positions step motor (only 12 are used). The excentricity of the sensor can be reduced to about .01 % chord (.05 mm).

### 3.4 Hot wire apparatus

The used hot wire is a 45 degrees slanted DISA gold plated hot wire type 55P02. The sensor diameter is .005 mm and the length is 1.25 mm. The wire is connected to a TSI CTA anemometer bridge. No linearisation of the hot wire signal is used in order to avoid phase distortion.

The calibration of the wire occurs in situ by use of a pitot tube. The operating free stream velocity when calibrating is considered to have a constant value of 11.5 m/s, although small variations from this mean value are observed over the long measurement periods. This approximation is done in order to have a coherent reference value over all the experiments.

### 3.5 Data acquisition facility

The data acquisition facility of the VUB Fluid Mechanics Department is an essential and unique facility for the present investigation.

The aim of this facility is to sample, digitize and write on tape up to 8 analog or digital input signals. Each analog signal (e.g. hot wire anemometer voltage) is filtered and DC amplified by the system before being sampled, digitized through a 10-bit ADC and recorded on tape. All acquisition parameters such as sample frequency, cut-off filters, run time, formatting of digitized data are simply read in from a tty, which makes the system flexible and widely applicable. The maximum data transfer rate is about 150 kHz. Comments can be added on the tape from the tty.

A constant DC offset is subtracted from the hot wire anemometer signal before being DC amplified, in order to have an acceptable resolution for the fluctuating amplitudes.

A 1 bit wing position reference signal is combined with a 9 bit probe position coordinate and recorded as one 10 bit signal on the tape

A detailed description of this datalogger can be found in [11].

## 4. ROTATING SLANTED HOT WIRE MEASUREMENT TECHNIQUE

### 4.1 Introduction

Two methods for the determination of Reynolds stresses in a flow field are mainly discerned. In the first an X-wire is set up in such a way that the wires are sensitive to the selected turbulent quantities. In the second method a single normal or slanted hot wire is used and in order to obtain sensitivity on the

different turbulence velocities, it is rotated around its probe support.

The latter method has some specific advantages over the X-wire technique. It allows for the determination of both mean flow and all turbulent quantities, which is not the case with an X-wire. Moreover, a less complicated electronic set up is needed and the data are related to a much smaller area.

The method as used in the present study has its base in the works of Kool and De Grande [10,16]. A special attention was however paid to the choice of the probe positioning in order to avoid prong effects as much as possible and to simultaneously increase the resolution on the different quantities to be measured.

The geometry of the wire is defined on fig 2.  $\varphi$  and  $\psi$  are the spherical coordinates which define the flow direction in the absolute frame.  $\alpha_0$  denotes the slanting angle and  $\alpha_p$  defines the probe rotation. The yaw angle  $\phi$  is defined as the angle between the velocity vector and the plane normal to the wire. This angle can be expressed as function of  $\alpha_0$ ,  $\alpha_p$ ,  $\varphi$  and  $\psi$  through the relationship

$$\begin{aligned} \sin\phi &= \sin\alpha_0 \cos\psi \cos\varphi \\ &+ \cos\alpha_0 \cos\psi \sin\varphi \cos\alpha_p \\ &+ \cos\alpha_0 \sin\psi \sin\alpha_p \end{aligned} \quad (2)$$

Eq (2) can be obtained through the scalar product of unit vectors chosen along the hot wire and along the velocity vector.

#### 4.2 Mean flow parameters

As the wire is rotated around its support axis for different  $\alpha_p$  values, variations of the yaw angle and hence of anemometer voltage are observed. From these variations it is possible to determine the flow direction and magnitude.

The anemometer voltage  $E$  and the 'effective' cooling velocity  $Q_{eff}$  ( $<Q$  when  $\phi$  non-zero) are related through King's law by

$$E^2 = A + B Q_{eff}^C \quad (3)$$

A, B and C are determined from a in situ calibration using a pitot tube. The cooling velocity  $Q_{eff}$  depends on the velocity magnitude  $Q$  and the yaw angle  $\phi$ . A simple cosine law can be used as a first approximation when relating  $Q_{eff}$  to  $Q$ .

$$Q_{eff} = Q \cos\phi \quad (4)$$

This law is valid in absence of prong effects for high wire length over diameter ratio's (400) and for values of  $\phi$  less than about 45 degrees [2]. At higher values of  $\phi$  (or lower  $l/d$  ratio), the forced convection no more obeys this law and a simple correction can be introduced through Bruun's law [2]

$$Q_{eff} = Q \cos^m\phi \quad (5)$$

This relation can be used for values of  $\phi$  up to 70 degr [2].

As the yaw angle goes to 90 degr, the velocity becomes tangential to the wire and eqs (4) and (5) would predict  $Q_{eff} = 0$ . This is an unrealistic behaviour since the wire is still cooled by the flow in this situation. Since such high values of yaw angle are expected in the present study, eqs (4) and (5) are corrected to the classical law

$$Q_{eff} = Q (\cos^2\phi + k^2 \sin^2\phi)^{1/2} \quad (6)$$

Kool [10,16] introduced corrections to eq (6) in order to take account of prong effects and asymmetry in the wire responses. These effects will however be avoided

through an adequate probe positioning and by continuous calibration for all probe positions.

It is to be observed that eqs (5) and (6) are closely related since

$$\begin{aligned} Q_{eff}^2 &= Q^2 (\cos^2 \phi)^m \\ &= Q^2 (1 - \sin^2 \phi)^m \\ &\approx (Q_{eff})_{\phi=0}^2 + \left( \frac{\partial Q_{eff}^2}{\partial \sin^2 \phi} \right)_{\phi=0} m \sin^2 \phi \\ Q_{eff} &\approx Q (1 - m \sin^2 \phi)^{1/2} \end{aligned} \quad (2)$$

Hence, from eqs (6) and (7)

$$k^2 \approx 1 - m \quad (8)$$

Eq (7) will further be used instead of eq (6), for convenience.

From the measured anemometer voltages  $E$ , or the corresponding values of  $Q_{eff}$  at different  $\alpha_p$  values, one has to determine the best values of  $\psi$ ,  $\phi$ ,  $m$  and  $Q$ . This is done by expressing the least squares condition as follows

$$\sum_{\alpha_p} [(Q_{eff}/Q)^2 + m \sin^2 \phi - 1]^2 \text{ is minimum} \quad (9)$$

From eq (9) it follows that

$$1/Q^2 \sum Q_{eff}^4 + m \sum \sin^2 \phi Q_{eff}^2 = \sum Q_{eff}^2 \quad (10)$$

$$1/Q^2 \sum Q_{eff}^2 \sin^2 \phi + m \sum \sin^4 \phi = \sum \sin^2 \phi \quad (11)$$

$$\sum [(Q_{eff}/Q)^2 + m \sin^2 \phi - 1] \sin \phi \cos \phi \frac{\partial \phi}{\partial \psi} = 0 \quad (12)$$

$$\sum [(Q_{eff}/Q)^2 + m \sin^2 \phi - 1] \sin \phi \cos \phi \frac{\partial \phi}{\partial \psi} = 0 \quad (13)$$

Since eqs (10) and (11) are linear in  $1/Q$  and  $m$ , it is possible to express eqs (10) to (13) as follows

$$f(\phi, \psi) = 0 \quad (14)$$

$$g(\phi, \psi) = 0 \quad (15)$$

Since in the present study the considered mean flow can be considered as two dimensional, at least one of the two angles  $\psi$  or  $\phi$  can be considered as known. The surfaces of two dimensional flow will be defined by  $\psi = \psi_0$ , where  $\psi_0$  is to be chosen (see 4.4). Hence eq (12) can be dropped and the least squares fit can be reduced to the solution of one implicit equation  $f(\phi)=0$ . This is a periodic function in  $\psi$  which in general has 4 roots (sometimes 8), as illustrated on fig 3. Two of the solutions correspond with maximum values of the sum of squares and can be rejected, the two other roots lie at 180 degrees interval and hence give the flow direction, but not the flow sense, which was to be expected since the wire cannot know from which side it is cooled. This point will further be discussed section 7

A first approximation for  $\psi$  when solving  $f(\psi)=0$  can be found from

$$\operatorname{tg} \psi = \sin \frac{\sum (Q-\bar{Q}) \sin \alpha_p}{\sum (Q-\bar{Q}) \cos \alpha_p} \quad (16)$$

On fig 4, an example is given of the experimental and fitted directional responses of  $Q_{eff}$  as function of  $\alpha_p$ , figs 3 and 4 are based on the same test data.

#### 4.3 Determination of Reynolds stresses

Flow turbulence can be observed by a hot wire thanks to its high frequency response (up to 20 kHz). The intensity of the anemometer voltage fluctuations is quantified by

$$E' = [(\overline{E-E})^2]^{1/2} \quad (17)$$

where  $\bar{E}$  denotes the time averaged value of  $E(t)$  and  $E'$  the rms of the voltage fluctuations. From this rms value, one can estimate  $Q_{eff}'$ , the rms of the fluctuations of  $Q_{eff}$ . Differentiation of eq (3) yields

$$dQ_{eff} = \left( \frac{E^2 - A}{B} \right)^{1/2} - 1 \frac{2E}{CB} dE \quad (18)$$

$$\overline{(dQ_{eff})^2} = \left( \frac{\bar{E}^2 - A}{B} \right)^{2/2} - 2 \left( \frac{2\bar{E}}{CB} \right)^2 \overline{(dE)^2} \quad (19)$$

Neglecting second order terms, eq (19) may be rewritten as

$$Q'_{eff} = \left( \frac{\bar{E}^2 - A}{B} \right)^{1/2} - 1 \frac{2\bar{E}}{CB} E' \quad (20)$$

When obtaining eq (19), it was assumed that the fluctuations  $Q_{eff}'$  and  $E'$  are small enough compared with the averaged values  $Q_{eff}$  and  $E$ . This linearisation for 'small' turbulence (<10%) will be applied in all the following.

The velocity fluctuations from the mean velocity  $Q$  are denoted by  $u$ ,  $v$  and  $w$ , where  $u$  is directed in the mean flow direction, while  $v$  and  $w$  are defined as respectively tangential and normal to the two dimensional plane  $\psi = \psi$  (see fig 2). Hence, these components can be written as, according to the linearisation

$$u = dQ \quad (21)$$

$$v = Q d\psi \quad (22)$$

$$w = Q \cos \psi d\psi \quad (23)$$

Differentiation of eq (6) yields

$$\begin{aligned} dQ_{eff} &= R_U dQ + Q \left( \frac{\partial R_U}{\partial \psi} d\psi + \frac{\partial R_U}{\partial \phi} d\phi \right) \\ &= R_U u + \frac{\partial R_U}{\partial \psi} v + \frac{1}{\cos \psi} \frac{\partial R_U}{\partial \phi} w \end{aligned} \quad (24)$$

where

$$R_U = (1 - m \sin^2 \phi)^{1/2} \quad (30)$$

$$\frac{\partial A_U}{\partial \psi} = -m \frac{\sin \phi}{A_U} \cos \phi \frac{\partial \phi}{\partial \psi} \quad (25)$$

$$\frac{\partial A_U}{\partial \phi} = -m \frac{\sin \phi}{A_U} \cos \phi \frac{\partial \phi}{\partial \phi} \quad (26)$$

and

$$\begin{aligned} \cos \phi \frac{\partial \phi}{\partial \psi} = & -\sin \alpha_0 \sin \psi \cos \psi - \cos \alpha_0 \sin \psi \sin \psi \cos \alpha_p \\ & + \cos \alpha_0 \cos \psi \sin \alpha_p \end{aligned} \quad (27)$$

$$\cos \phi \frac{\partial \phi}{\partial \phi} = -\sin \alpha_0 \cos \psi \sin \psi + \cos \alpha_0 \cos \psi \cos \psi \cos \alpha_p \quad (28)$$

From eqs (24) to (28), one can write

$$dQ_{eff} = A_U U + A_V V + A_W W \quad (29)$$

where

$$A_U = (1 - m \sin^2 \phi)^{1/2} \quad (30)$$

$$\begin{aligned} A_V = -m \frac{\sin \phi}{A_U} (\cos \alpha_0 \cos \psi \sin \alpha_p - \sin \alpha_0 \sin \psi \cos \psi \\ - \cos \alpha_0 \sin \psi \sin \psi \cos \alpha_p) \end{aligned} \quad (31)$$

$$A_W = -m \frac{\sin \phi}{A_U} (\cos \alpha_0 \cos \psi \cos \alpha_p - \sin \alpha_0 \sin \psi) \quad (32)$$

Squaring and time averaging of eq (29) yields

$$\begin{aligned} \overline{(dQ_{eff})^2} = & \overline{(A_U U)^2} + \overline{(A_V V)^2} + \overline{(A_W W)^2} \\ & + 2\overline{A_U A_V UV} + 2\overline{A_U A_W UW} + 2\overline{A_V A_W VW} \end{aligned} \quad (33)$$

According to the linearisation assumption, this equation can be rewritten as

$$\begin{aligned} Q_{eff}^2 = & A_U^2 U^2 + A_V^2 V^2 + A_W^2 W^2 \\ & + 2A_U A_V \overline{UV} + 2A_U A_W \overline{UW} + 2A_V A_W \overline{VW} \end{aligned} \quad (34)$$

In eq (34) all six components of the Reynolds stress tensor appear, while all the coefficients and the l.h.s. are known values for each rotational probe position. Hence, at least six probe positions allow for the determination of all six Reynolds stresses, as far as these positions are chosen adequately. In practice, more than six positions are used and the best values of the stresses are obtained by a least squares fit. This fit is performed as follows.

Eq (34) is rewritten as

$$Q_{eff}^2 - \sum_{j=1}^6 a_j s_j = 0 \quad (35)$$

where  $s_j$  denote the Reynolds stresses and  $a_j$  the corresponding coefficients in eq (34). The least squares condition implies

$$\sum_{\alpha_p} (Q_{eff}^2 - \sum_{j=1}^6 a_j s_j)^2 \text{ is minimum} \quad (36)$$

This is satisfied when

$$\begin{aligned} \sum_{\alpha_p} a_1 (\sum_j a_j s_j - Q_{eff}^2) &= 0 \\ \dots \dots \dots \\ \sum_{\alpha_p} a_6 (\sum_j a_j s_j - Q_{eff}^2) &= 0 \end{aligned} \quad (37)$$

These 6 equations can be written as

$$\sum_j b_{ij} s_j = c_i \quad i = 1, 6 \quad (38)$$

or

$$[B](S) = (C) \quad (39)$$

where

$$b_{ij} = \sum_{\alpha_p} a_i a_j \quad (40)$$

$$c_i = \sum_{\alpha_p} a_i Q_{eff}^2 \quad (41)$$

The stresses  $s_j$  are finally found from

$$(S) = [B]^{-1}(C) \quad (42)$$

In the present study the flow is basically two dimensional and  $uw$  and  $vw$  can therefore be considered as neglectable. Hence, the rank of  $[B]$ ,  $(S)$  and  $(C)$  is reduced to 4.

On fig 4 an experimental and fitted directional response of  $Q_{eff}'$  is illustrated.

#### 4.4 Optimal probe positioning

When choosing the probe positioning with respect to the expected flow directions, three parameters are to be determined: the inclination  $\varphi$ , a main value for the flow angle  $\psi$  and the range of  $\alpha$ , over which the probe will be rotated. Two criteria are to be considered when choosing these parameters: prong effects are to be avoided as much as possible and the wire must be sensitive to all the searched parameters.

Prong effects can best be avoided by choosing the probe axis parallel to the expected velocity direction ( $\varphi = \psi = 0$ ), while they induce important errors as  $\varphi$  or  $\psi$



reach 90 degrees or more [2, 10, 16] (probe axis normal to velocity). The position  $\varphi = \psi = 0$  is however a singular situation since both determinants of eqs (10)-(11) for the main flow and of [B] for the Reynolds stresses become zero. Hence, an intermediate solution is to be chosen.

This choice is based on an analysis of  $[B]^{-1}$ . Since the components of [B] are sums over trigonometric functions, the order of magnitude of its components is 1. The ranges of  $\varphi$ ,  $\psi$  and  $\alpha_p$  will be chosen in such a way that all components of  $[B]^{-1}$  have this same order of magnitude (10 different components, [B] being symmetric).

An analytical expression for these components has not been found and the analysis is therefore based on plots of these 10 components as functions of  $\varphi$  and  $\psi$ . On figs 5 to 9, logarithmic plots of the moduli of the components are made. On figs 5 and 6, one can observe the behaviour of  $[B]^{-1}$  as  $\varphi$  resp.  $\psi$  are increased from 0 to 45 degrees. When comparing these figures it appears that the best behaviour is found when choosing  $\varphi = 0$ . At a value  $\psi = 0$  and  $\varphi = 15$  degr, the largest component has the desired order of magnitude (fig 5), while at  $\varphi = 0$  (fig 6), this magnitude is still 10 at a flow angle of 30 degrees. At higher values of  $\varphi$  and  $\psi$ , it is no more possible to rotate the wire over 360 degrees without masking the wire by one of the prongs. Probe rotation is then limited to 180 degrees in order to avoid too important prong effects. On figs 7 and 8 are plotted the  $[B]^{-1}$  components at 180 degr rotation for a probe axis perpendicular to the flow ( $\varphi$  or  $\psi = 90$  degr). From these figures it appears that besides the prong effects, a bad behaviour is found for  $[B]^{-1}$  at a perpendicular probe set up, since some components reach values of 100 (fig 7) and 1000 (fig 8).

According to these considerations, it was decided to choose  $\varphi$  as close to zero as is allowed by the magnitude of the  $[B]^{-1}$  components. This value is chosen as  $\varphi = 15$  degrees. On fig 9, it is shown that the magnitude of  $[B]^{-1}$  remains advantageous at any flow angle, except around  $\psi = 42$  degrees (or  $-42$  degrees), where some components reach values of 10 and 100. Hence less resolution and more scatter on some results can be expected at these flow angles.

The largest components of  $[B]^{-1}$  moreover determine which Reynolds stresses will be most scattered. According to the present analysis, it was found that most scatter will be found on  $v'$  and next on  $w'$ .

## 5. DATA REDUCTION

### 5.1 Introduction

A main problem of the present study is the acquisition and processing of an enormous amount of data. About  $10^9$  bytes have been recorded (40 1600-bpi 2400 ft magnetic tapes) and have been processed on a 170/750 CDC computer.

The amount of data to be recorded was chosen as a compromise between minimum requirements for obtaining an acceptable accuracy on the results at one hand, and acceptable measuring times and computer requirements on the other hand, as will be outlined in the following.

### 5.2 Ensemble average

The theory described in section 4 is valid for a steady flow while in the present investigation a large scale fluctuation on E is impressed by the periodic motion of the blade. Hence averages are to be taken at times when main values of E and E' are identical, which can be performed by a periodic sampling (ensemble average). In this way values with overbars such as  $\bar{E}$  are to be interpreted as periodic averaged values which vary periodically with time.

The amount of periodic samples to be taken is determining for the required measuring times and is therefore reduced to an absolute minimum of 30. At each of these 30 oscillations, about 250 samples of

$$E1 = A (E - E0)$$

are taken at a constant sample frequency,  $E_0$  being a constant offset voltage and  $A$  an amplification factor.  $A$  and  $E_0$  are chosen in such a way that the best resolution is obtained in the data acquisition system (8-bit). It is to be observed that the hot wire is calibrated through  $E_1$  values and not  $E$ , in order to increase the calibration resolution and to eliminate  $A$  and  $E_0$  fluctuations.

### 5.3 Instantaneous profiles

In order to easily reconstruct instantaneous wake profiles, the probe is translated slowly across the swept wake area when measuring (see fig 10). The translation speed is chosen in such a way that the distance covered by the probe during 30 oscillations is small enough compared with variations of the instantaneous wake profile within this area. This distance is 13 % chord or about 1.5 % of the observed wake thicknesses. Hence results will be available at  $100/1.5$  or about 65 points within the instantaneous wake profiles, which allows for the drawing of quite continuous experimental curves.

Figure 10 shows the time signals as they are recorded on digital tape. Ensemble average over 30 oscillations delivers profiles as shown on fig 11 (with much scatter however). A cut through these profiles with voltage/space planes delivers instantaneous space profiles of  $E(t)$  and  $E'(t)$ . Up to 250 cuts can be made, but in order to limit the computer requirements, only 48 are taken (each 7.5 degr phase shift).

The triggering in time occurs with a 1 bit reference signal delivered by the driving mechanism. Triggering occurs with an accuracy of  $1/250$  or .4 % of the oscillation period, since 250 samples of this signal are taken. At maximum wing speed this corresponds to .4% or 1.25 % of the distance swept by the wing. At maximum oscillation amplitude (5 degr), this corresponds to about 2 % of the wake thickness, which is close to the 1.5 % distance over which the data are taken. Hence, instantaneous profiles with about 65 significant experimental points will be available at 48 times during one oscillation period.

### 5.4 Conditional averaging

Averaging over 30 events is insufficient for obtaining results without important scatter. More accuracy would be obtained with at least 200 or 300 events, but this would imply about 10 times more measuring time (one week for one low frequency experiment). In reality, more than 30 values are taken into account when searching for the turbulence levels. Since much data are available in space as well as in time, it is possible to take conditional averages over small space/time areas. In reality about 400 data values are taken into account in this way in order to obtain  $E'$ . Care must be taken however in order to not destroy significant detailed information and the used averaging procedures which are summarized in section 5.5 were merely obtained by trial and error.

The most helpful step when averaging is illustrated on fig 12 and is performed as follows. The 48 instantaneous profiles are translated along the space coordinate in such a way that the minimum velocity coordinates coincide for all the profiles (see fig 12). When a time cut is made through these profiles, one obtains a periodic function where the periodic variations are rather slow compared with the scatter which can therefore easily be reduced by a conditional averaging, without affecting the details along the space axis

### 5.5 Summary and computer requirements

The different steps of the data reduction are summarised in the following.

- i) Ensemble average from magnetic tape data, for one space coordinate
- ii) Weak smoothing of  $\bar{E}(t)$  and  $E'(t)$  profiles.
- iii) 48 phase angles are selected from the data and saved on mass storage
- iv) Repeated for each space coordinate

v) Repeated for each probe position (12)

These steps require about 1000 System Seconds on the 170/750 CDC computer for each experiment. Data are reduced from 50 Mbyte to about 200 10-bit Kbyte.

vi) Instantaneous E and E' profiles are reconstructed from mass storage for all probe positions, for one phase angle.

vii) Weak smoothing of these profiles.

viii) Least squares fit (see 4.3 and 4.4) in order to obtain velocity, flow angle and four non-zero Reynolds stress profiles. These profiles are defined in the absolute frame.

ix) Results are saved on mass storage

x) Repeated for each of the 48 phase angles

These steps require about 110,000 CM words and 200 System Seconds for each experiment.

xi) Profiles are read from mass storage, aligned by minimum velocity and information which lies within the wake is windowed (see fig 12).

xii) The obtained profiles are smoothed in time (fig 12) eliminating most of the scatter.

xiii) All desired output quantities are derived (see section 7.1), plotted and/or saved on mass storage for final availability. Final results are saved on magnetic tape.

## 6. SELECTION OF TEST CASES

The selection of test cases was mainly based on previous work done on oscillating airfoils [4,12,13,22]. The parameters to be chosen are the oscillation amplitude, the mean airfoil incidence and the oscillation frequency. Chord Reynolds number is kept constant at about 300,000. All test are done at .7, 2, 5, 10 and 20 % chord downstream of the trailing edge. All done experiments are listed in table 2.

### 6.1 Oscillation amplitude

Two values of oscillation amplitude are considered. The maximum value used is 5 degrees, this value has been used in the past in oscillating airfoil experiments [22]. At this amplitude the area swept by the wing is large compared with the unstalled wake thickness (13 % chord against 8 %) and the incidence varies in an important way (10 degrees). Tests were also made at a low amplitude of 1.7 degrees (swept distance is 4.4 % chord) in order to compare results at similar maximum wing speeds.

### 6.2 Mean incidence

Considered mean incidences are 0, 5, 9 and 10 degrees. Maximum incidences at maximum oscillation amplitude are resp. 5, 10, 14 and 15 degrees. At 0 and 5 degr mean incidence no stall or flow reversal is expected. At 9 degr mean incidence (14 degr max inc) stall onset is expected according to the measurements of Mc Croskey et al [22], while at 10 degr mean incidence (15 degr max inc) light dynamic stall is present. Deeper stall is not considered at the present time.

### 6.3 Oscillation frequency

Three situations are considered: steady state, 'low' and 'high' frequency. 'Low' frequency means that the passage time from leading to trailing edge of the boundary layer fluid is small compared with the oscillation period. Hence, this situation can be considered as close to consecutive steady state situations, although significant disturbances due to the wing motion are found. At 'high' frequency, the passage time from leading to trailing edge has the same magnitude as the oscillation period and large phase shifts are found between wing oscillation and turbulence response in the wake and in the rearmost part of the wing boundary layers.

The corresponding frequency coefficients are .36 and 1 to 1.23. Corresponding frequencies 2.16 and 6.1 to 7.4 Hz.

The considered frequencies are small when compared with the 'bursting' frequency. The unsteady effects in the present experiments are however mainly due to the strong variation in incidence and the propagation of the disturbances along the airfoil, whereas in experiments at fixed incidence no similar behaviour is present and effects can best related to something as the 'bursting frequency'.

## 7. RESULTS

All obtained results are reported on figs 16 to 69. Continuous curves are drawn since about 100 experimental points are available for one curve, allowing for the observation of small details. The results are drawn each 45 degrees phase angle. The motion of the blade is defined through the instantaneous incidence  $i$  as follows

$$i = i_0 - i_a \cos \psi \quad (44)$$

where  $i$  = instantaneous incidence

$i_0$  = mean incidence

$i_a$  = amplitude

$\psi = 2\pi ft$  phase angle

$\psi = 0$  always corresponds to the minimum incidence. Data are shown at 7 (○), 2 (◇), 5 (△), 10 (□) and 20 (×) % chord downstream of the trailing edge.

The data as shown in the present report are saved on magnetic tape and are available each 7.5 degrees phase angle.

Before going into the discussion of the results, details will be given of the exact definition of the output variables and the way used to calculate them.

### 7.1 Output variables

The basic data as detailed in section 4 are defined in the absolute wind tunnel reference system. For a coherent representation of the results, they will be transformed to a relative system fixed on the oscillating wing.

The 'chordwise' direction in this system is defined as the instantaneous centerline of the MACA profile. The 'pitchwise' coordinate is normal to it and has its zero reference on it (see fig 14). The absolute velocity  $U$  is projected in this coordinate system through

$$V_c = Q \cos(\psi - i) \quad (45)$$

$$V_p = Q \sin(\psi - i) \quad (46)$$

where the instantaneous incidence  $i$  is found from eq (44) (a correction due to non infinite crank/connecting rod ratio is however taken into account). The absolute and relative chordwise velocities are identical

$$V_c(r) = V_c \quad (47)$$

while the relative pitchwise velocity is given by (see fig 14)

$$\begin{aligned} V_p(r) &= V_p - r \frac{di}{dt} \\ &= V_p + r i_a 2\pi f \sin\psi \end{aligned} \quad (48)$$

The relative flow angle  $\psi(r)$  is next found from

$$\tan \psi(r) = \frac{V_p(r)}{V_c} \quad (49)$$

Drawn output variables are  $V_c$ ,  $V_p(r)$  and  $\psi(r)$ .

The turbulence quantities  $u'$ ,  $v'$ ,  $w'$  and  $\overline{uv}$  are also to be transformed to the relative system.  $u'(r)$  is defined as the relative streamwise fluctuating velocity and  $v'(r)$  the fluctuation normal to it. The spanwise fluctuation  $w'$  is unchanged

$$w'(r) = w' \quad (50)$$

$u'(r)$  and  $v'(r)$  can be obtained as follows

$$u(r) = u \cos\delta - v \sin\delta \quad (51)$$

$$v(r) = u \sin\delta + v \cos\delta \quad (52)$$

$$\delta = \psi - \psi(r) \quad (53)$$

Squaring and averaging of eqs (51) and (52) yields, according to the assumption of linearisation

$$u'(r)^2 = u^2 \cos^2\delta + v^2 \sin^2\delta - 2\overline{uv} \sin\delta \cos\delta \quad (54)$$

$$v'(r)^2 = u^2 \sin^2\delta + v^2 \cos^2\delta + 2\overline{uv} \sin\delta \cos\delta \quad (55)$$

$$\overline{uv}(r) = (\overline{u^2} - \overline{v^2}) \cos\delta \sin\delta + \overline{uv}(\cos^2\delta - \sin^2\delta) \quad (56)$$

Drawn output variables are  $u'(r)$ ,  $v'(r)$ ,  $w'$  and  $\overline{uv}(r)$ . It is to be observed that far downstream  $\delta$  is small and no difference is observed between relative and absolute values of the Reynolds stresses, within the considered oscillation speeds.

It is possible to calculate the values of wake displacement and momentum thicknesses as periodic functions from the detailed data. These values are defined as

$$\delta^* = \int_{-\infty}^{+\infty} (V_{c0} - V_c) dy \quad (57)$$

$$\theta = \int_{-\infty}^{+\infty} (V_{c\infty} - V_c) V_c dy \quad (58)$$

$$H = \delta^* / \theta \quad (59)$$

where  $y$  denotes the pitchwise coordinate. In theory,  $V_{c\infty}$  can be defined without ambiguity, but in practice it is not possible to perform the numeric integration in pitchwise direction far enough to obtain  $V_c \rightarrow V_{c\infty}$ , since large velocity fluctuations are found at the edge of the viscous wake (see fig 15). In order to obtain consistent results which are almost independent of the chosen window ( $y_1, y_2$ ), following definition was introduced (fig 15)

$$\delta^* = \int_{y_1}^{y_m} (V_{c1} - V_c) dy + \int_{y_m}^{y_2} (V_{c2} - V_c) dy \quad (60)$$

$$\theta = \int_{y_1}^{y_m} (V_{c1} - V_c) V_c dy + \int_{y_m}^{y_2} (V_{c2} - V_c) V_c dy \quad (61)$$

Drawn output variables are  $\delta^*$ ,  $\theta$  and  $H$ , by use of eqs (59), (60) and (61).

## 7.2 Steady state results

Steady state results are available at 0, 5, 10, and 13 degrees incidence. Detailed results are reported on figs 16 to 18 while wake thickness parameters are shown on figure 19. Results of the measurements made at 15 degrees incidence are not reported: these results are not reliable due to the strong turbulence intensities (stalled flow). 13 and 15 degrees are incidence values just below and just above the static stall limit.

The results as they are reported on figs 16 to 18 were obtained without smoothing, except the  $v'$ ,  $w'$  and  $uv$  profiles near stall (13 degr).

The chordwise velocity profiles at 13 degrees incidence indicate the neighbourhood of the stall limit (fig 16). No flow reversal is observed. A sharp discontinuity in pitchwise velocity which gradually disappears downstream is observed close to the trailing edge (.7%) at all incidences. Peaks are found in the corresponding turbulence profiles (figs 17, 18). These peaks close to trailing edge are most pronounced at pressure side of the wake, and result in a smooth turbulence increase further downstream. At suction side of the wake a gradual increase in turbulence levels is observed as the incidence grows from 0 to 13 degrees. At 0 and 5 degrees incidence central peaks seem to be present in the  $v'$  and  $w'$  profiles close to trailing edge (fig 18). These peaks are smooth at 2% downstream distance and disappear at 5%.

The symmetric results at 0 degrees incidence can be compared with calculated data of Baker et al [12] (fig 21). On this figure similar double peaks in  $u'$  and single peaks in  $v'$  are observed. The outer parts of the turbulent profiles are practically unchanged as the flow goes from .7 to 20 % chord distance, while in the central part a decrease in all turbulence profiles is observed over a width which gradually increases downstream.

The values of wake thickness and shape factor of the static test cases are shown on fig 19 and are also listed in table 3. Results at 0 and 5 degrees incidence are quite similar, while a rapid increase in thicknesses and shape factor is observed at 10 and 13 degrees incidence, in particular close to the trailing edge. Momentum thicknesses are practically constant over the 5 downstream distances.

### 7.3 Zero mean incidence cases

These results are reported on figures 22 to 31.

On figure 22, the wake thicknesses are first shown as functions of time, at the 5 considered downstream positions. At low frequency (WL05), small disturbances are found on the displacement thickness. Momentum thickness and shape factor show larger oscillations with a maximum shape at about 45 degr phase lead to maximum incidence times (0 and 180 degr phase). The wake thicknesses are very close to the steady state values. At high frequency but low amplitude (WH01), oscillations are lightly more pronounced. The phase lead of maximum shape is increased to about 70 degrees. At high frequency and high amplitude (WH05), important oscillations and more distortion are found in the thicknesses. The maxima of shape factor are increased to 2, close to the trailing edge. The same phase lead of 70 degrees with respect to maximum incidence time is observed at low and high oscillation amplitude (WH01 and WH05).

Detailed results of the zero incidence test cases are next shown on figs 23 to 31. These results are shown at 0, 45, 90, 135 and 180 degrees phase angle, which corresponds to instantaneous incidences  $i$  of resp. -5, -3.53, 0, 3.53 and 5 degrees. Results are shown at increasing incidence ( $di > 0$ ), while symmetric results are found at decreasing incidence. Profiles at 0 and 180 degrees phase should be completely symmetric, but small differences are however found. Since these asymmetries are similar in all experiments at zero mean incidence, they are believed to be due to windtunnel effects and clearance problems in the driving mechanism.

At low frequency (figs 23 to 25, WL05), results are in general close to the steady state results, except at .7 % downstream distance where the wing speed/flow speed ratio reaches about .25. At this distance details in  $u'$  profiles similar to those at 5 degrees steady state incidence are observed at 0 and 180 degrees phase angle, where the wing speed is zero ( $di=0$ ). At maximum wing speed (90 degr phase) detailed differences are observed. Less difference is observed on the other profiles. Central peaks are found again in the  $v'$  and  $w'$  profiles, but not in a reliable way since they are not present at 0 degr phase angle.

At high frequency and same amplitude (figs 26 to 28, WH05) differences are increased and are observed up to 10 % downstream of the trailing edge. Velocity profiles are also disturbed, especially at pressure side close to the trailing edge (fig 26). At 0 and 180 degr phase ( $di=0$ ), detailed turbulence profiles are again rather close to steady state as well as low frequency profiles, while at high speed, important differences are found (compare figs 24 and 27). Central peaks in  $v'$  and  $w'$  profiles are increased at maximum wing speed.

On figs 29 to 31, the high frequency but low amplitude test case is shown. No significant detailed differences are found, although the maximum wing speed at 90 degr phase angle is the same as in the low frequency and high amplitude test case (WL05). Central peaks in  $v'$  and  $w'$  are less pronounced.

### 7.4 5 degrees mean amplitude test cases

5 degrees amplitude cases are drawn on figs 32 to 50.

The wake thicknesses are first reported on figure 32. The maximum shape is reached at about 40, 70 and 90 degrees phase lead to maximum incidence time at frequency coefficients of resp. .36, 1.01 and 1.23 (resp WL55, WH55 and WH51). The maximum shape is almost the same at the similar maximum wing speeds (WL55 and WH51) while it reaches critical values at high wing speed (WH55,  $H = 2.6$ ). Hence the phase lead depends mainly of the frequency coefficient while the maximum shape increases with maximum wing speed.

The most important oscillations in wake thickness are found at low frequency (WL55) where maximum thickness is reached at about 60 degrees phase lag after maximum incidence time. This behaviour was to be expected, according to the history of the fluid when passing from leading edge to trailing edge, since this fluid has seen the maximum incidence some time before reaching the region just behind the trailing edge. At small oscillation amplitude (WH51), less oscillations are observed, which

was again to be expected since the absolute level of incidence does not vary too much (3.3 to 6.7 against 0 to 10 degr).

At high frequency and high amplitude (WH55) a quite different behaviour of the thicknesses is observed. Oscillations are less important in amplitude (observe difference in scales) and maxima of  $\delta$  are shifted to the increasing incidence times instead of the decreasing ones. Maxima of shape and of  $\delta^*$  are almost in phase, while at low frequency they were shifted over 180 degrees. Maximum thicknesses are in general smaller than the 10 degrees steady results.

Detailed profiles are next shown on figs 33 to 50. Detailed results are drawn at 0, 45, 90 and 135 degrees phase angle at increasing incidence ( $di > 0$ , upper figures) and at 180, 225, 270 and 315 degr phase angle at decreasing incidence ( $di < 0$ , lower figures). Corresponding incidences are 0, 1.47, 5, 8.53 and 10 degrees. At low frequency (figs 33 to 38, WL55) and zero phase angle (zero incidence, zero wing speed), profiles are found which are rather close to the zero incidence steady state ones. At maximum wing speed however (90 and 270 degr phase) an important hysteresis is found on all profiles, which is in accordance with the behaviour of the wake thicknesses (fig 32). Corresponding to the instant of maximum shape factor, a maximum peak in the  $u'$  profiles is observed (fig 35,  $u'$  up to 14%) close to the trailing edge, which rapidly decreases downstream. No significant peaks are observed on the other profiles. Increased values of  $uv$  are found when the shape factor is maximum at 2 and 5 % downstream distance.

At high frequency and high amplitude (figs 39 to 44, WH55), a quite different behaviour is found. Profiles at zero phase angle (zero inc, zero speed) are rather close to the 5 degrees steady state profiles, which can be explained as a simple phase shift between passage along the airfoil and passage at trailing edge. Flow reversal is approached close to trailing edge when shape and displacement thickness are maximum (90 to 135 degr phase). High corresponding  $u'$  and  $w'$  peaks are observed on figs 41 and 44. These peaks close to trailing edge result in a local smooth increase in the turbulence profiles at 20 % chord distance downstream of trailing edge ( $u'_{max} = 10\%$  at 20 % chord). No corresponding peaks are found in the other profiles close to trailing edge but from 5 to 20 % downstream distance,  $uv$  is increased to -0.005 instead of -0.002 to -0.003 elsewhere (fig 42).

The highest frequency (WH51) but low amplitude test case is shown on figs 45 to 50. Some detailed differences in all profiles are observed, but the influence of the wing oscillations on the profile details is in general small, although the oscillation frequency of this test case was the highest one.

### 7.5 Stall onset test cases

Three test cases were considered where the maximum dynamic incidence is near the static stall limit (14 degrees) - a low and a high frequency experiment where the maximum incidence is 15 degrees (WLA5, WHA5), and one high frequency experiment at 14 degrees maximum incidence (WH95).

Wake thicknesses are shown on fig 51. Although the stall limit is lightly exceeded, the overall qualitative behaviour is similar to the non-stalled 5 degrees mean incidence cases. Shape factor and wake thicknesses are however increased in an important way. The maximum shape factor in the high frequency case is again found at about 70 degrees phase lead to the maximum incidence time, while at low frequency, these maxima are spread over the maximum incidence times, or when the airfoil is above the static stall limit. Important increases in shape factor are observed at high frequency up to 3.6 for WH95 and 4.1 for WHA5.

On figs 52 to 69 are shown the detailed results of the test cases WLA5, WH95 and WHA5. Again, a quite similar qualitative behaviour as in the 5 degrees mean incidence test cases is found. Peaks and turbulence levels are however increased. At low frequency (figs 52 to 57), flow reversal is approached around 30 degrees phase lag after maximum incidence time (fig 52 : 180 and 225 degrees phase angle), while at high frequency flow reversal is touched at 14 degrees maximum incidence (fig 58 : WH95) and is clearly observed at 15 degrees maximum incidence (fig 64 WHA5). This flow reversal occurs around 120 degrees phase angle, at increasing incidence. The flow is still reversed at 2% downstream distance, while at 5% it has disappeared. At 180 degrees phase angle, when the incidence is maximum and



above the static stall limit, no flow reversal is observed

High turbulence levels are observed at decreasing incidence in the low frequency case (figs 54 to 57) and these profiles can be considered as very close to stall, according to fig 55 where the uv profiles are shown. On this figure a behaviour is found which is believed to indicate stall onset. At decreasing incidence important disturbances are observed on the suction side of the uv profiles at all downstream distances. uv becomes positive at pressure side of the wake at .7 and 2 % downstream distance, whereas this behaviour disappears further downstream.

At high frequency, the overall turbulence levels are more uniform over the whole oscillation period. Around flow reversal, strong up and downs are observed in the  $u'$  profiles, with a minimum at flow reversal (fig 66). The corresponding  $v'$  and  $w'$  profiles show a different behaviour and are rather increased around flow reversal. The uv profiles (figs 61 and 67) present important scatter around flow reversal, probably indicating stall onset.

An important observation here is that even at low frequency or when flow reversal is present, the suction side of the wake cannot be considered as completely stalled, the wake thicknesses and turbulence levels being small when compared with steady state measurements at 15 degrees incidence. Flow reversal is detected at high wing speeds only.

## 8 CONCLUSIONS AND FUTURE WORK

In the present report the technique for the measurement of mean flow and all non-zero Reynolds stresses in the wake of an oscillating airfoil is detailed. All available results are presented and discussed. The obtained data set applies on a wide range of oscillation situations at several positions downstream of the trailing edge and represents an extensive contribution for direct data-comparisons

Following qualitative conclusions from the above discussion can moreover be made

At low oscillation amplitude no or small influence is observed on velocity and turbulence profiles, within the considered frequencies and in the non-stalled case.

At high amplitude, the influence of the oscillations is important. A phase lead in shape factor is found which increases with the oscillation frequency and which is the same for all mean incidences, except at stall onset. The maximum thicknesses show a phase lead or lag to the maximum incidence time depending of the mean incidence and frequency.

Strong disturbances on the turbulence are present, in particular at high wing speeds close to the trailing edge where important turbulence peaks are observed which result in an overall turbulence increase far downstream.

When the static stall limit is lightly exceeded (1 degree) the wake cannot be considered as stalled at frequencies above a certain frequency which is less than the considered low frequency ( $k \approx .38$ ). Flow reversal is detected at the highest wing speed and occurs before the static stall limit incidence is reached.

The main effects of the oscillatory motion are strong phase shifts in the turbulence responses and detailed disturbances, in particular close to the trailing edge.

In the near future the present investigations will be extended to deeper stall cases and the measurements will be extended to the airfoil boundary layers using a sensor mounted on the airfoil. For these measurements similar test conditions will be used and measurements will be made at several chordwise positions along the oscillating airfoil.

# REFERENCES

- [1] BAKER A. J., YU J. C., GATSKI T. B., "Prediction and Measurement of Turbulent Aerodynamic Trailing Edge Flows", AIAA paper nr 80-1395, 1980
- [2] BRUUN H. H., "Hot Wire Data Corrections in Low and High Turbulence Intensity Flows", J. of Physisc Eng.:Sci. Instrum., Vol 5, 1972
- [3] CARR L. W., "A Compilation of Unsteady Turbulent Boundary Layer Data", AGARDograph AG265, 1981
- [4] CARR L. W., Mc ALISTER K. W., Mc CROSKEY W. J., "Analysis of the Development of Dynamic Stall Based on Oscillating Airfoil Experiments", NASA TM D-8382, 1977
- [5] CEBECI T., "Prediction of Boundary-Layer Characteristics of an Oscillating Airfoil", "Unsteady Turbulent Shear Flows", Springer Verlag 1981 (in press)
- [6] COUSTEIX J., DESOPPER A., HOUEVILLE R., "Recherches sur les Couches Limites Turbulentes Instationnaires", ONERA/DERAT TP 1976-147, Toulouse, France, 1976
- [7] COUSTEIX J., DESOPPER A., HOUEVILLE R., "Investigation of the Structure and of the Development of a Turbulent Boundary Layer in an Oscillating External Flow", ONERA TP N1977-14, Toulouse, France, 1977
- [8] COUSTEIX J., HOUEVILLE R., RAYNAUD M., "Oscillating Turbulent Boundary Layer with Strong Mean Pressure Gradient", ONERA TP 1979-89 Toulouse, France, 1979
- [9] COUSTEIX J., HOUEVILLE R., JAVELLE J., "Experiments on an Oscillating Turbulent Boundary Layer with and without Pressure Gradient," "Unsteady Turbulent Shear Flows", Springer Verlag, 1981 (in press)
- [10] DE GRANDE G., KOOL P., "An Improved Experimental Method to Determine the Complete Reynolds Stress Tensor with a Single Rotating Hot Wire", J. Phys. E.:Sci. Instrum., Vol 14, p196-201, 1981
- [11] GOOSSENS M., HAVERBEKE A., DEDONCKER H., "A Fast Programable Multichannel Datalogger", Microprocessors and their Applications, North-Holland Publ. Comp., p 155, 1979
- [12] HO C. M., CHEN S. H., "Unsteady Wake of a Plunging Airfoil", AIAA paper nr 80-1446, 1980
- [13] HO C. M., CHEN S. H., "Unsteady Kutta Conditin of a Plunging Airfoil", "Unsteady Turbulent Shear Flows", Springer Verlag, 1981 (in press)
- [14] KENISON R. G., "An Experimental Study of the Effect of Oscillatory Flow on the Separation Region in a Turbulent Boundary Layer," AGARD C.P. 227, p20.1-20.12, 1977
- [15] KOBASHI Y., HAYAKAWA M., "Structure of a Turbulent Boundary Layer on an Oscillating Flat Plate", "Unsteady Turbulent Shear Flows", Springer Verlag, 1981 (in press)
- [16] KOOL P., "Determination of the Reynolds Stress Tensor with a Single Slanted Hot Wire in Periodically Unsteady Turbomachinery Flow", ASME paper nr 79-GT-130, 1979
- [17] KOTTAPALLI S. B. R., PIERCE G. A., "Drag on an Oscillating Airfoil in a Fluctuating Free Stream", ASME J. of Fluids Eng., Vol 101, 3, p 391-399, 1979
- [18] Mc ALISTER K. W., CARR L. W., "Water-Tunnel Experiments on an Oscillating Airfoil at  $Re = 21,000$ ", NASA TM 78446, 1978
- [19] Mc ALISTER K. W., CARR L. W., "Water Tunnel Visualisations of Dynamic Stall", ASME J. of Fluids Eng., Vol 101, 3, p377-380, 1979

- [20] Mc CORMACK R.W., "Three Dimensional and Unsteady Separation at High Reynolds Numbes", AGARD LS94, 1978
- [21] Mc CROSKEY W.J., "Some Current Research in Unsteady Fluid Dynamics" Trans ASME, J. of Fluid Engineering vol 99, pB-39, 1977
- [22] Mc CROSKEY W.J., PUCCI S.L., "Viscous-Inviscid Interaction on Oscillating Airfoils", AIAA paper nr 81-0051, 1981
- [23] PARIKH P.G., REYNOLDS W.C., JAYARAMAN R., CARR L.W., "Dynamic Behavior of an Unsteady Turbulent Boundary Layer", NASA TM 81304, 1981
- [24] PATEL M.H., "On Turbulent Boundary Layers in Oscillatory flows" Proc Roy Soc. Vol A353, p 121-144, 1977
- [25] PERICLEUS K A., "An Oscillatory Turbulent Boundary Layer in an Adverse Pressure Gradient", PhD Thesis, Queen Mary College, Univ of London, Enland, 1977
- [26] RAKOWSKY E.L., "The Effect of Freestream Oscillations on the Incompressible Turbulent Boundary Layer on a Flat Plate with Pressure Gradient", PhD Thesis, Stevens Inst. of Tech., Hoboken, N.J., 1966
- [27] SATYANARAYANA, "Some Aspects of Unsteadu Flow Past Airfoils and Cascades", AGARD C.P. 177, pr 25, 1975
- [28] SAXENA L., FEJER A., MORKOVIN M., "Features of Unsteady Flows over Airfoils", AGARD C.P. 227, p22.1-22.11, 1977
- [29] SCHACHENMANN A., ROCKWELL D., "Oscillating Turbulent Flow in a Conical diffuser", J. of Fluids Eng., Vol 98, p 695-702, 1976
- [30] SHAMROTH S.J., "The Prediction of the Turbulent Flow Field About an Oscillating Airfoil Using a Time-Dependent Navier Stokes Procedure", "Unsteady Turbulent Shear Flows" Springer Verlag 1981 (in press)
- [31] SIMPSON R., "Features of Unsteady Turbulent Boundary Layers as Revealed from Experiments", AGARD C.P. 227, p19.1-19.10, 1977
- [32] SOUTIF M., FAVRE-MARINET M., BINDER G., "Diffusion and Periodic Structure of Flapping Jets",
- [33] TELIONIS D.P., "Unsteady Boundary Layers, Separated and Attached" Agard C.P. 227, p 16.1, 16.21, 1977
- [34] YU J.C., "Mean Flow and Reynolds Stresses Measurements in the Vicinity of the Trailing Edge of a NACA 63-012 Airfoil", NASA Report TM-80224, 1980

TABLE 1 : FLAT PLATE EXPERIMENTS

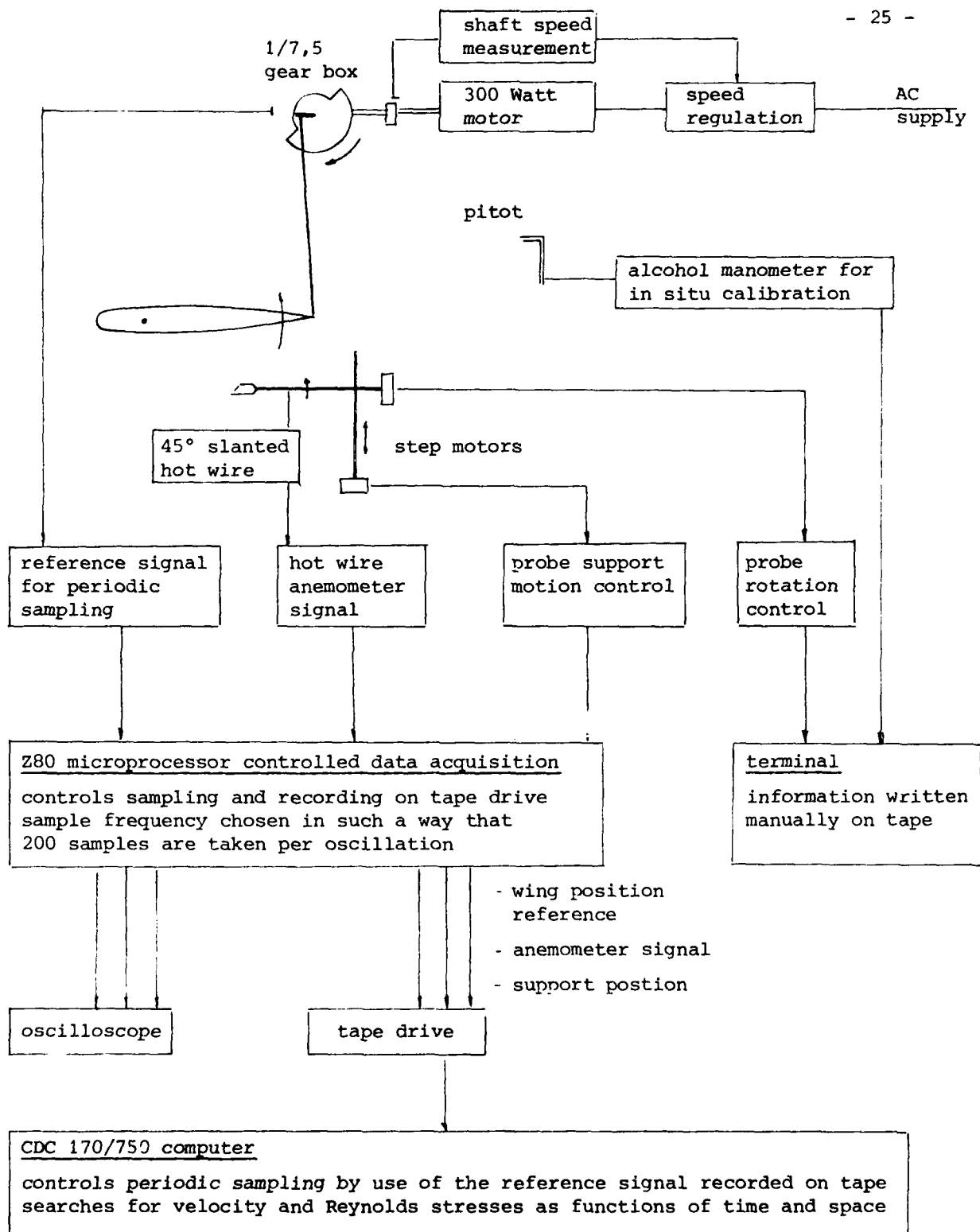
Author	Type of experiment	Type of results
Cousteix et al [6, 7, 8, 9]	with and without adverse pressure gradient separated flows rotatin vanes high oscillation ampl.	instantaneous velocity and 3 Reynolds stress profiles, boundary layer thicknesses
Kenison [14]	adverse pressure gradient separated flows	static pressure, skin friction
Parikh et al [23]	time and space dependent pressure gradient bleeding off through test section wall	instantaneous velocity and 3 Reynolds stress profiles, boundary layer thicknesses
Patel [24]	zero pressure gradient	overall averaged velocity and Reynolds stresses
Pericleus [25]	adverse pressure gradient	overall averaged velocity and Reynolds stresses
Rakowsky [26]	adverse pressure gradient	overall averaged velocity and Reynolds stresses
Simpson [31]	adverse pressure gradient near separation	instantaneous static pressures, skin friction and two Reynolds stresses

TABLE 2 : SELECTED TEST CASES

ident	mean incid.	amplit	freq	freq coeff	incidence from	to
WS00	0	-	-	-	-	-
WS05	5	-	-	-	-	-
WS0A	10	-	-	-	-	-
WS0D	13	-	-	-	-	-
WS0F	15	-	-	-	-	-
WL05	0	5	2.16	.36	-5	5
WH01	0	1.7	6.1	1.01	-1.7	1.7
WH05	0	5	6.1	1.01	-5	5
WL55	5	5	2.16	.36	0	10
WH51	5	1.7	7.4	1.23	3.3	6.7
WH55	5	5	6.1	1.01	0	10
WH95	9	5	6.1	1.01	4	14
WLA5	10	5	2.31	.38	5	15
WHA5	10	5	6.1	1.01	5	15

TABLE 3 : STEADY STATE WAKE THICKNESSES

incidence	0	5	10	13	15 degrees
$\delta^*$ (% chord)					
at 7 %	1.81	1.89	3.75	6.99	-
2 %	1.65	1.74	3.58	6.69	-
5 %	1.40	1.48	3.23	6.23	-
10 %	1.23	1.29	2.77	5.34	-
20 %	1.08	1.10	2.19	3.79	-
$\eta$ (% chord)					
at 7 %	.98	1.01	1.48	1.99	-
2 %	.97	1.02	1.49	1.98	-
5 %	.90	.95	1.55	1.97	-
10 %	.86	.88	1.54	2.09	-
20 %	.82	.83	1.42	2.13	-
shape factor					
at 7 %	1.85	1.86	2.54	3.51	-
2 %	1.70	1.70	2.40	3.37	-
5 %	1.55	1.56	2.08	3.15	-
10 %	1.43	1.45	1.80	2.55	-
20 %	1.32	1.33	1.53	1.77	-



EXPERIMENTAL SET-UP AND DATA ACQUISITION

figure 1

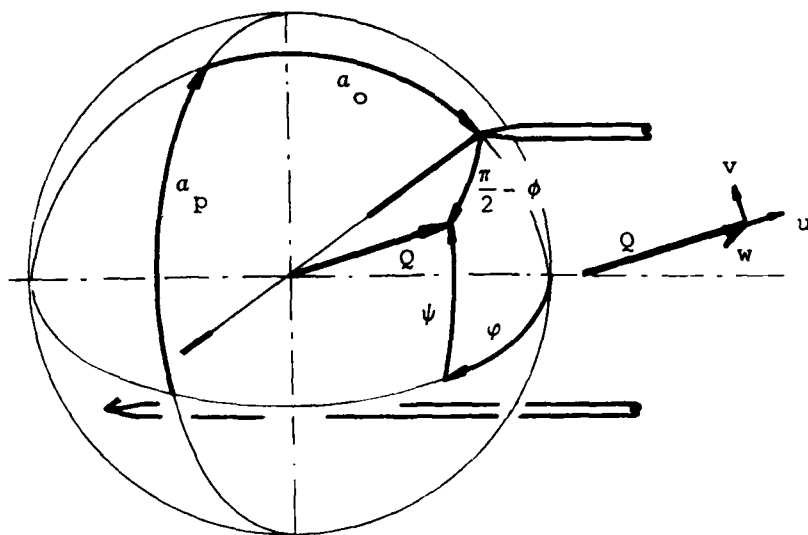


Figure 2  
Hot wire geometry

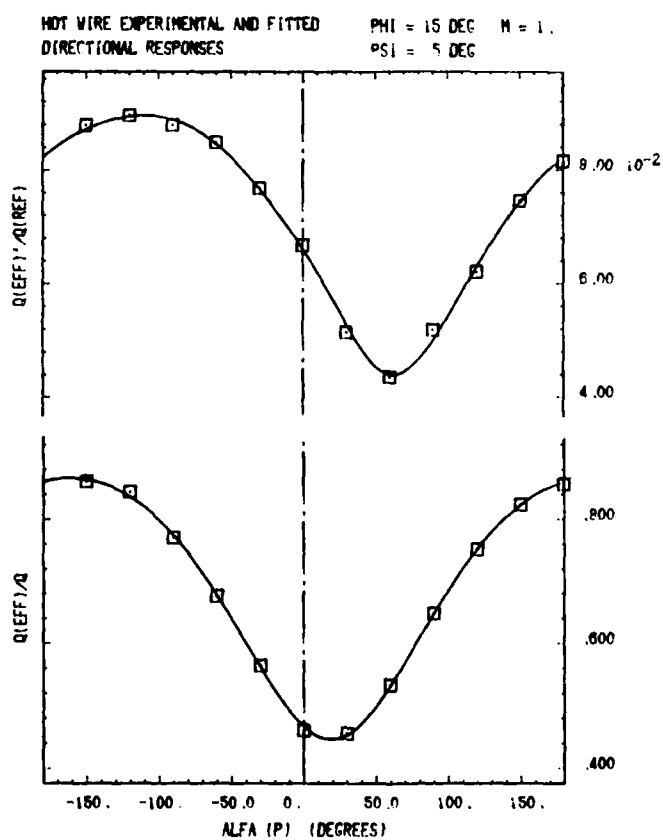


Figure 4 : hot wire directional  
responses

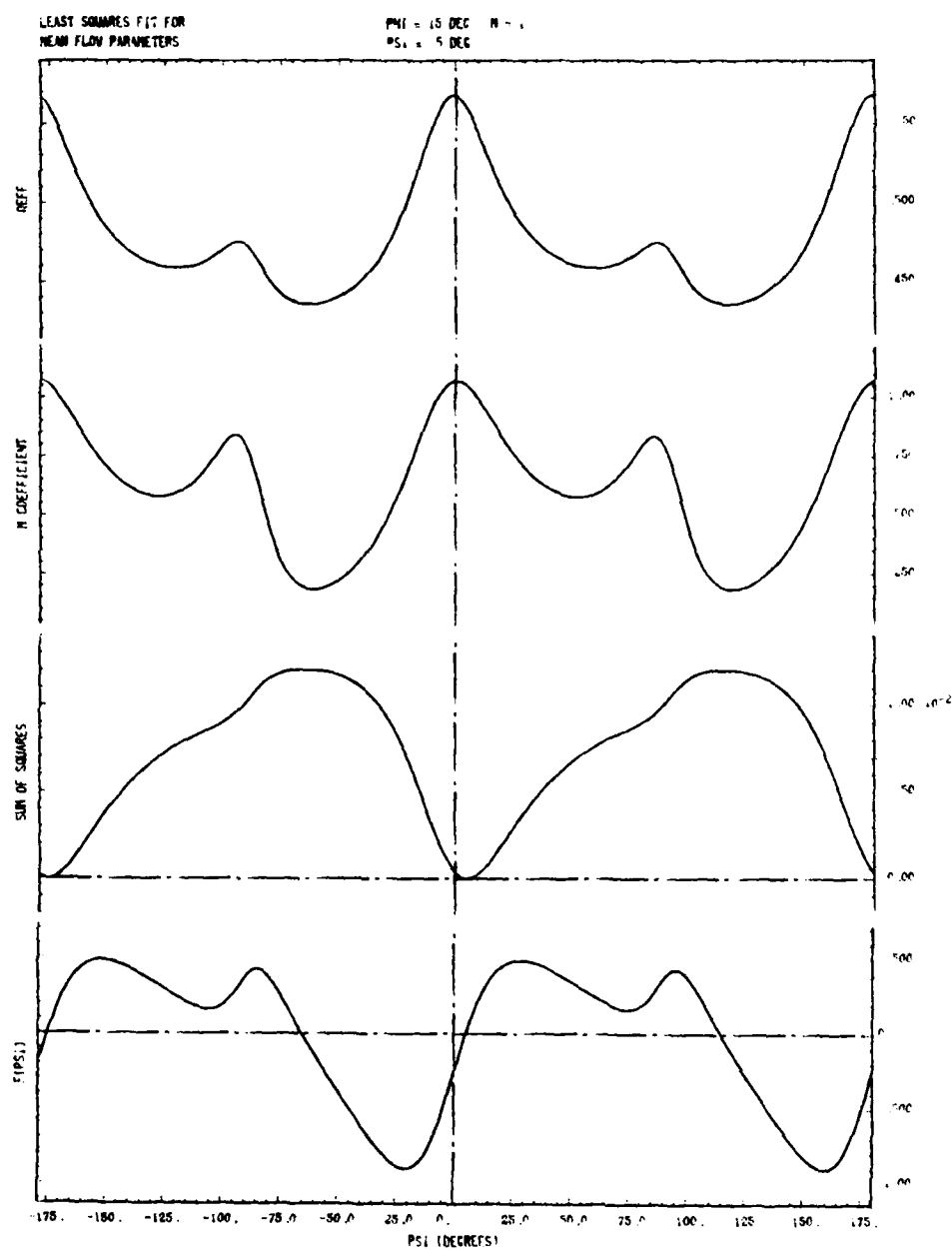


Figure 3 : Least squares fit for  
mean flow parameters



360 DEG ROTATION - COMP OF INVERSE (B)  
PSI = 0. DEGREES

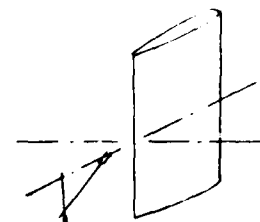
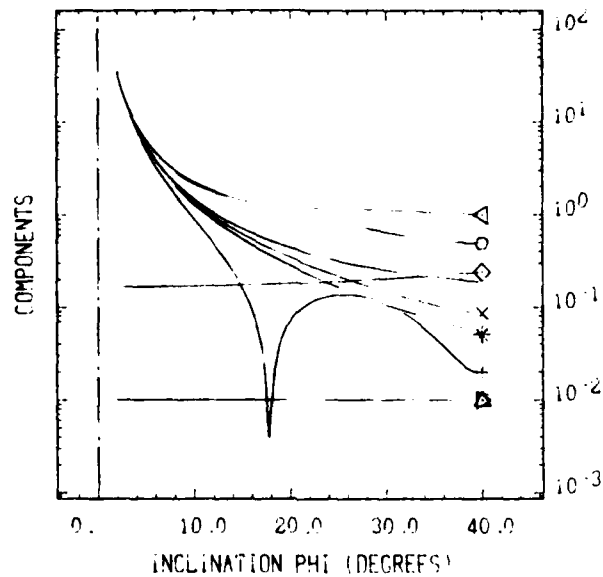


Figure 5

360 DEG ROTATION - COMP OF INVERSE (B)  
PHI = 0. DEGREES

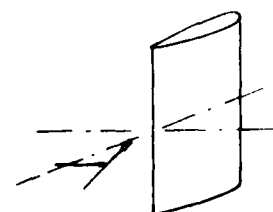
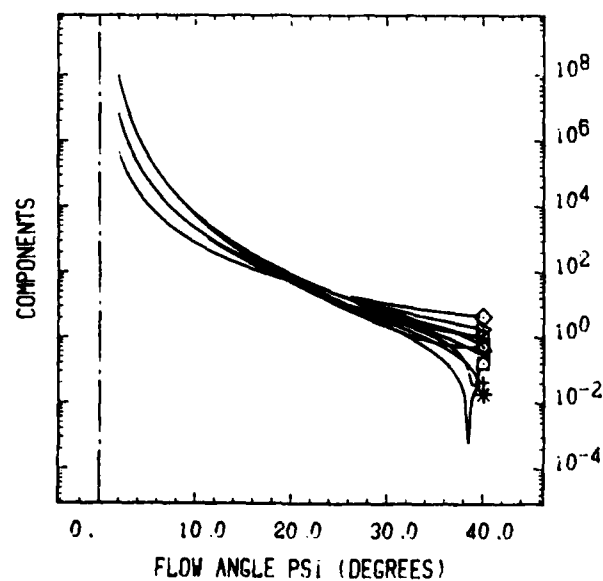


Figure 6

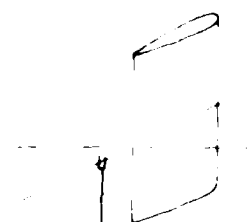
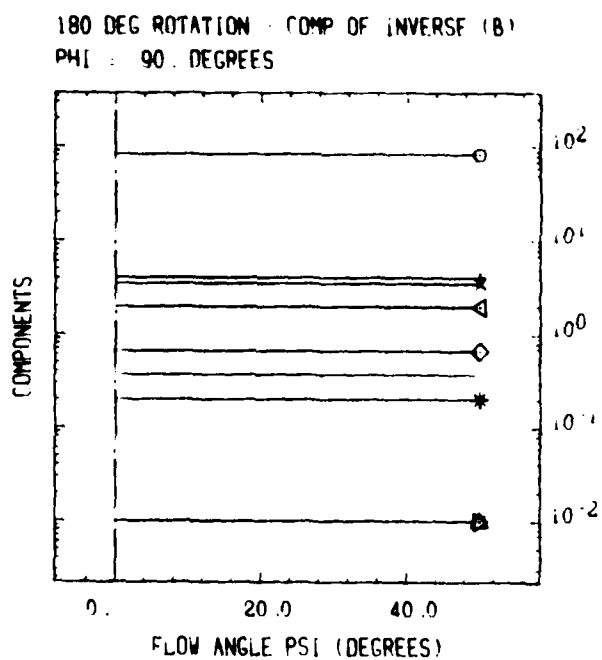


Figure 7

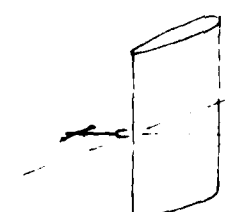
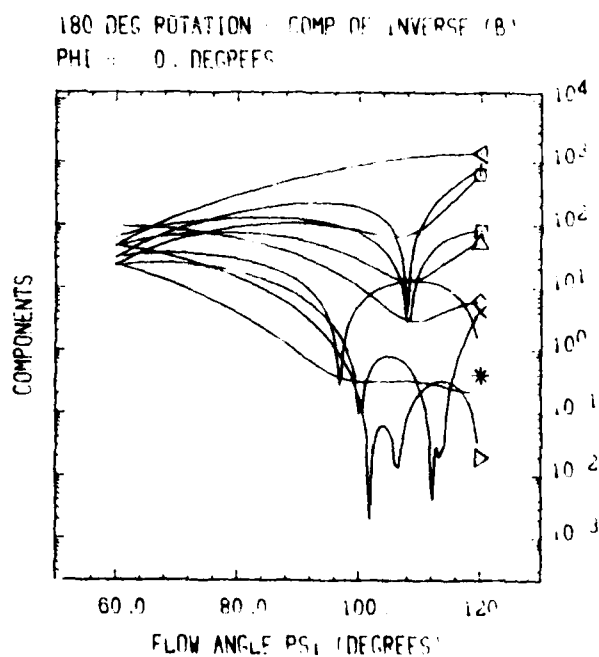


Figure 8

360 DEG ROTATION - COMP OF INVERSE (B)  
PHI = 15. DEGREES

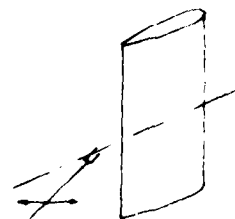
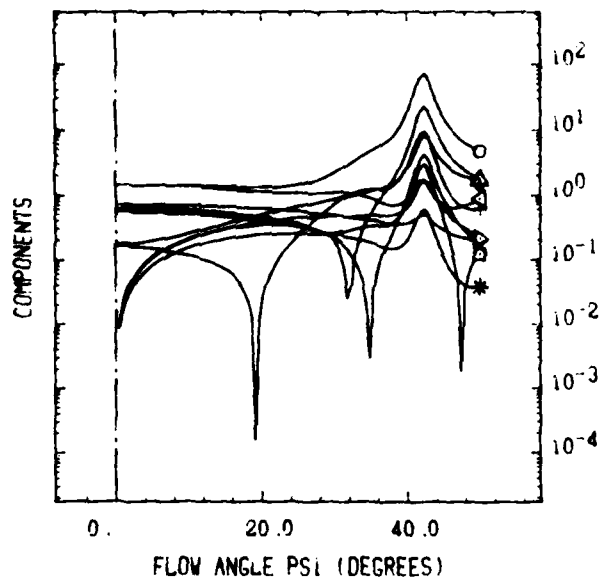


Figure 9

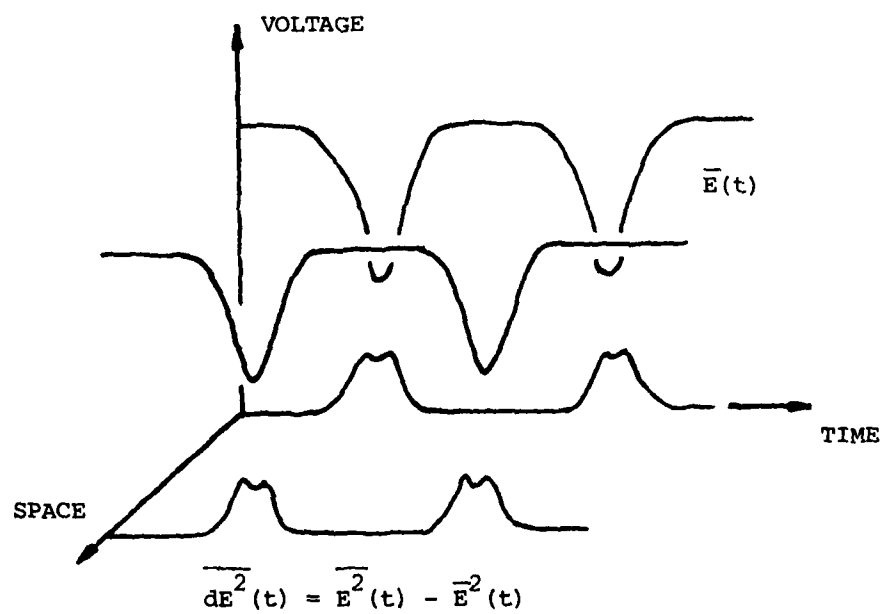
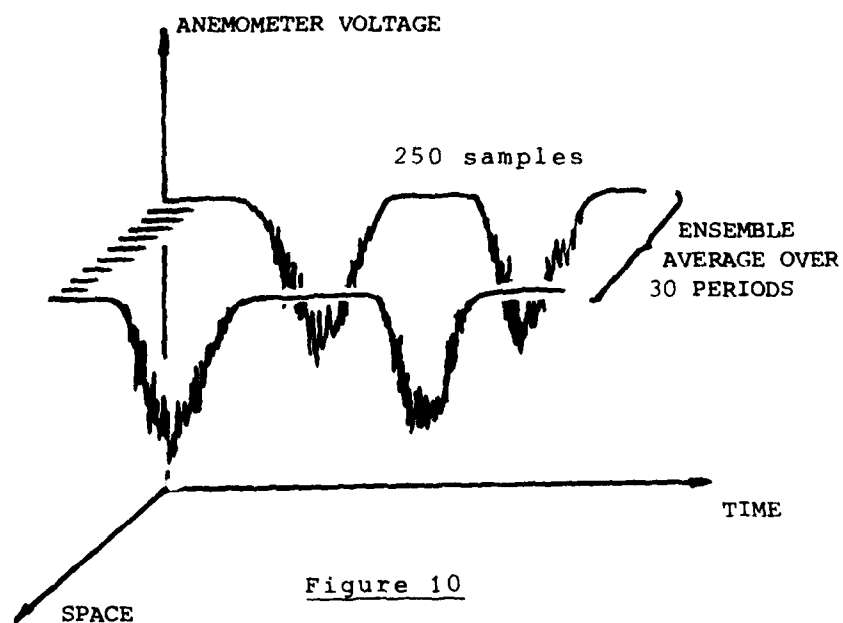
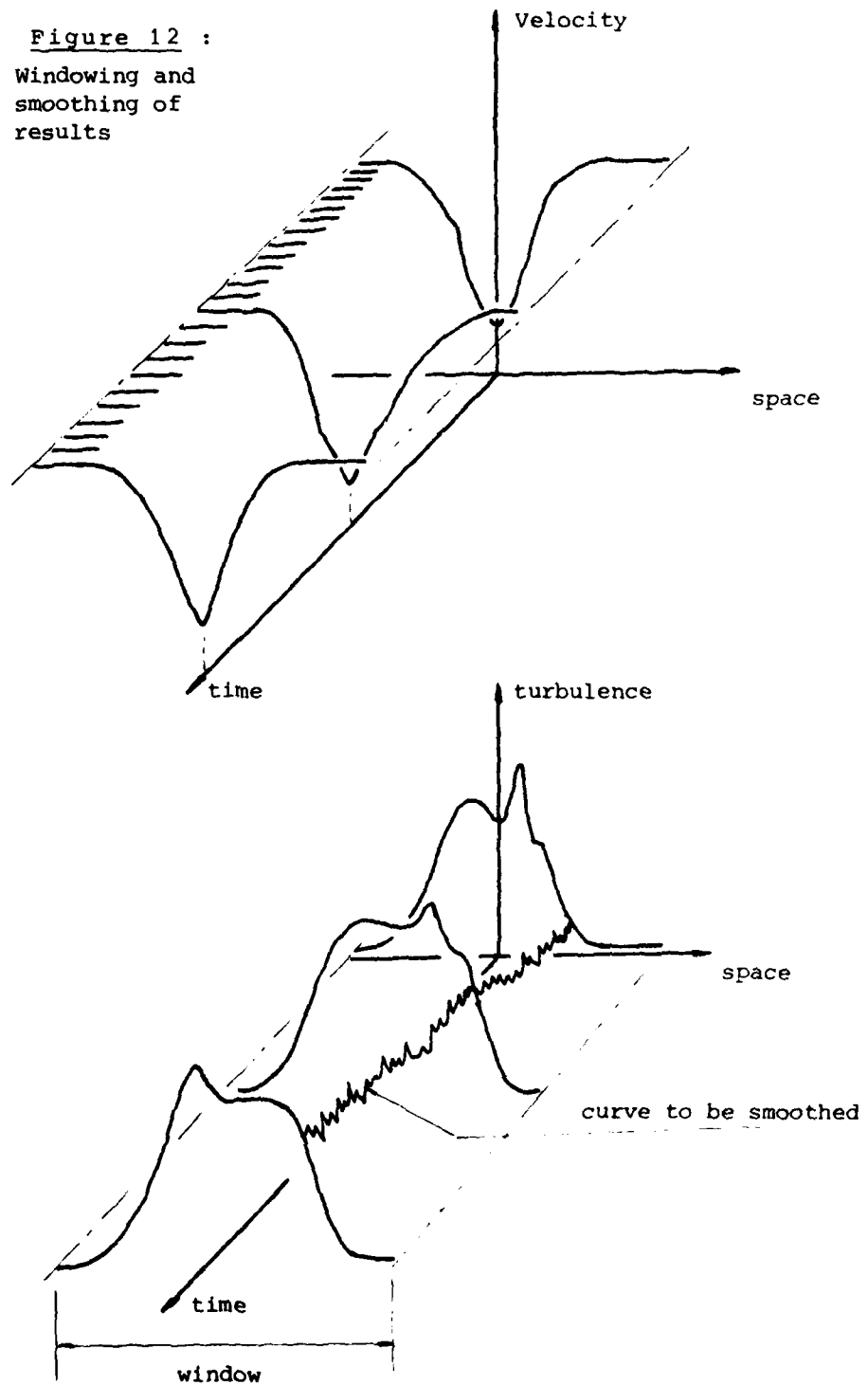


Figure 12 :  
Windowing and  
smoothing of  
results



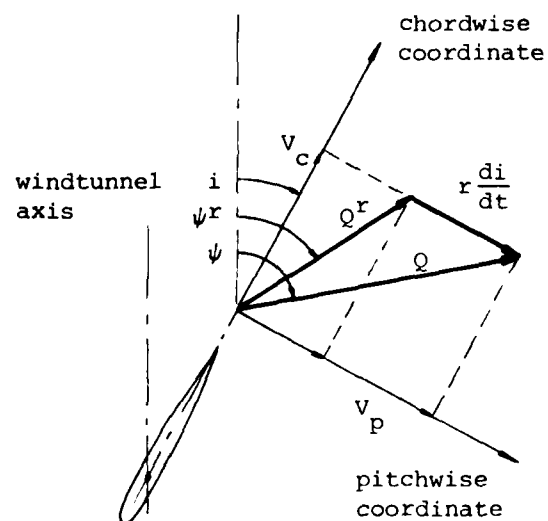


Figure 14 : relative coordinate system

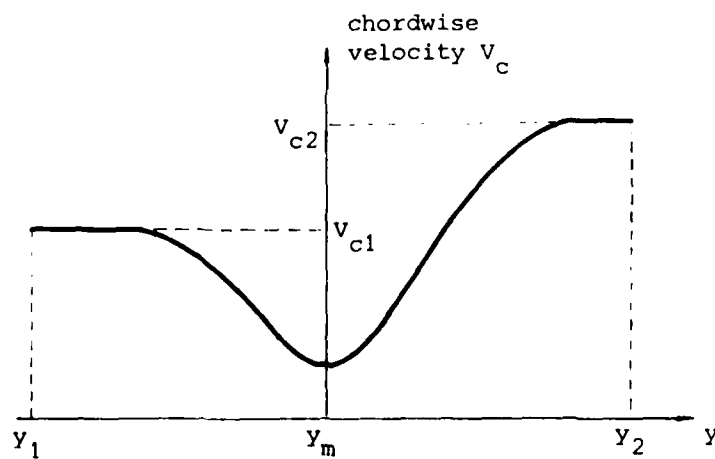


Figure 15 : chordwise reference velocities

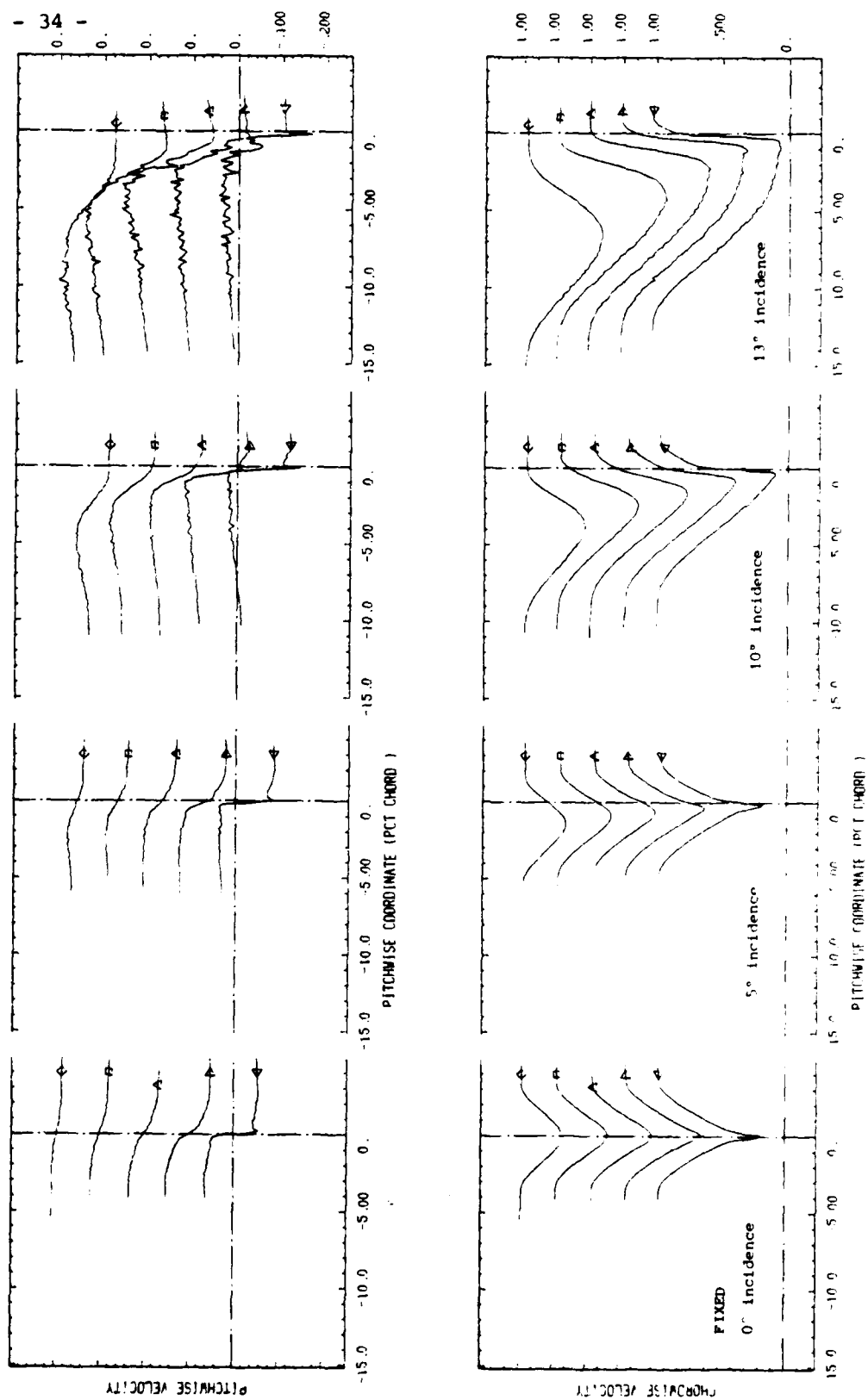


FIGURE 16 : STEADY CASES

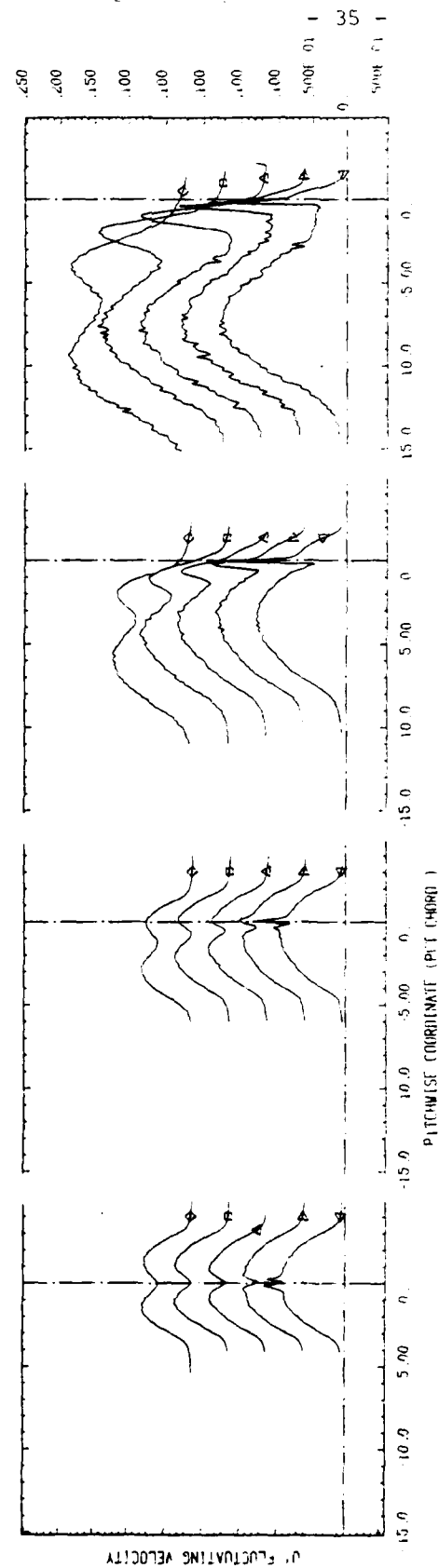
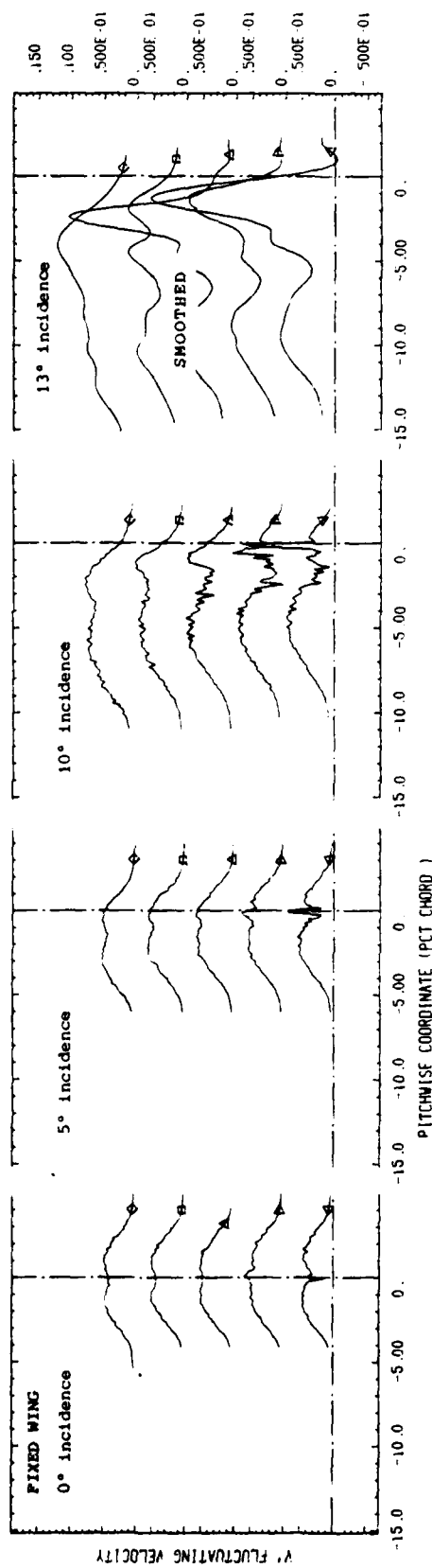


FIGURE 17 : STEADY CASES



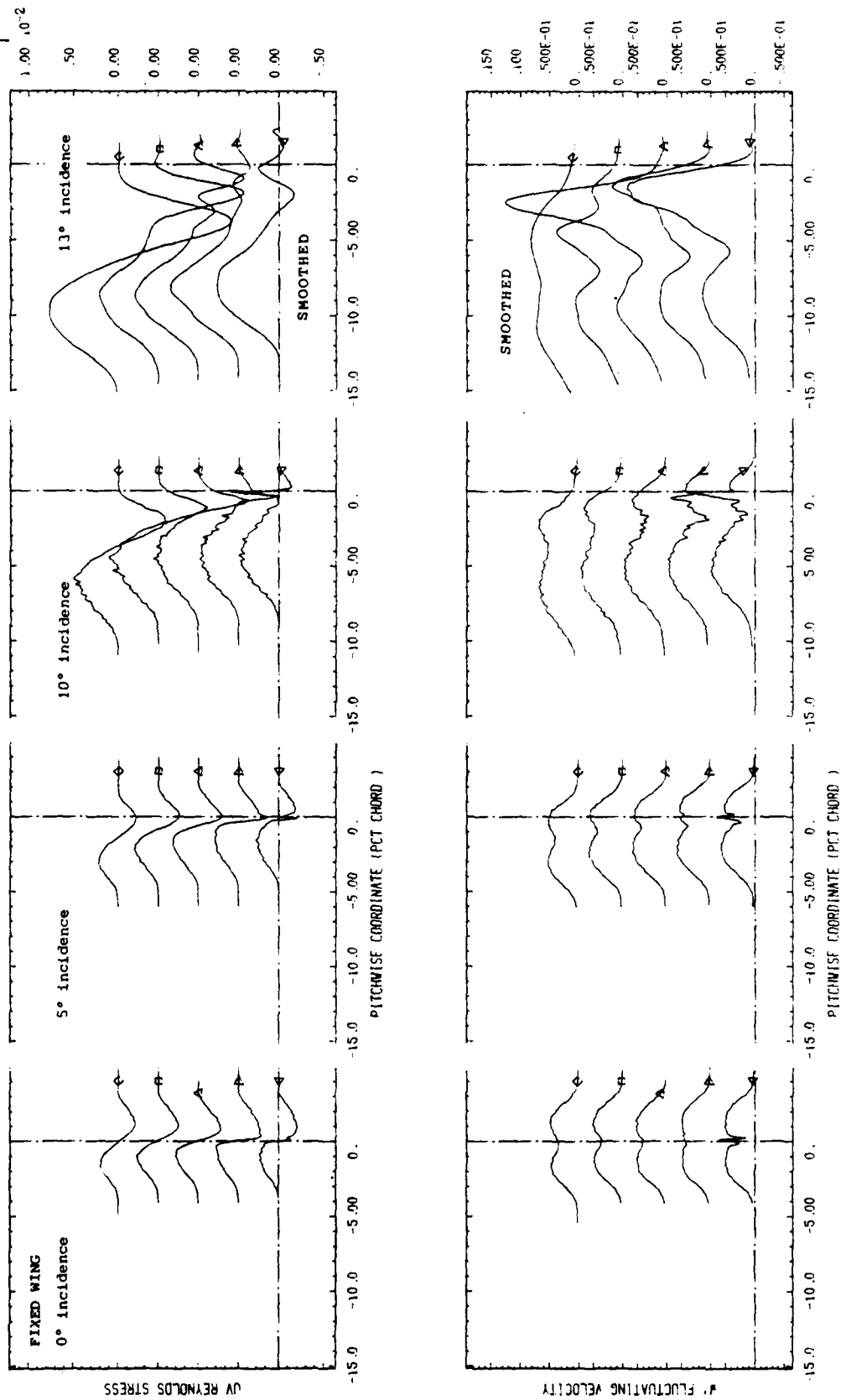


FIGURE 18 : STEADY CASES

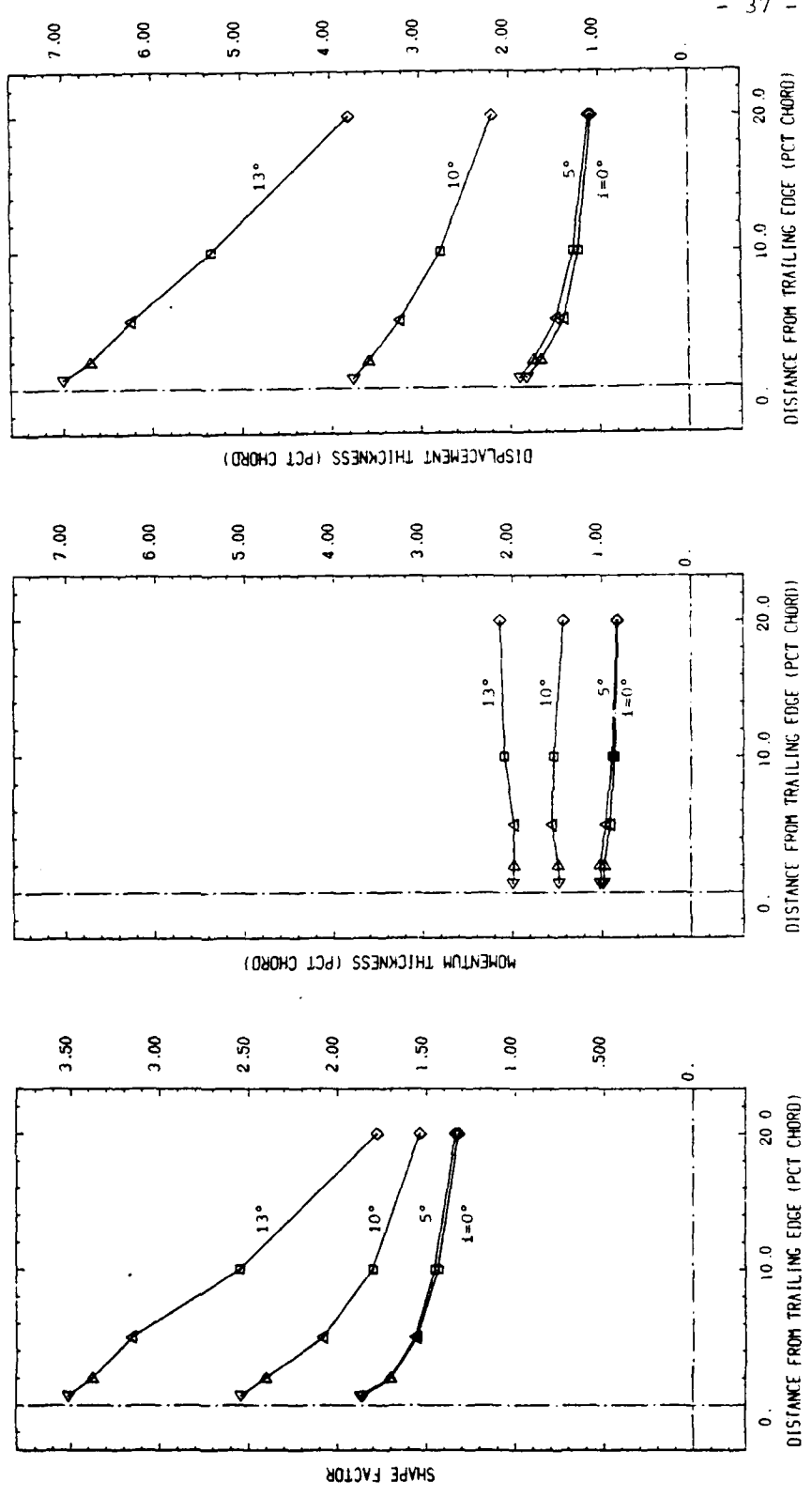


FIGURE 19 : STEADY WAKE PARAMETERS

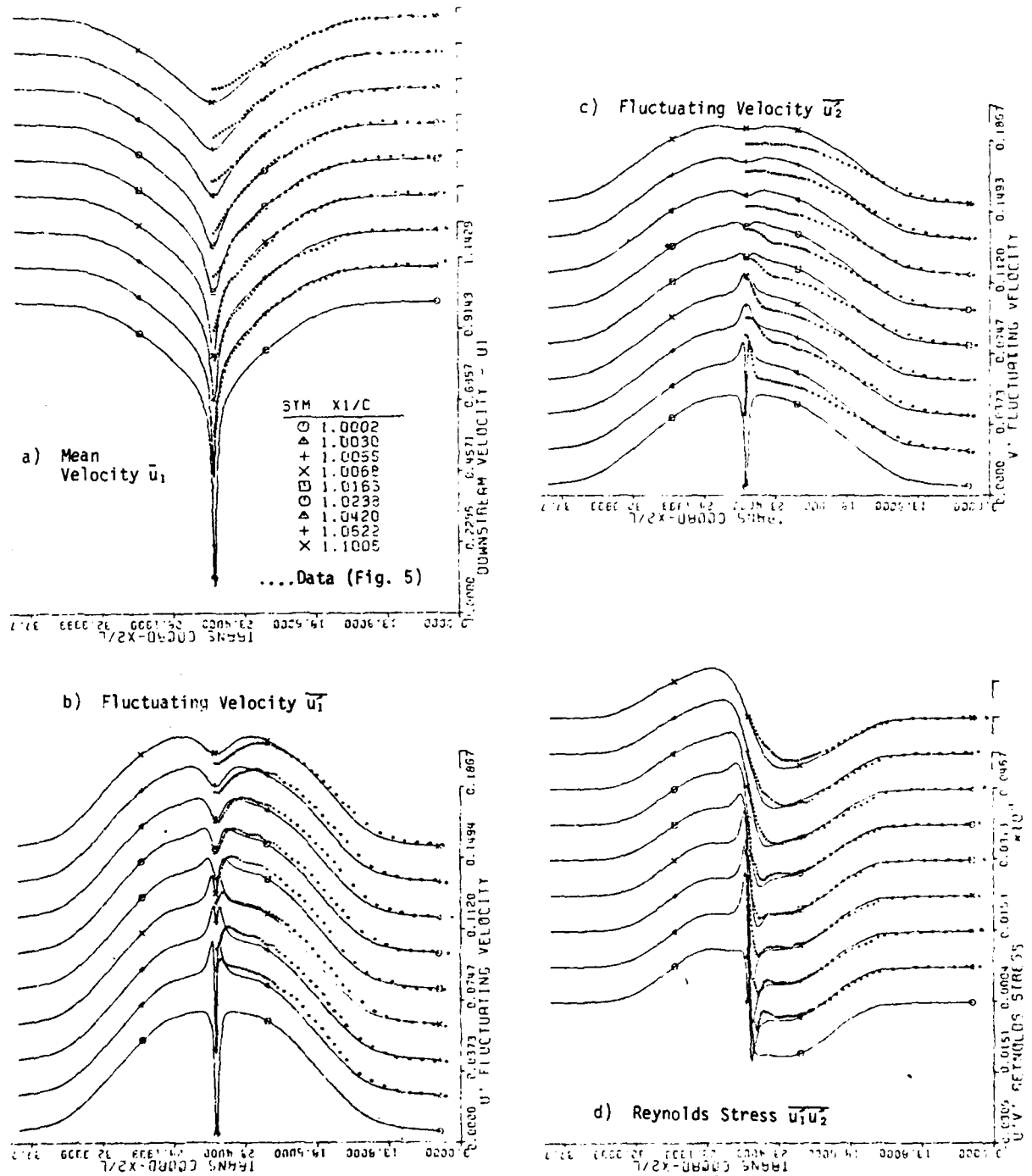


FIGURE 21 : from ref 1

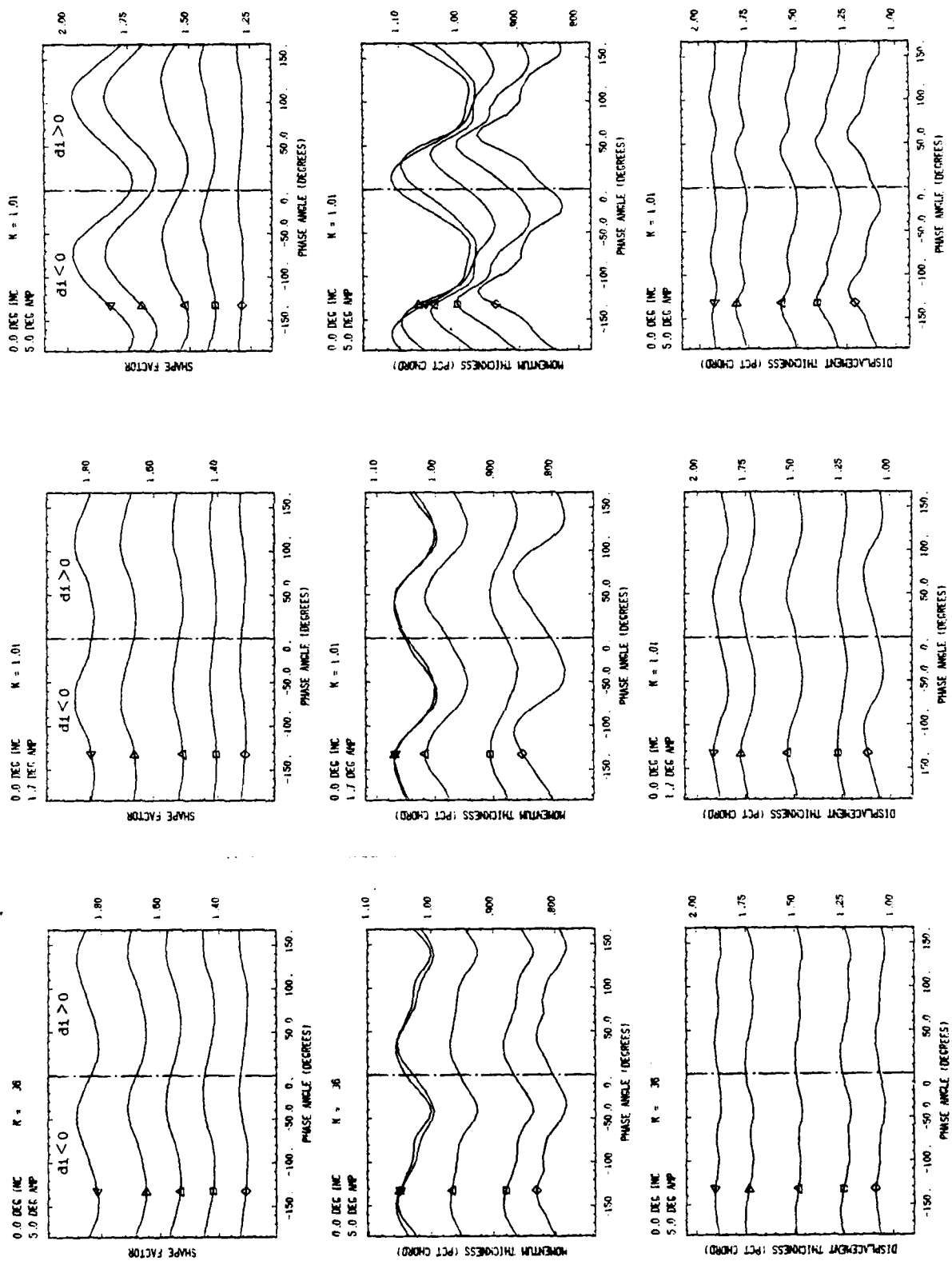


FIGURE 22 : WL05, WH01 and WH05

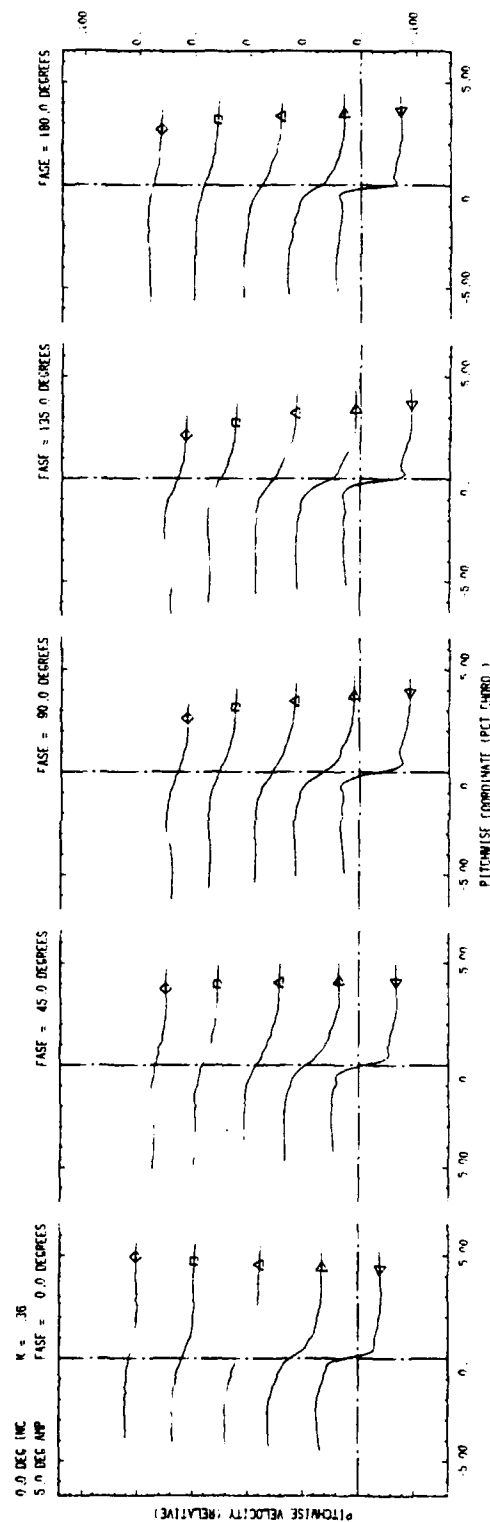
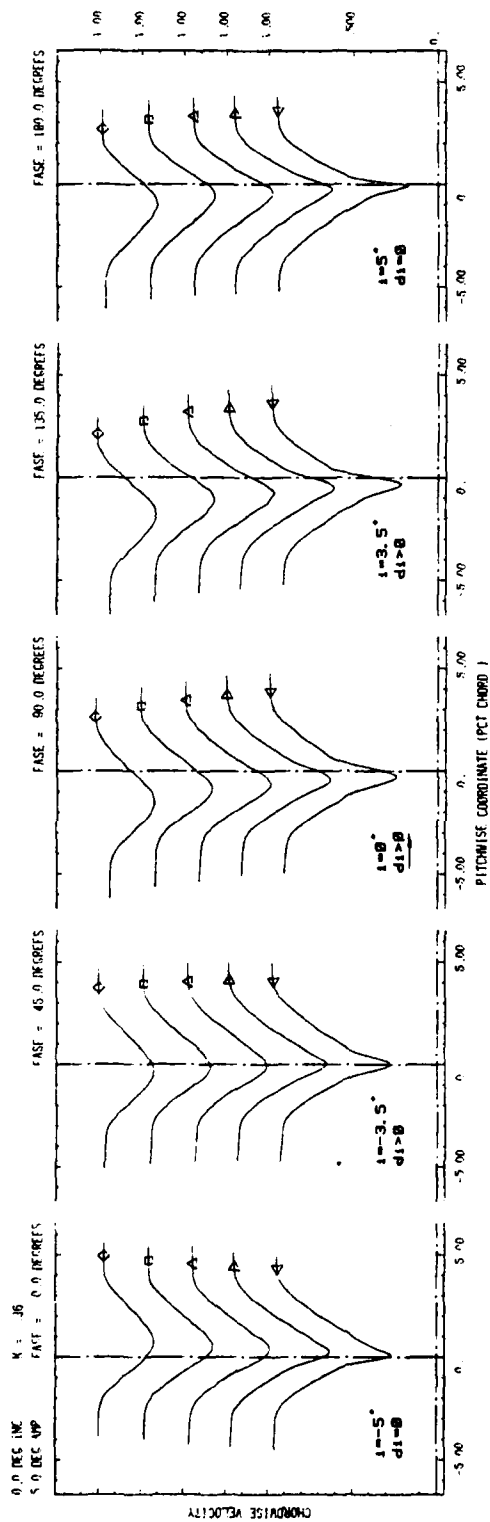


FIGURE 23 : WL05

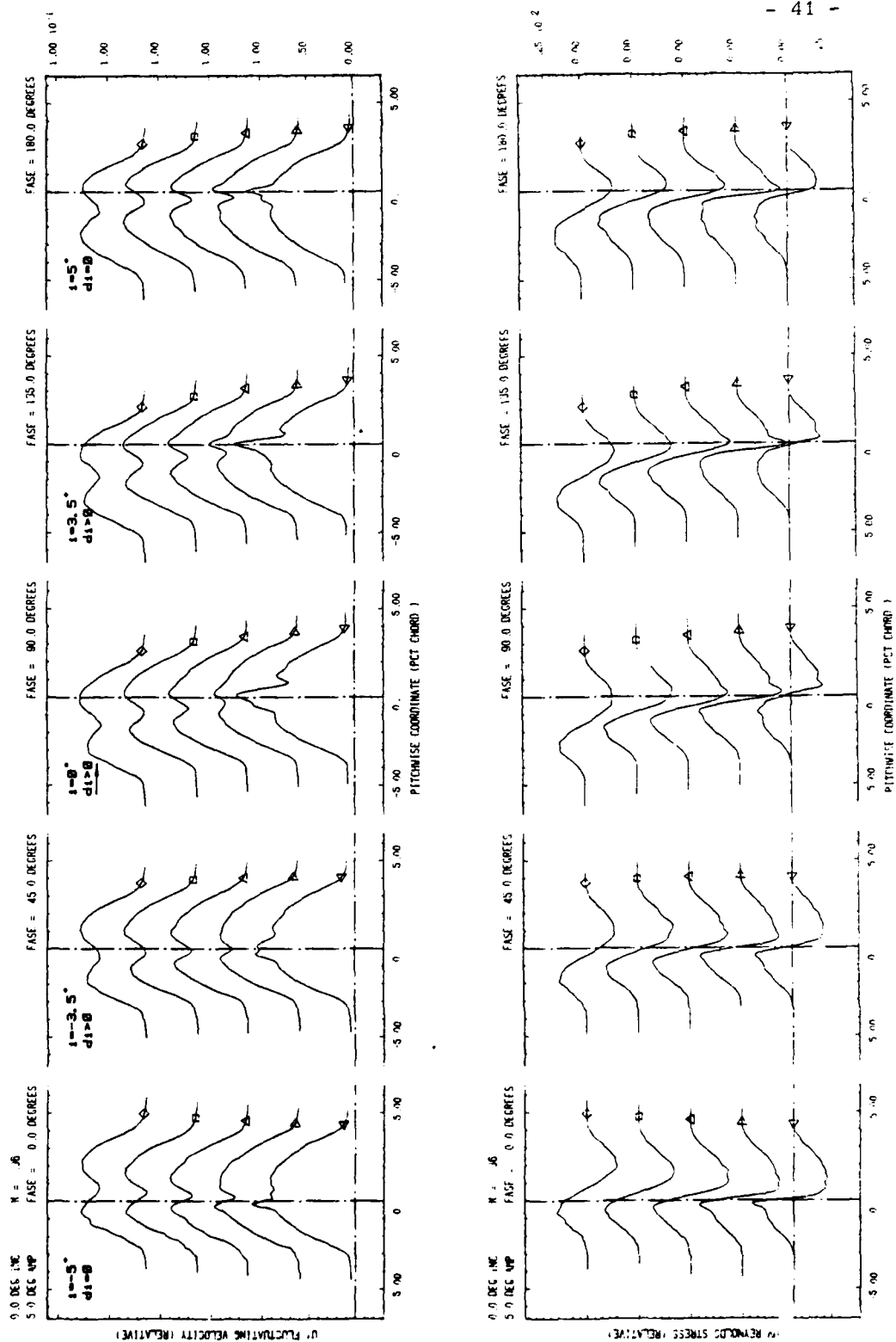


FIGURE 24 : WLO5

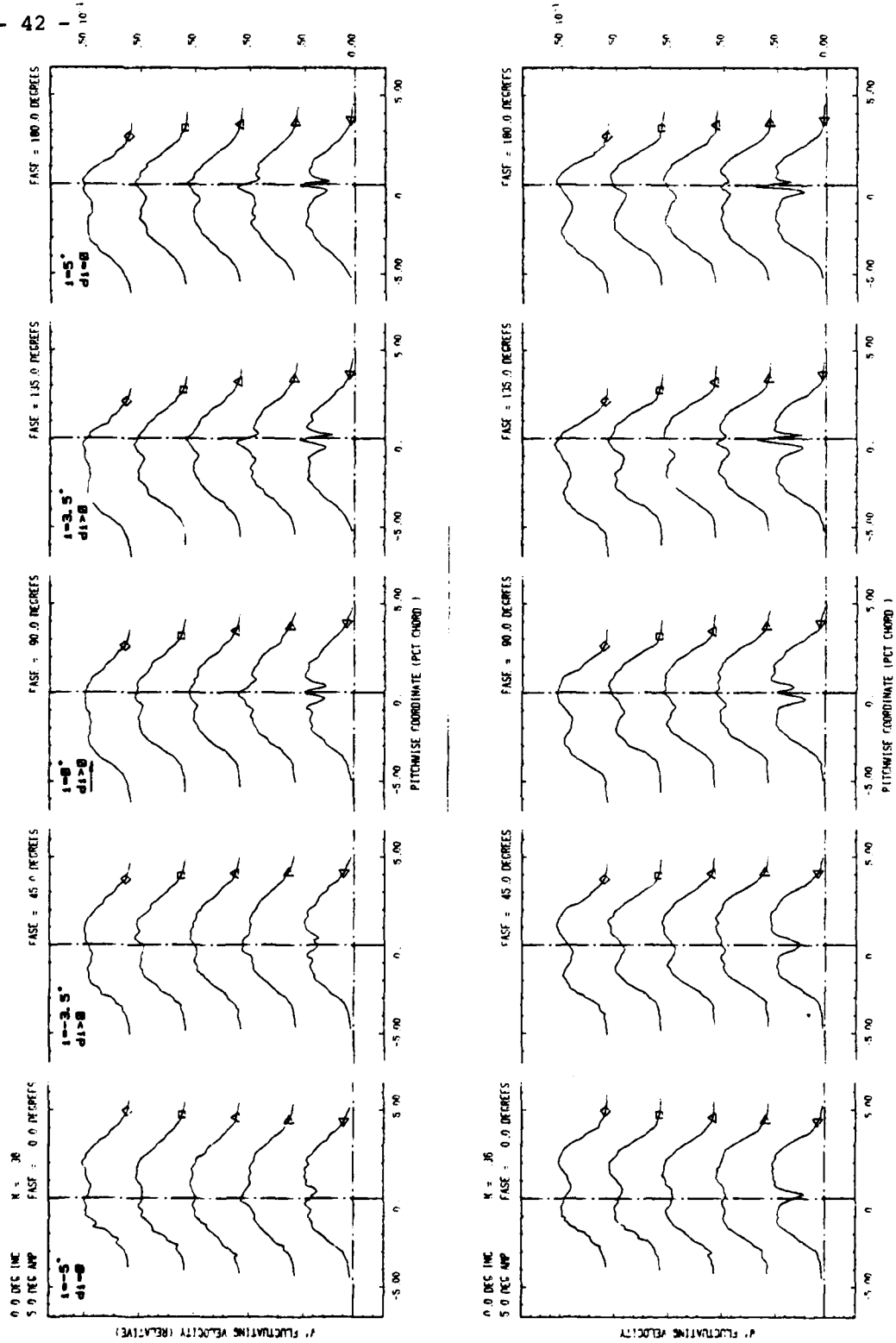


FIGURE 25 : WL05

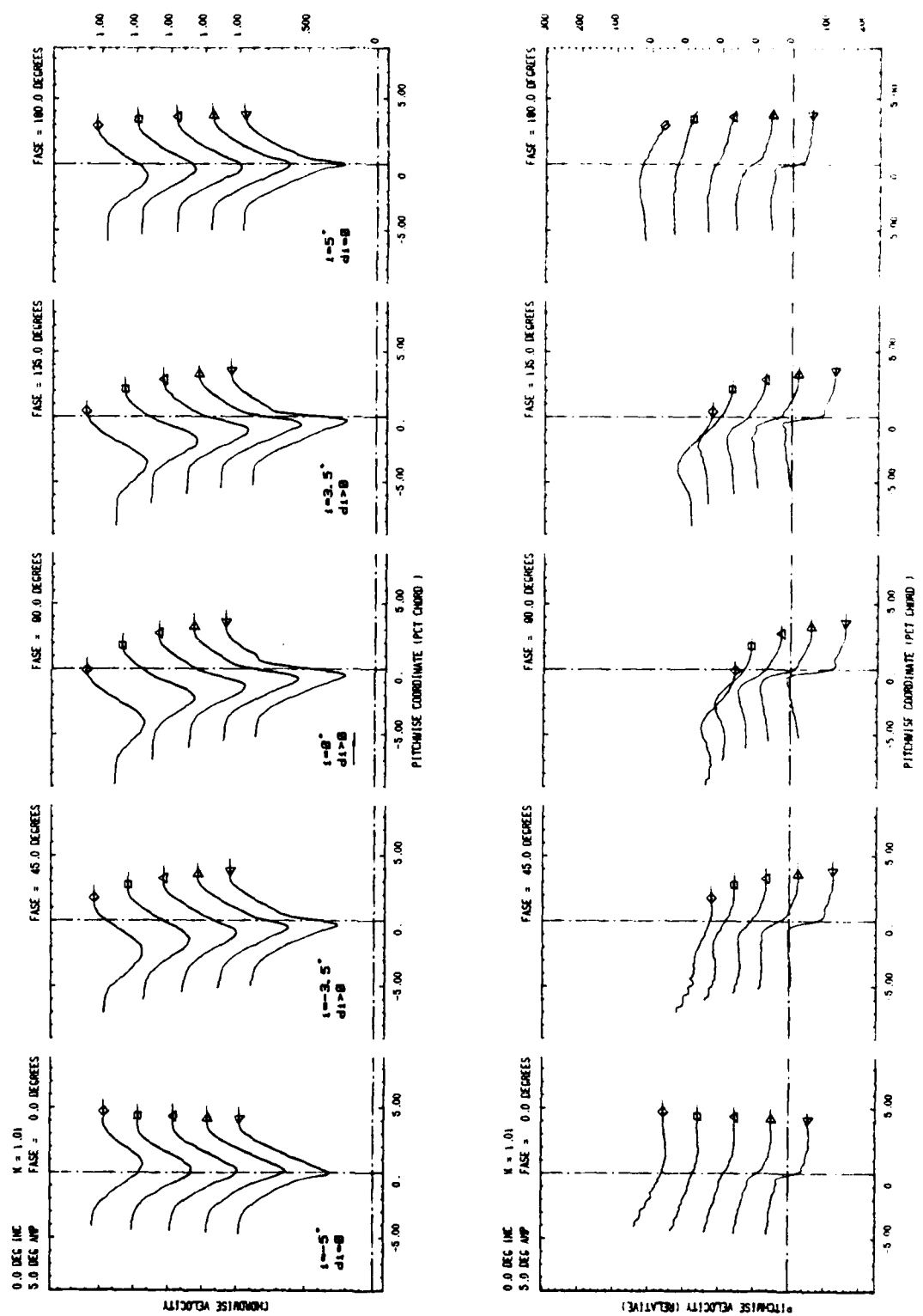


FIGURE 26 : WH05



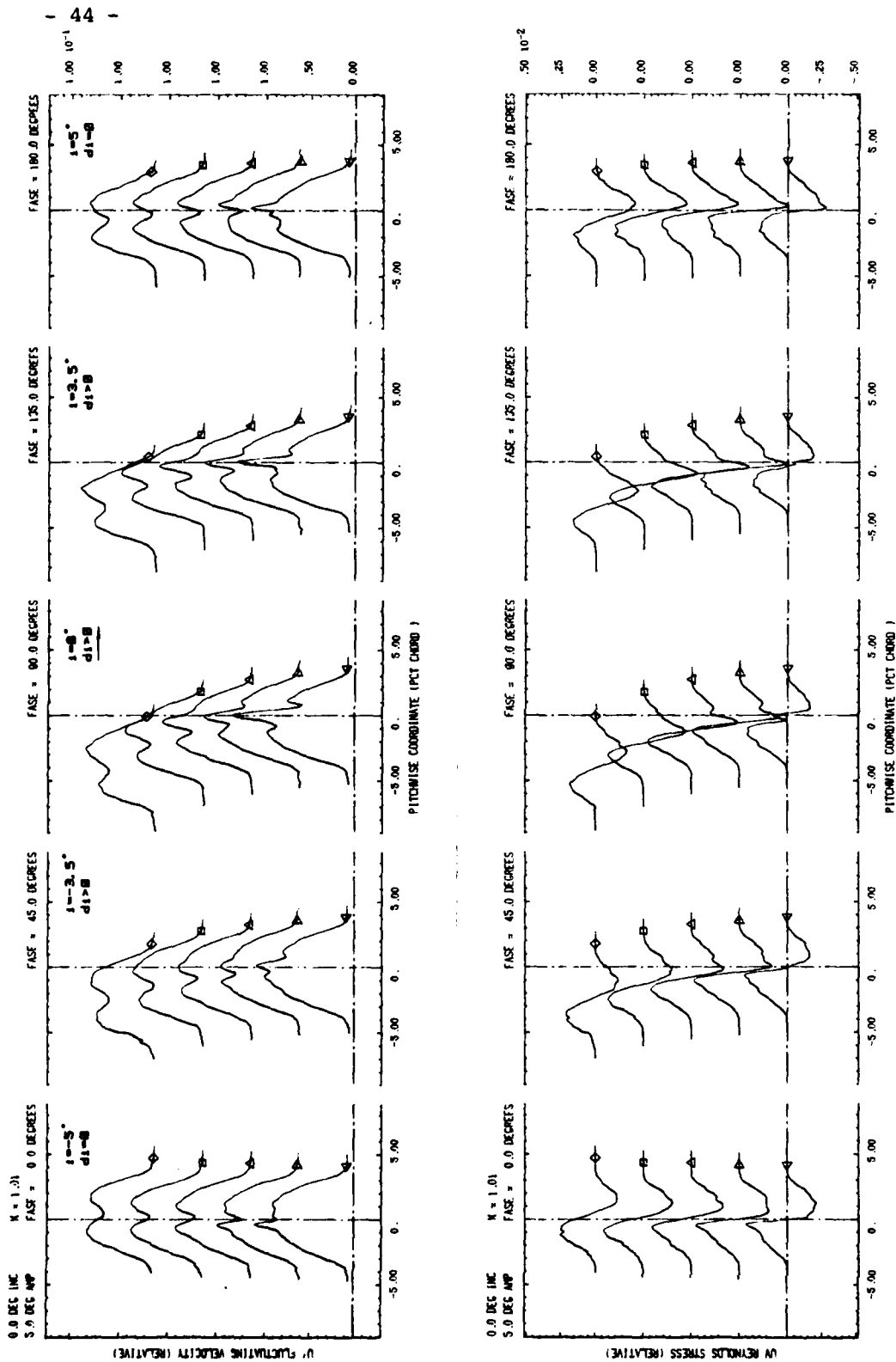


FIGURE 27 : WH05

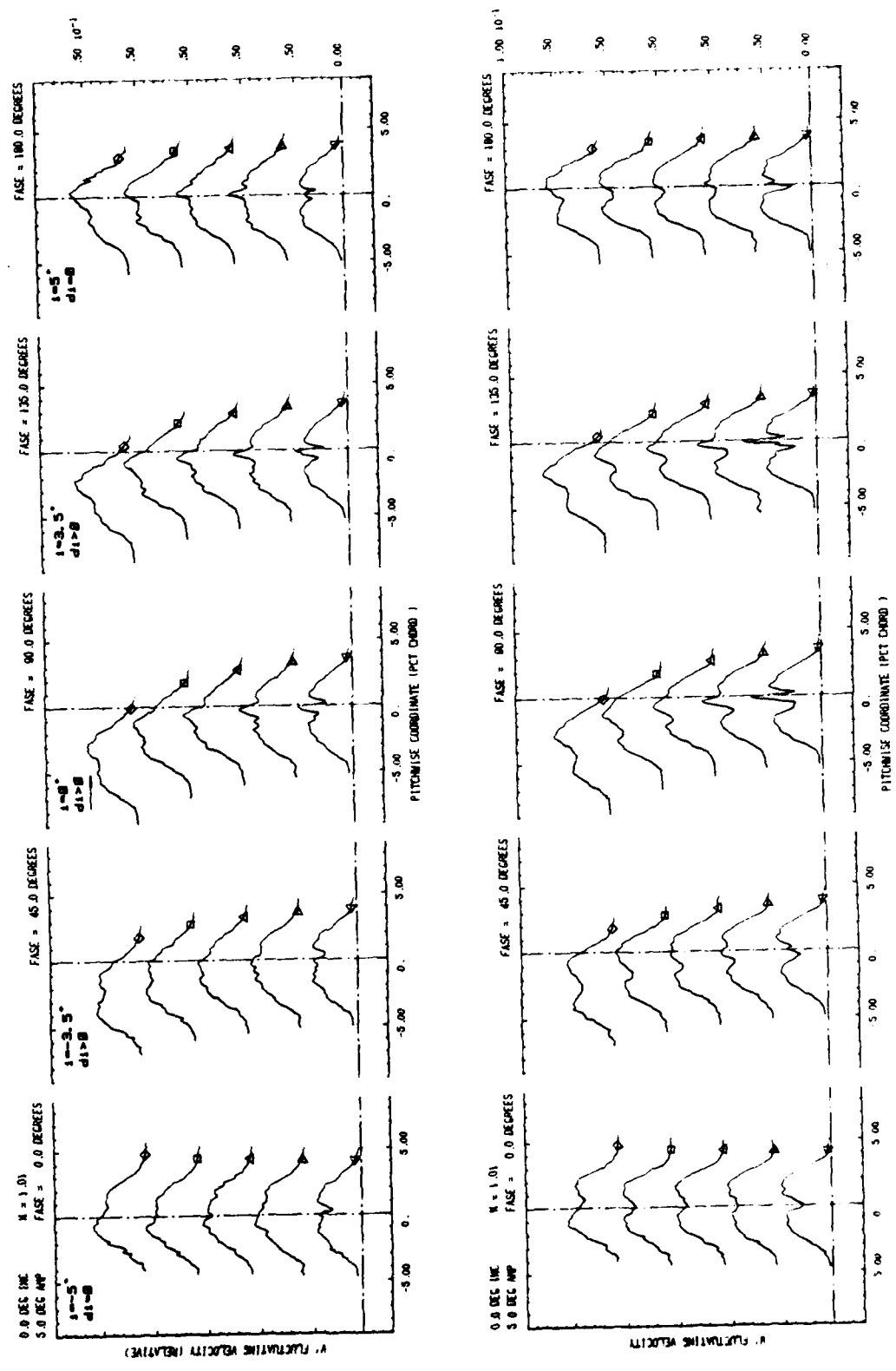


FIGURE 28 : WB05

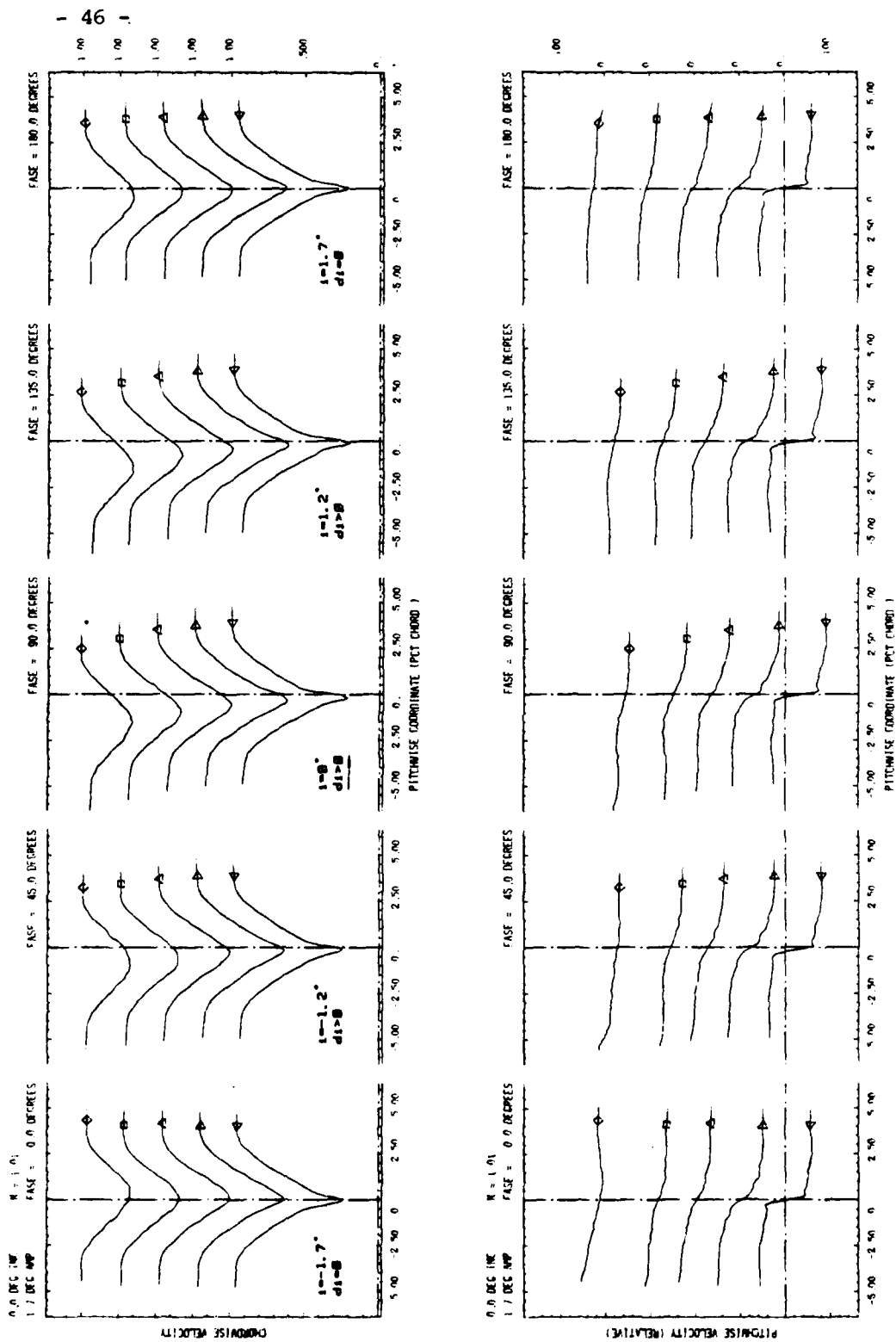


FIGURE 29 : WHO1

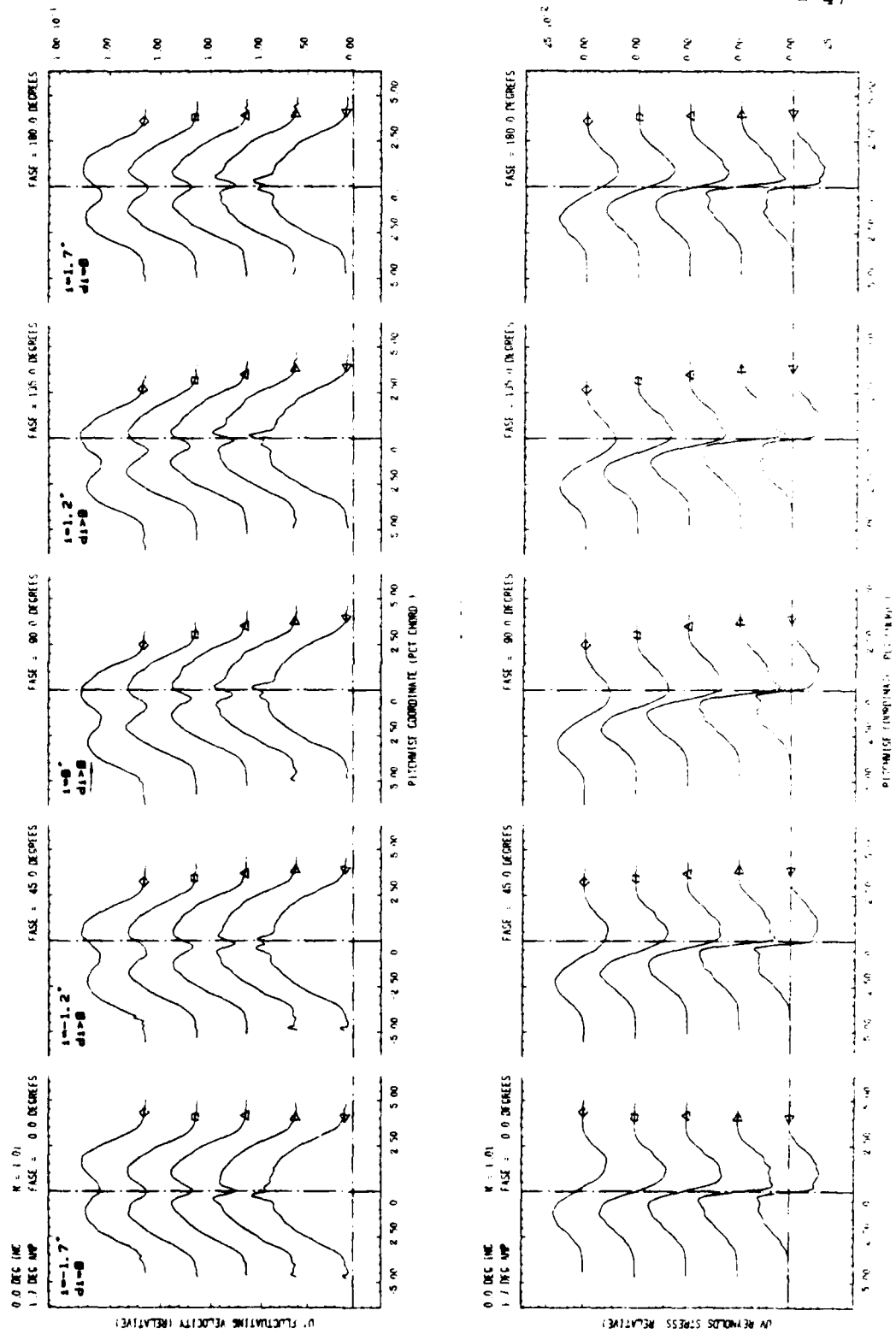


FIGURE 30 : WH01

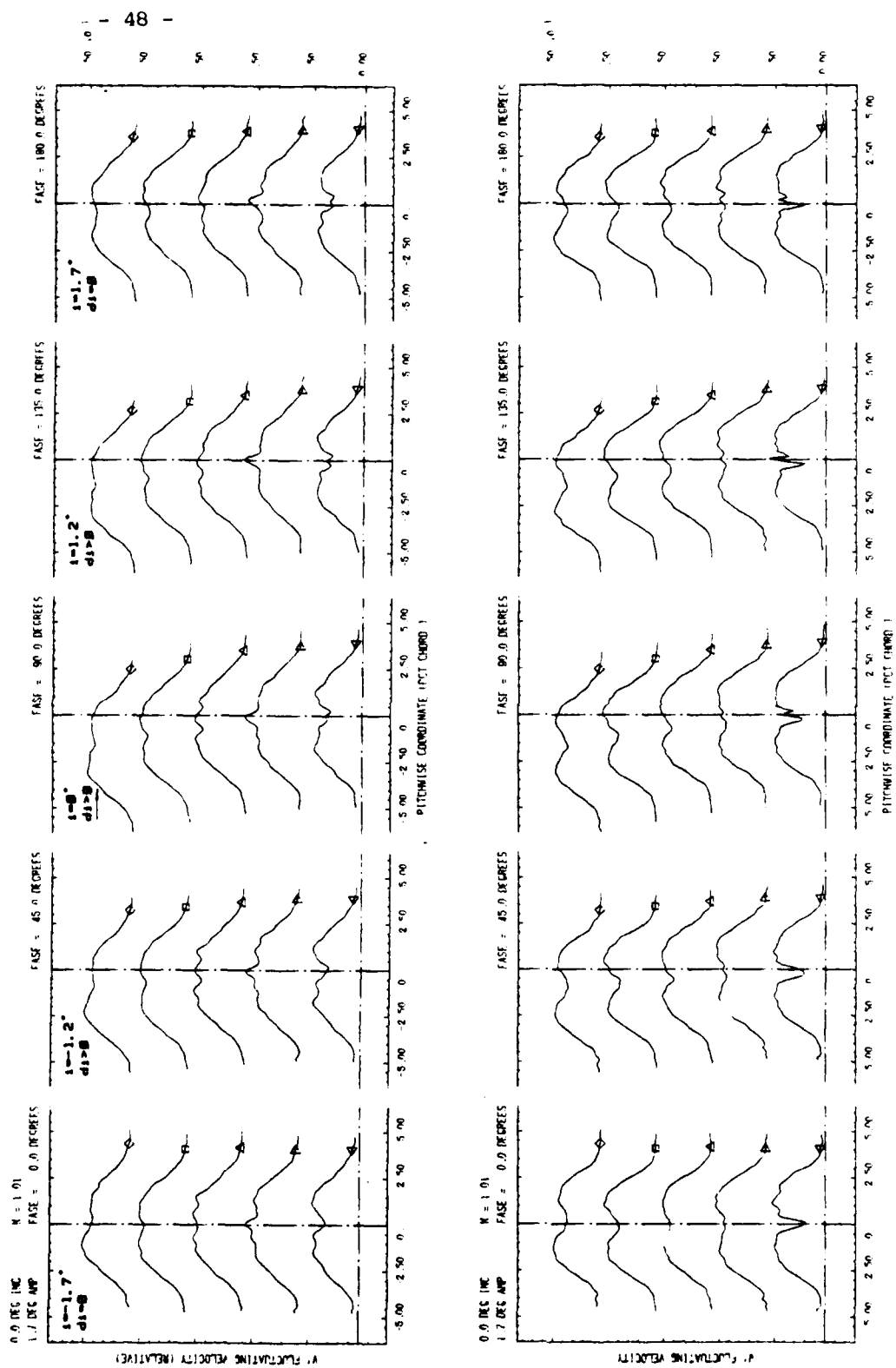


FIGURE 31 : WH01

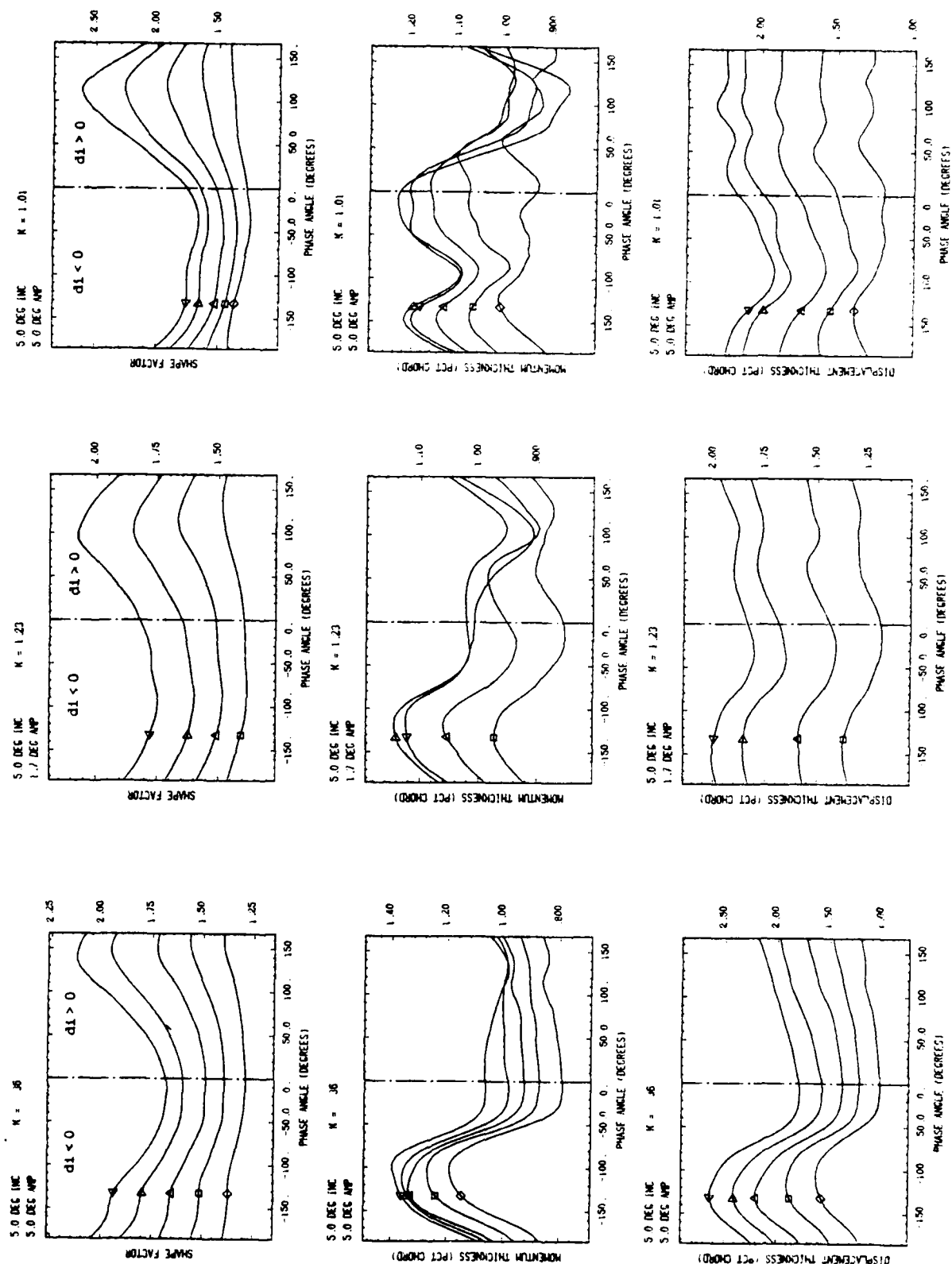


FIGURE 32 : WL55, WH51 and WH55

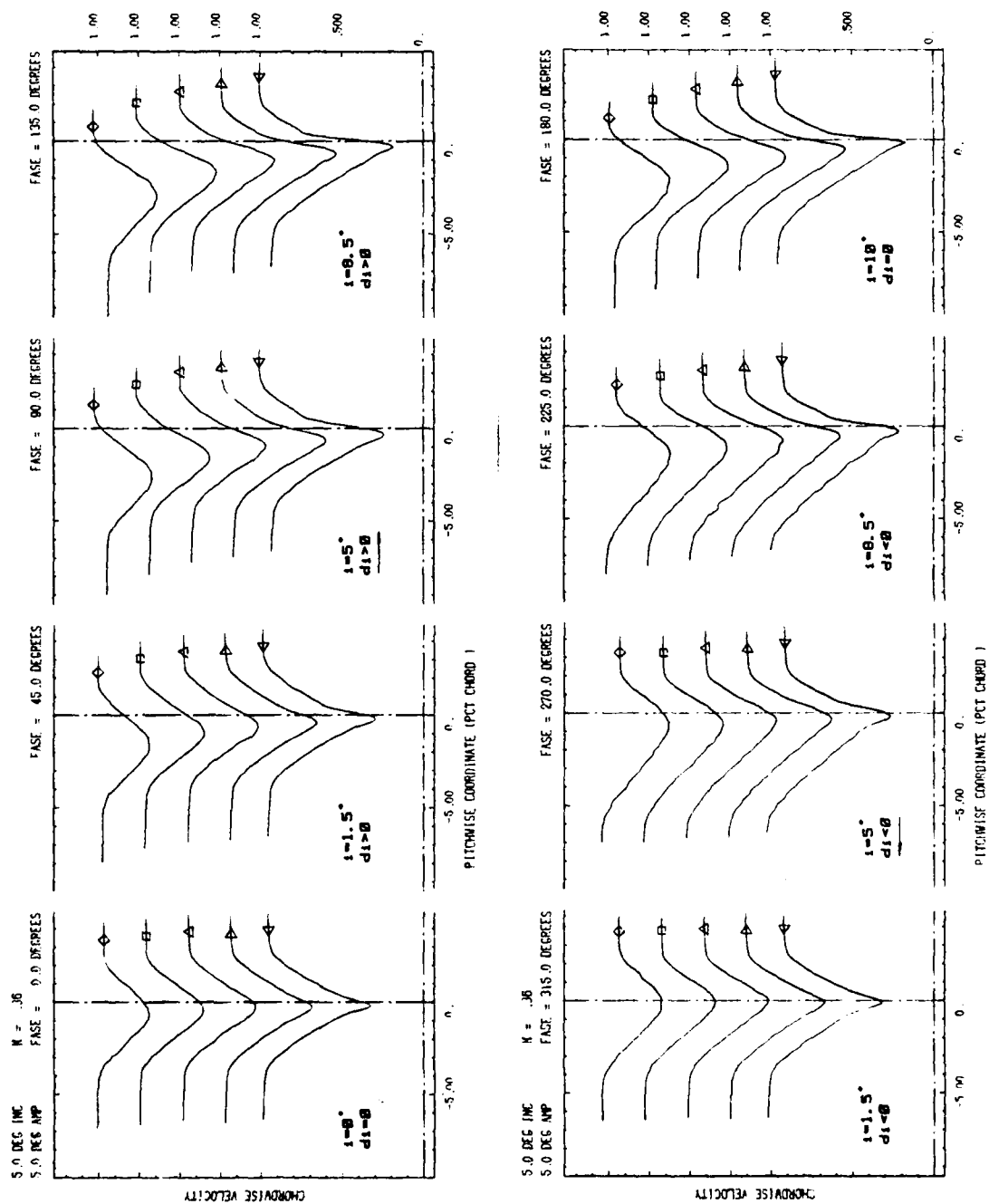


FIGURE 33 : WL55

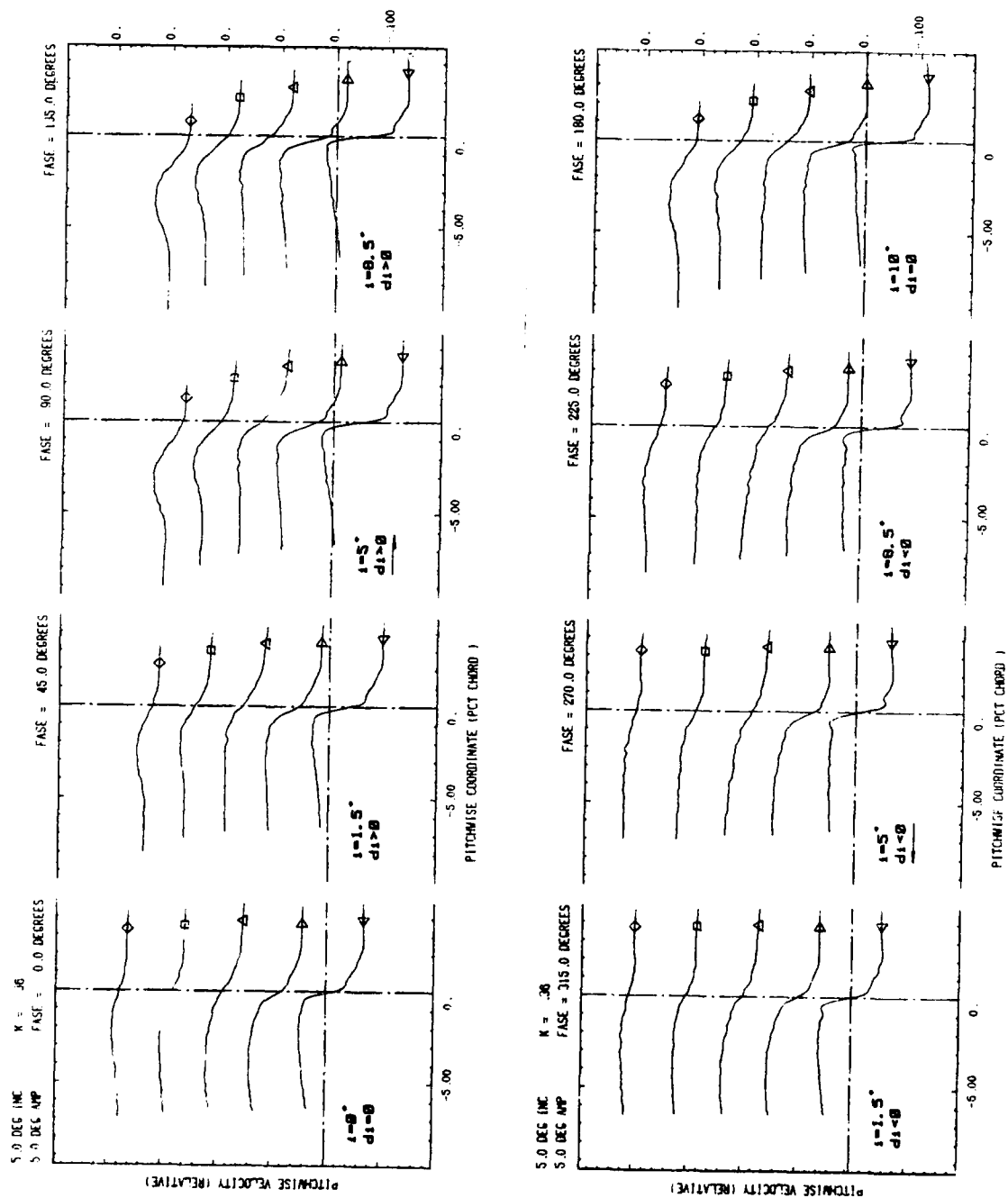


FIGURE 34 : WL55



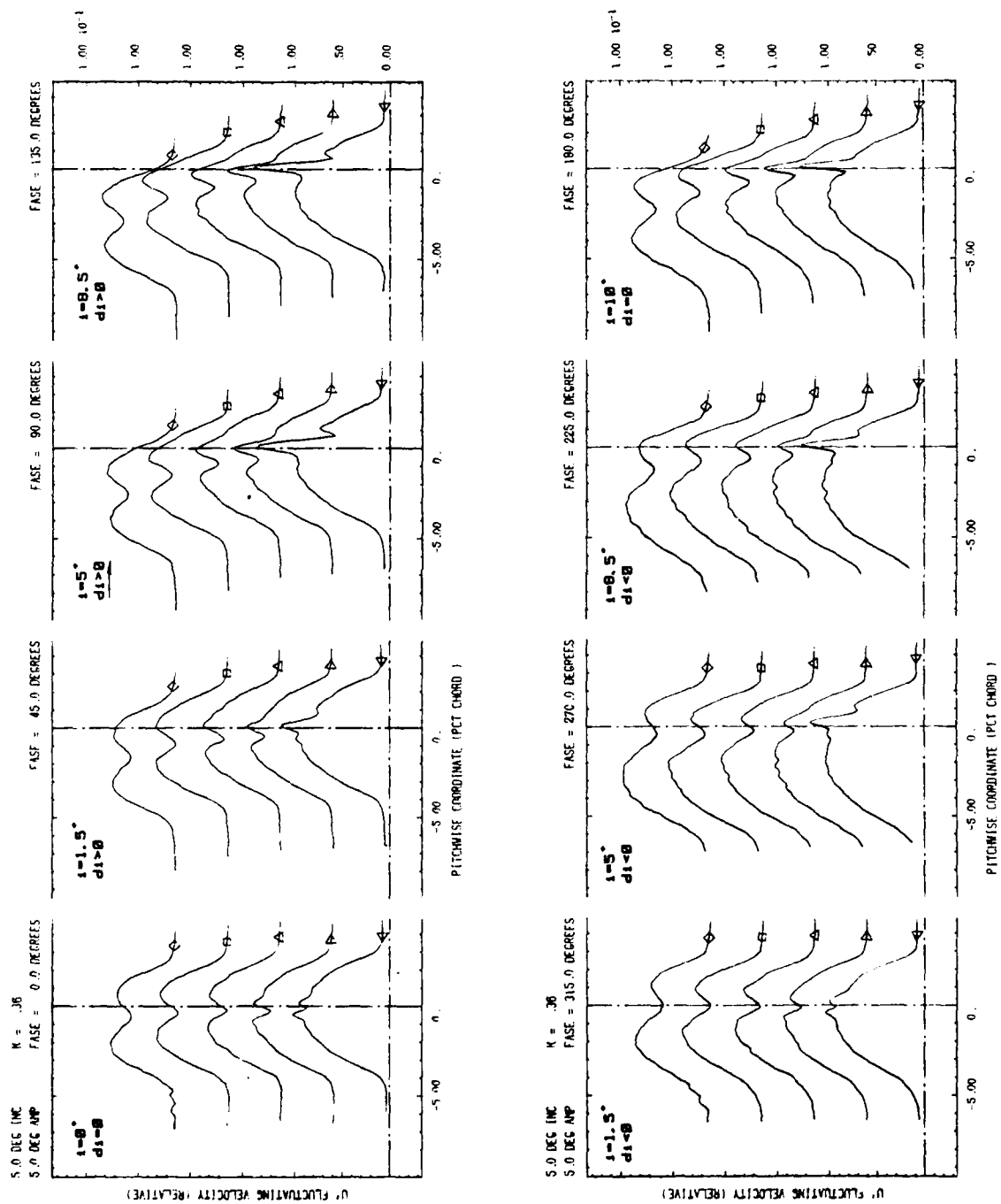


FIGURE 35 : WL55

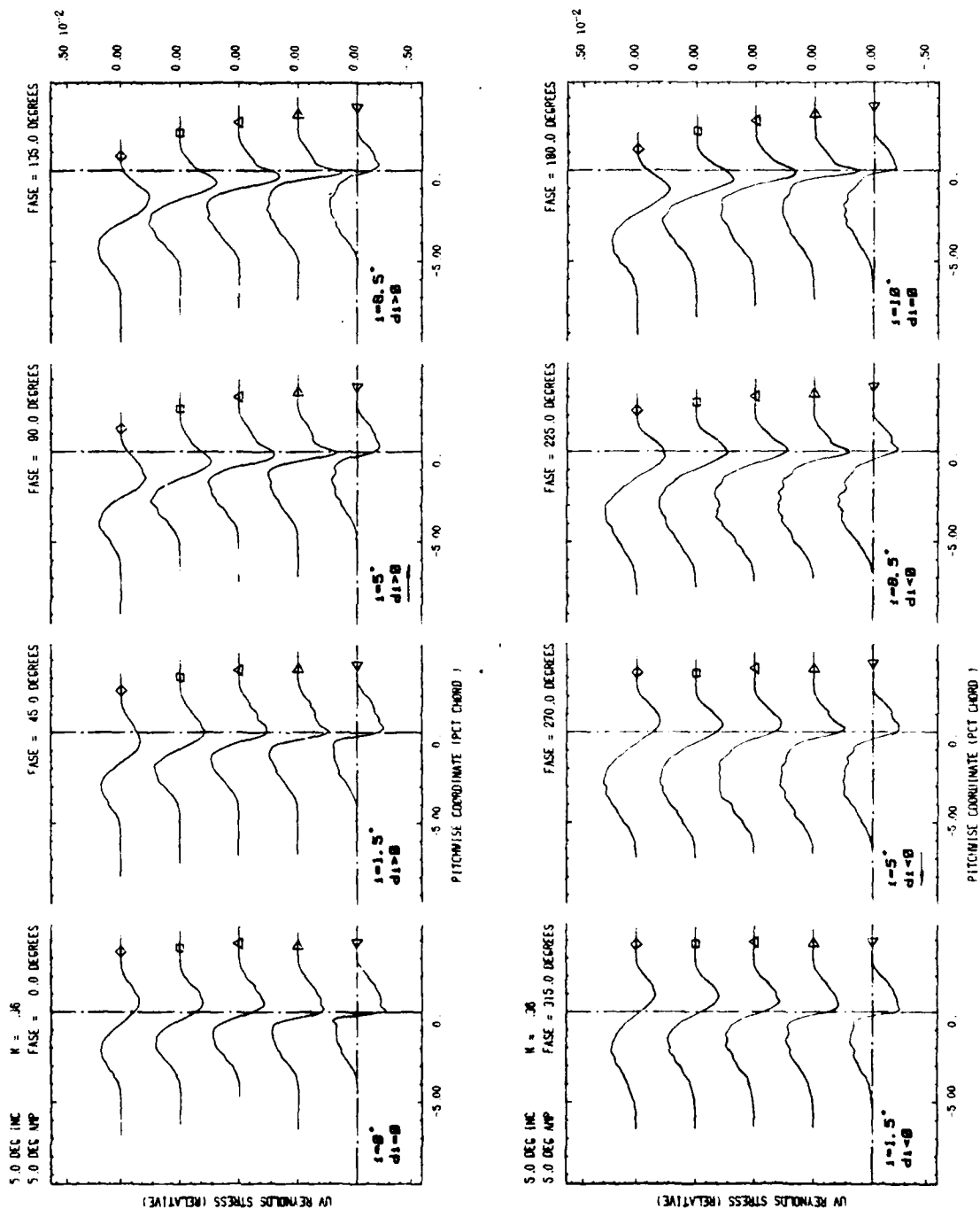


FIGURE 36 : WL55

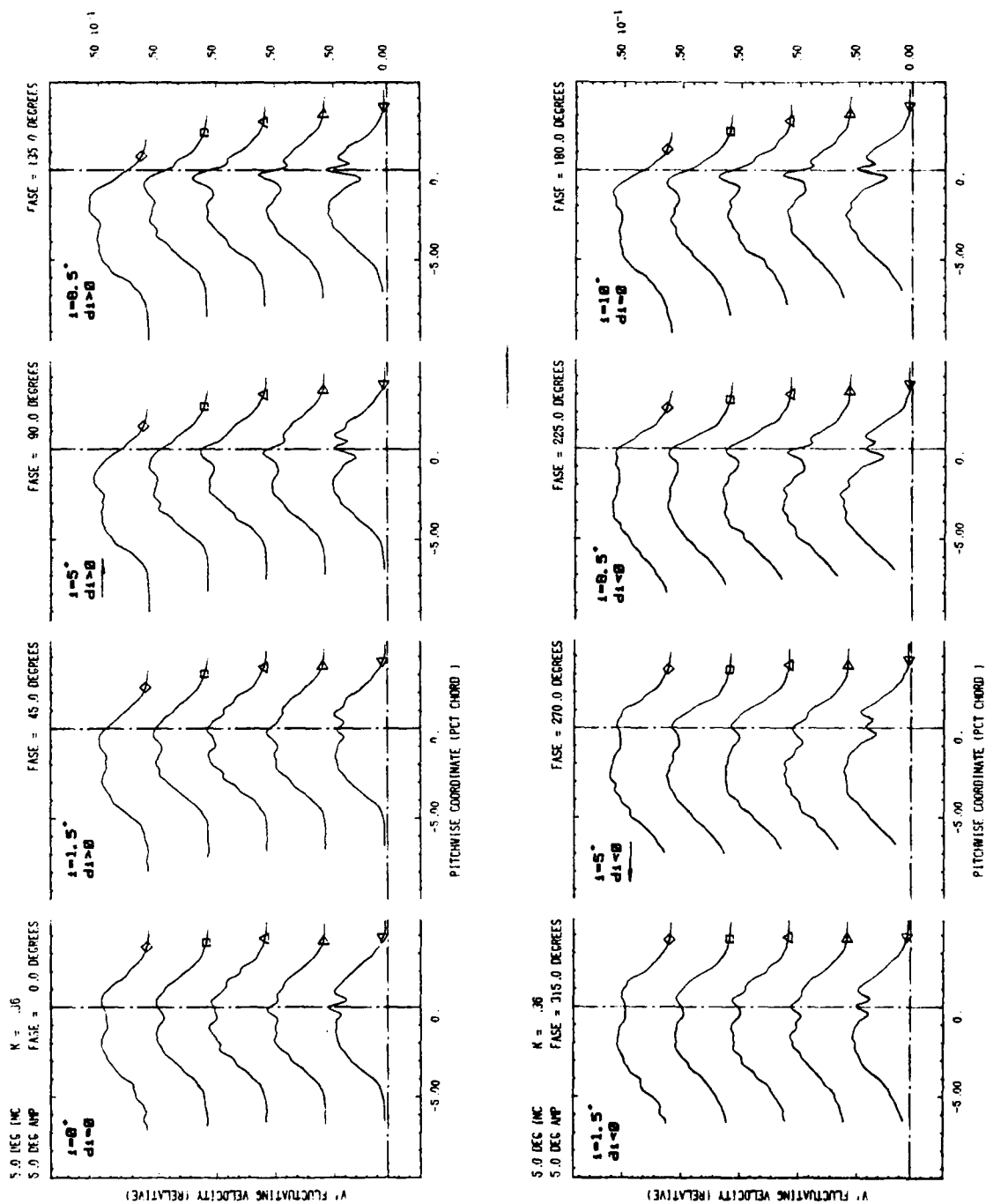


FIGURE 37 : WL55

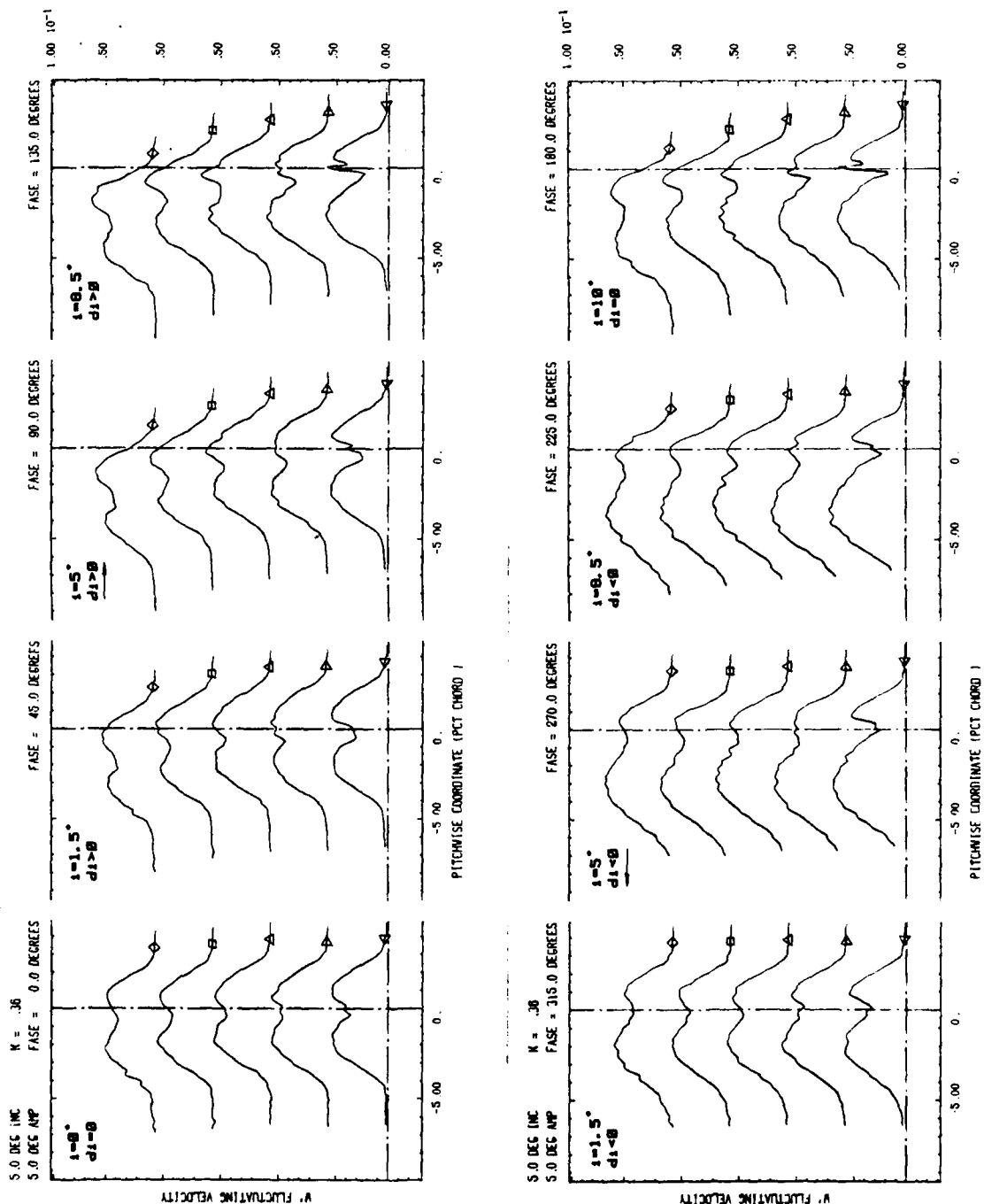


FIGURE 38 : WL55

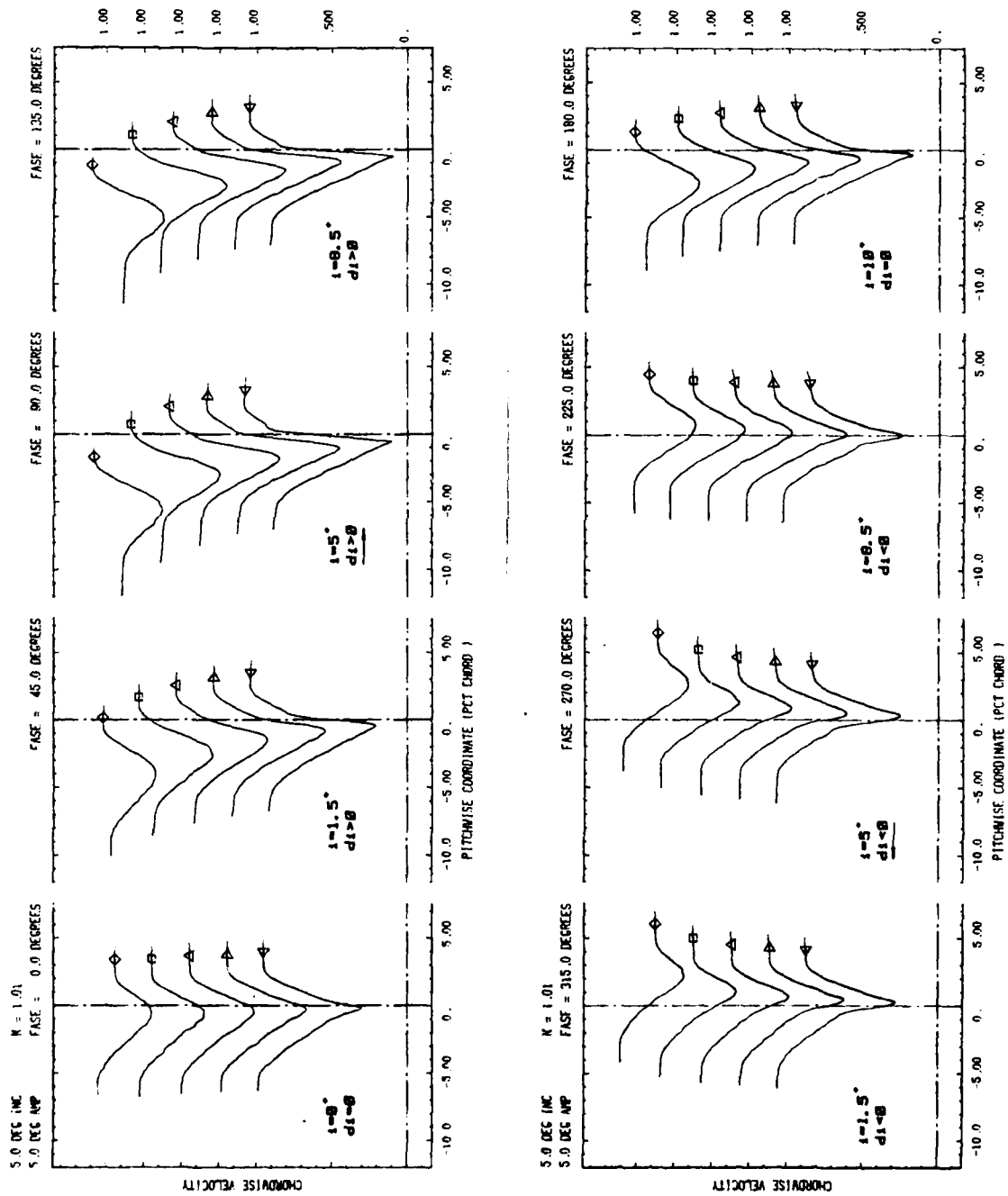


FIGURE 39 : WH55

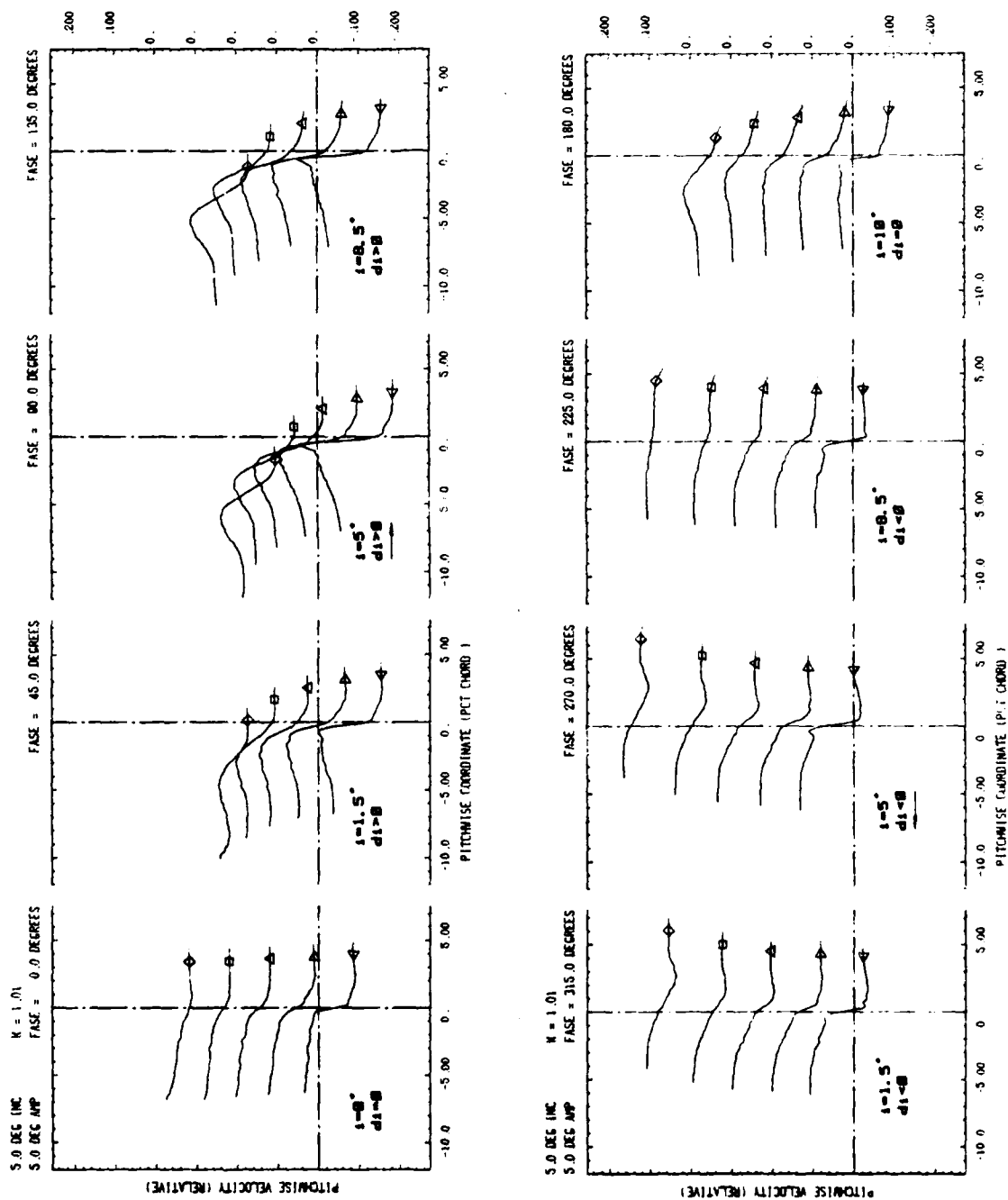


FIGURE 40 : WH55

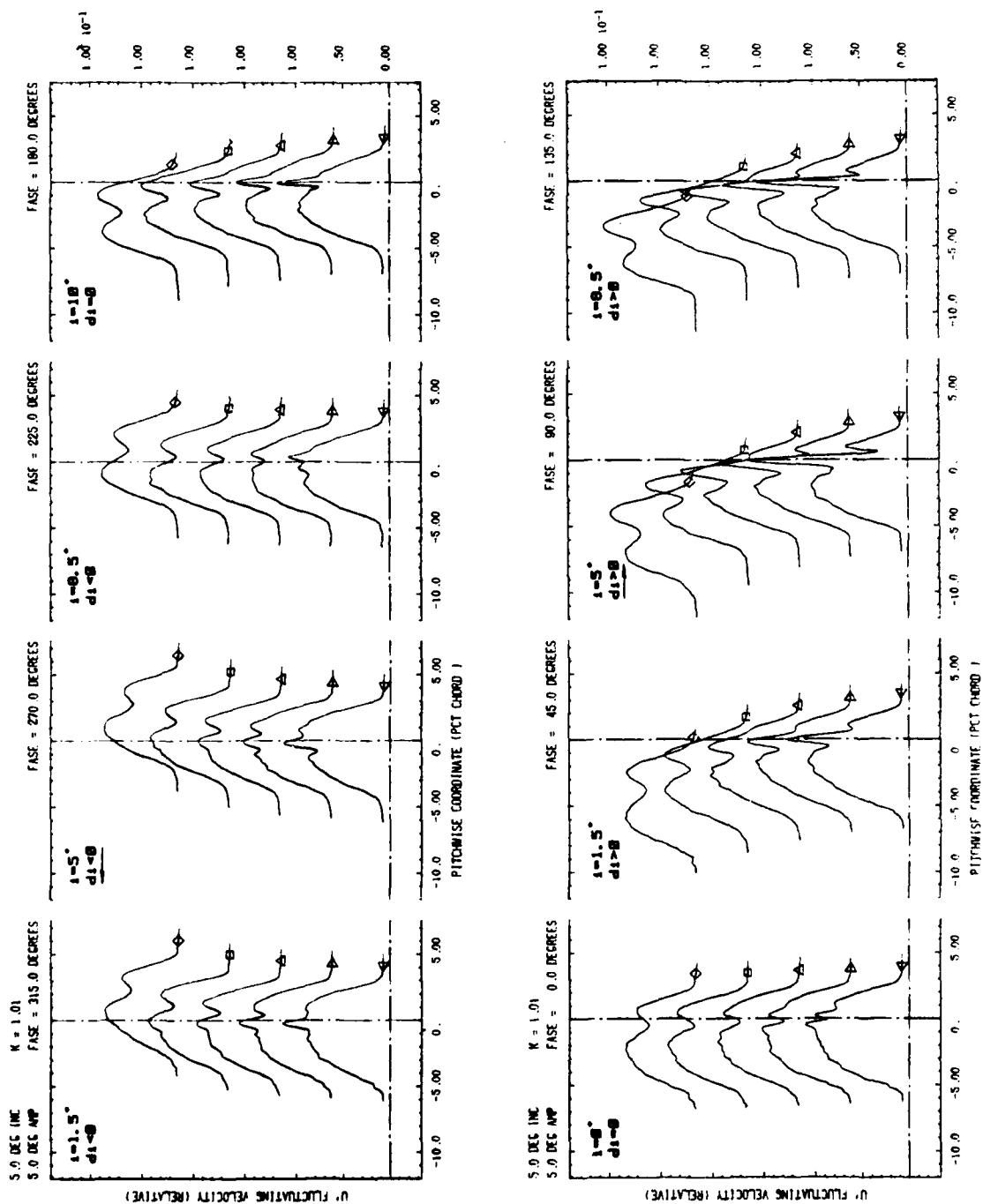


FIGURE 41 : WH55

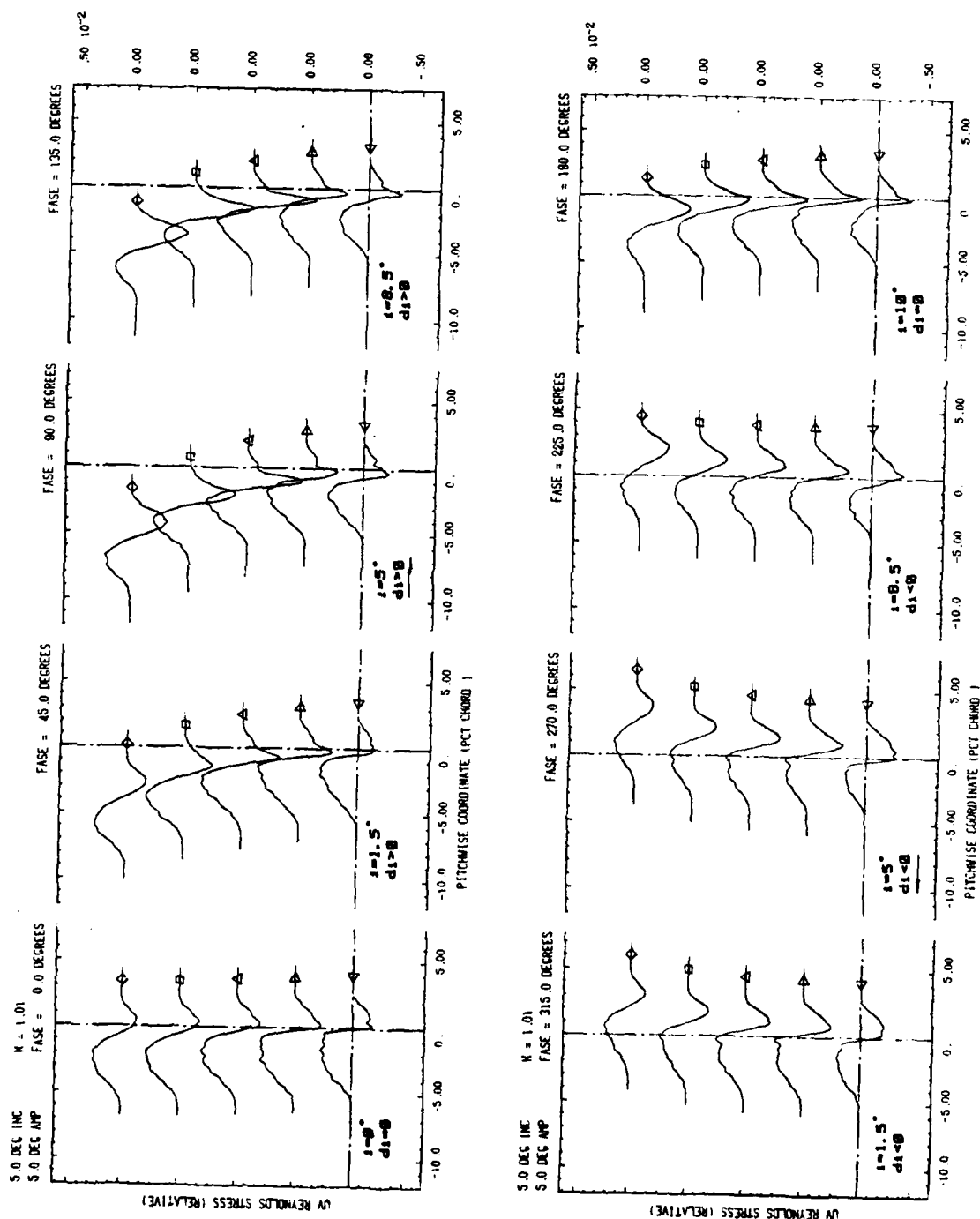


FIGURE 42 : WH55



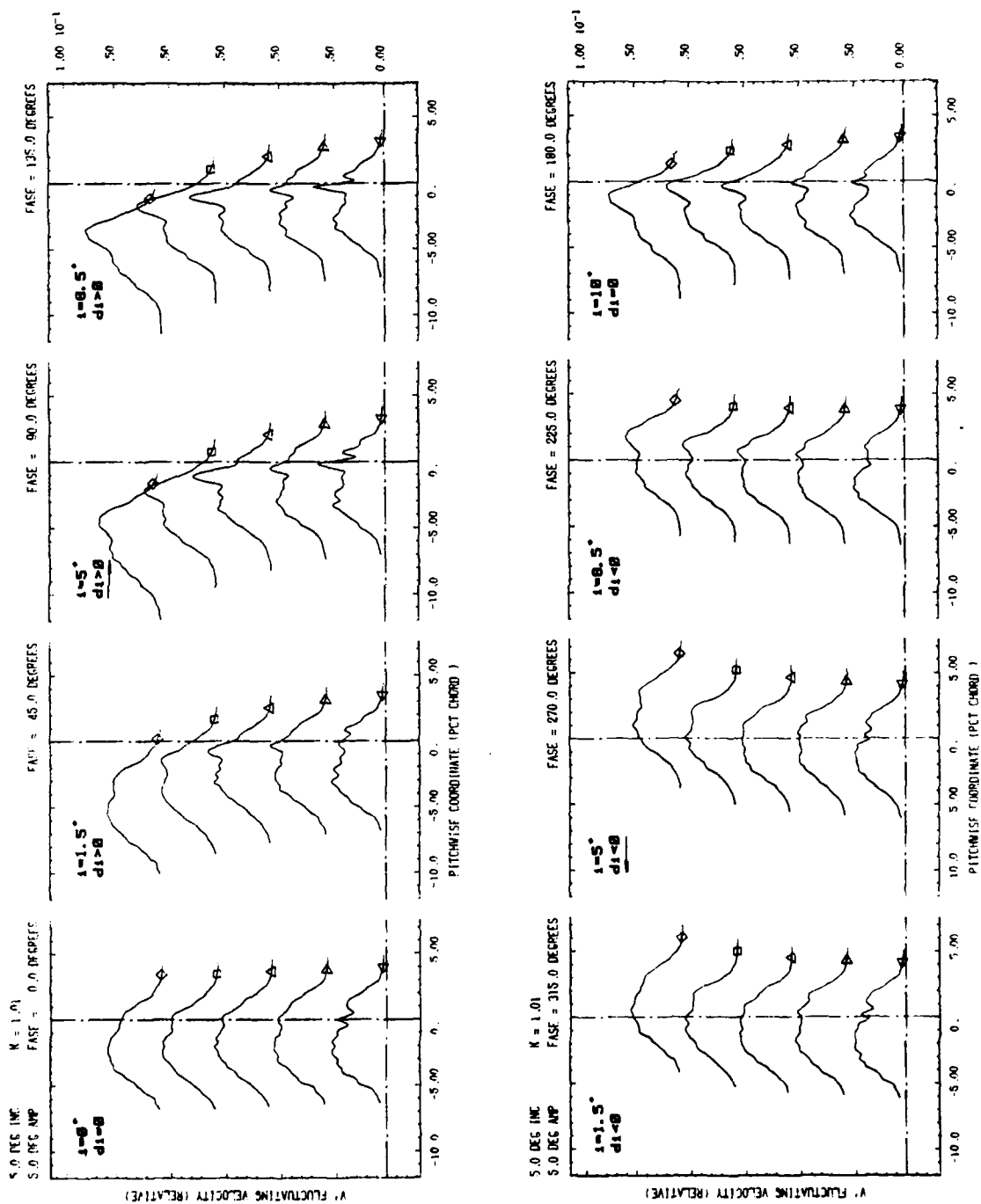


FIGURE 43 : WH55

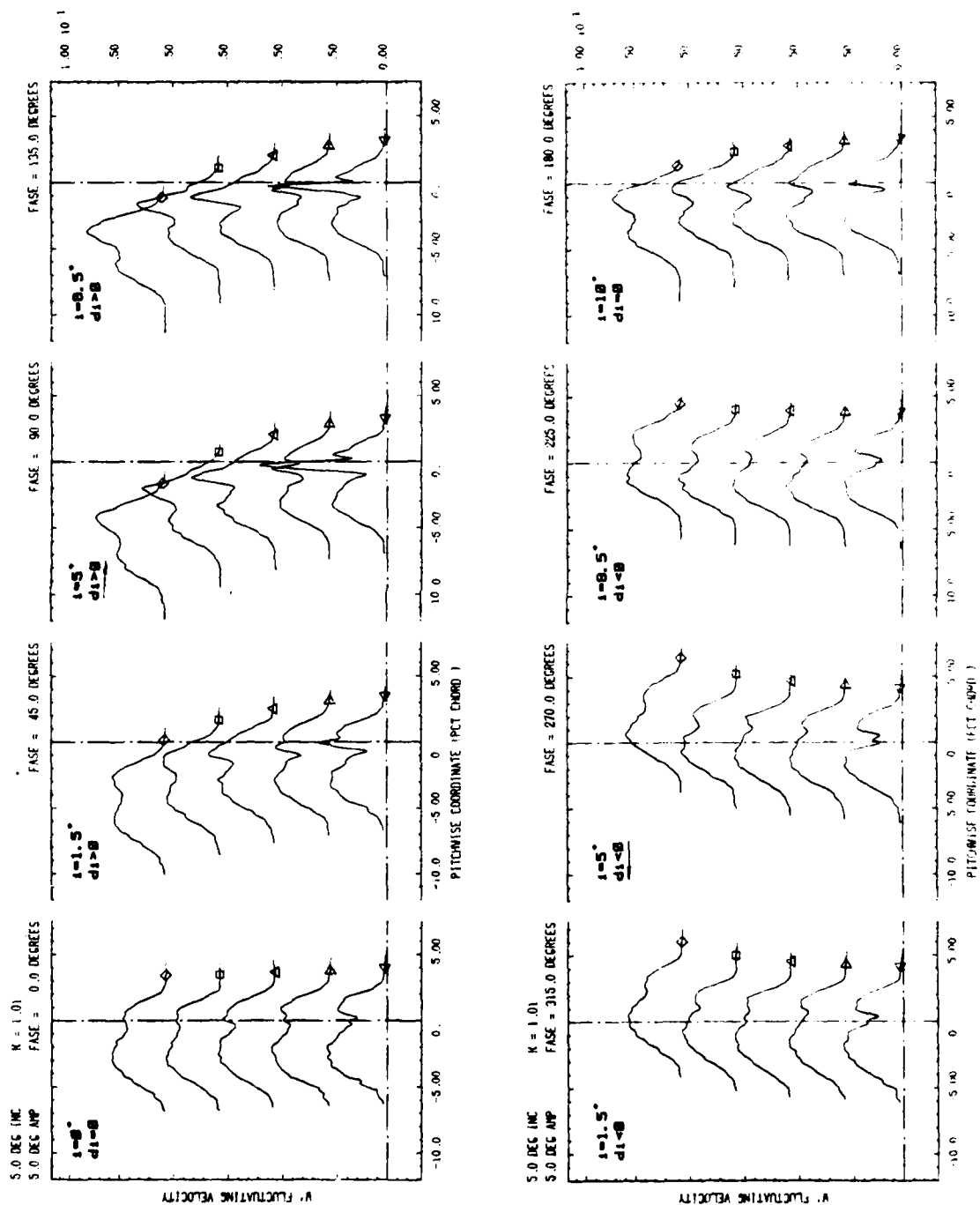


FIGURE 44 : WH55

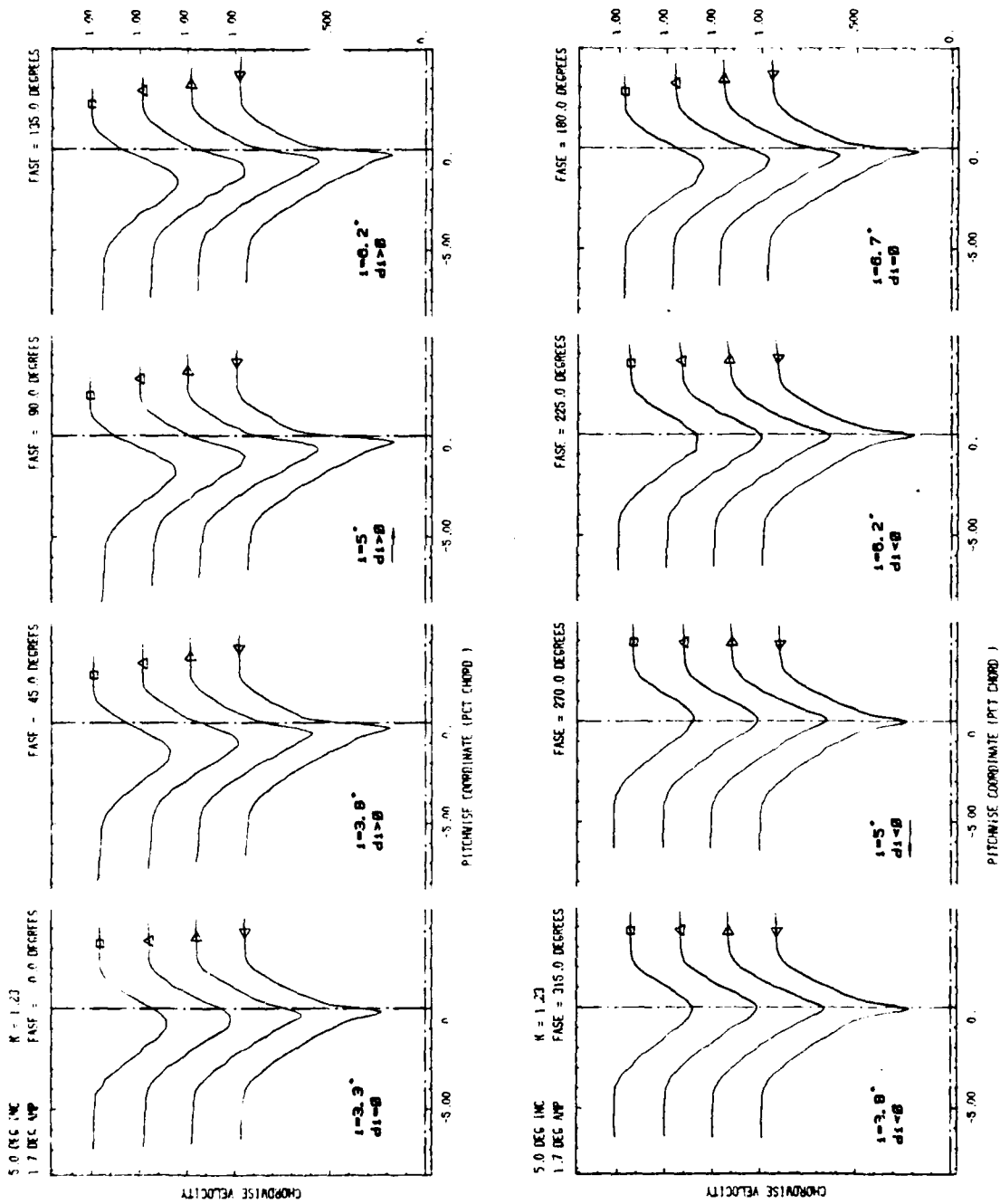


FIGURE 45 : WH51

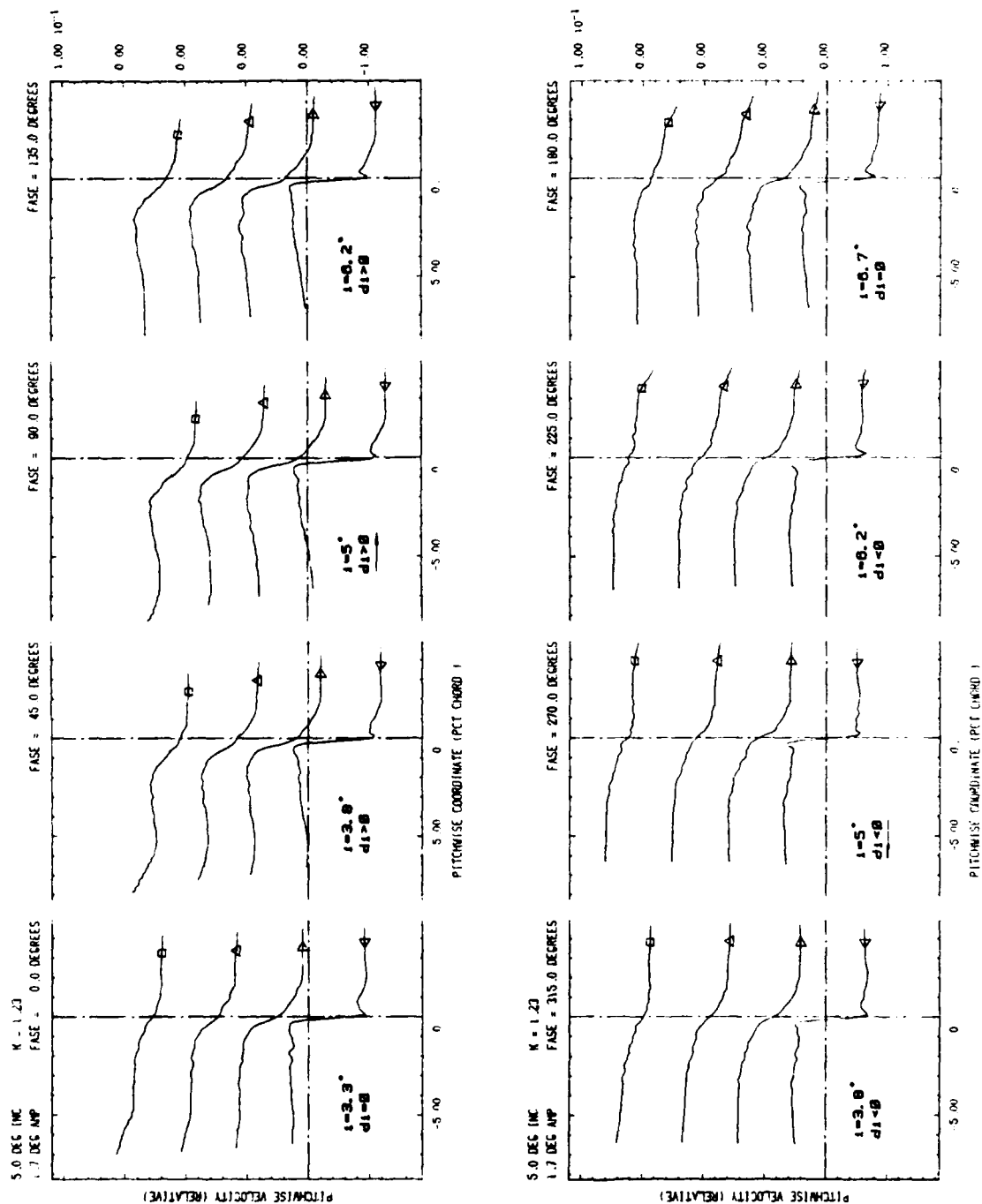


FIGURE 46 : WH51

FIGURE 47 : WH51

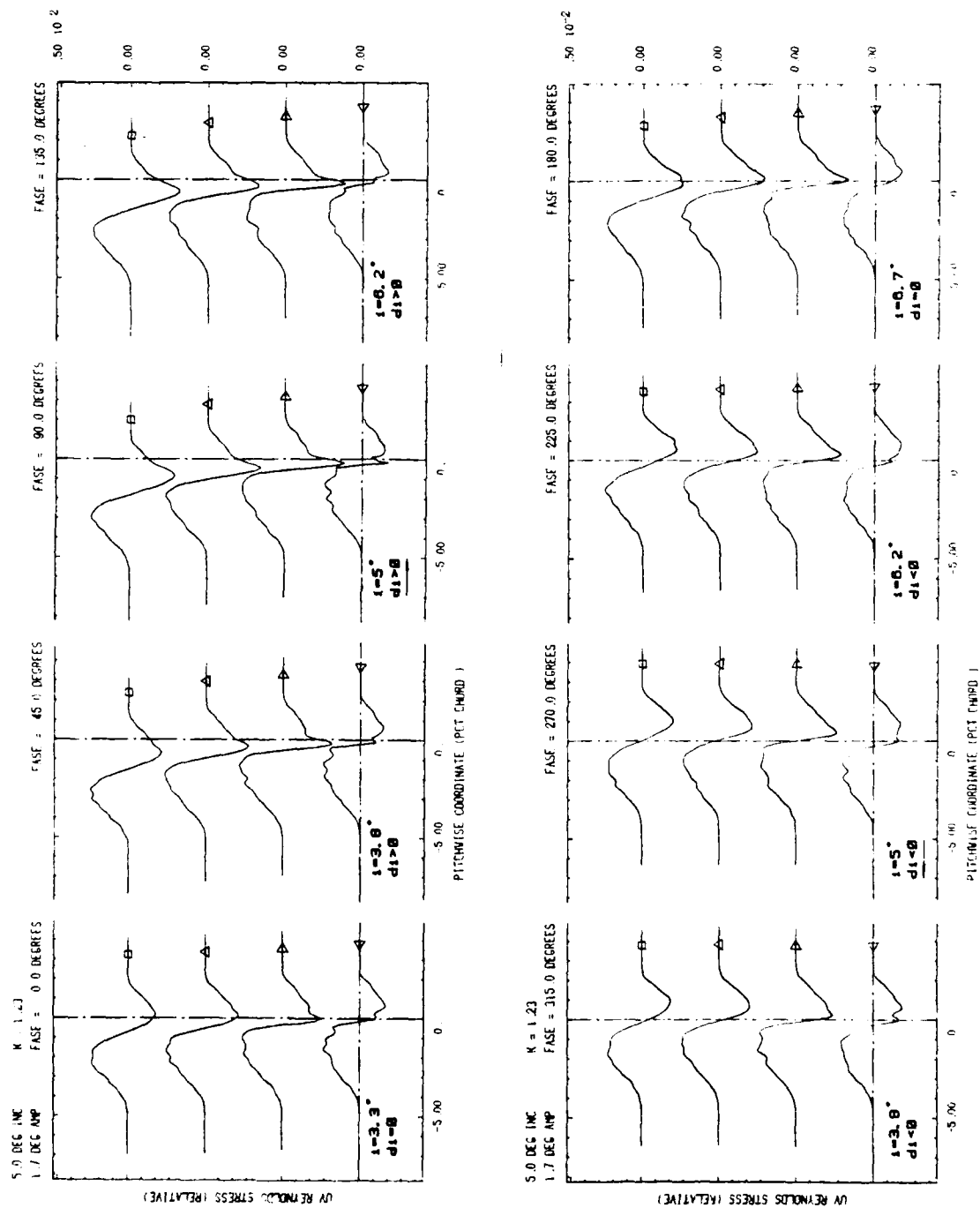


FIGURE 48 : WH51

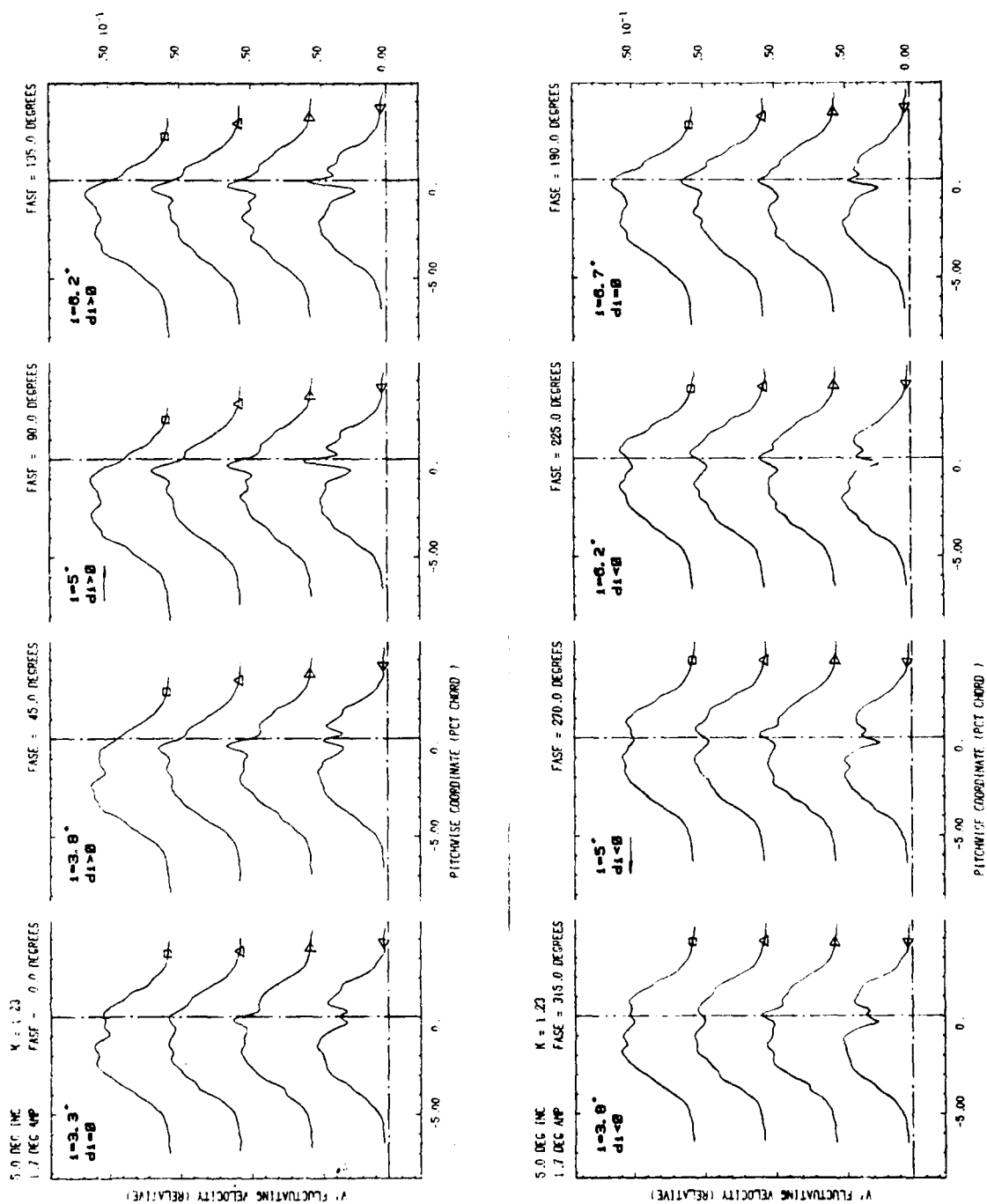


FIGURE 49 : WH51

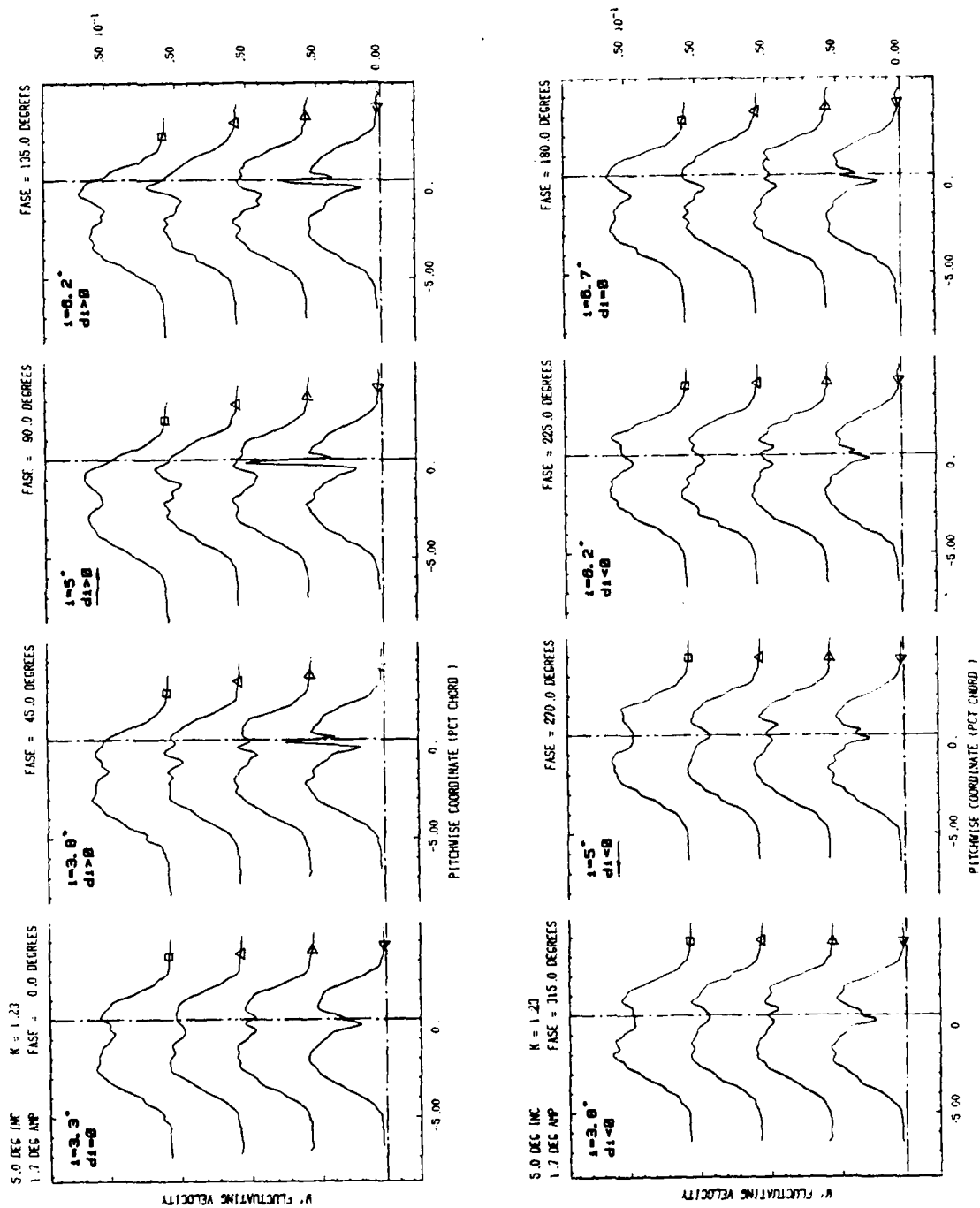


FIGURE 50 : WH51



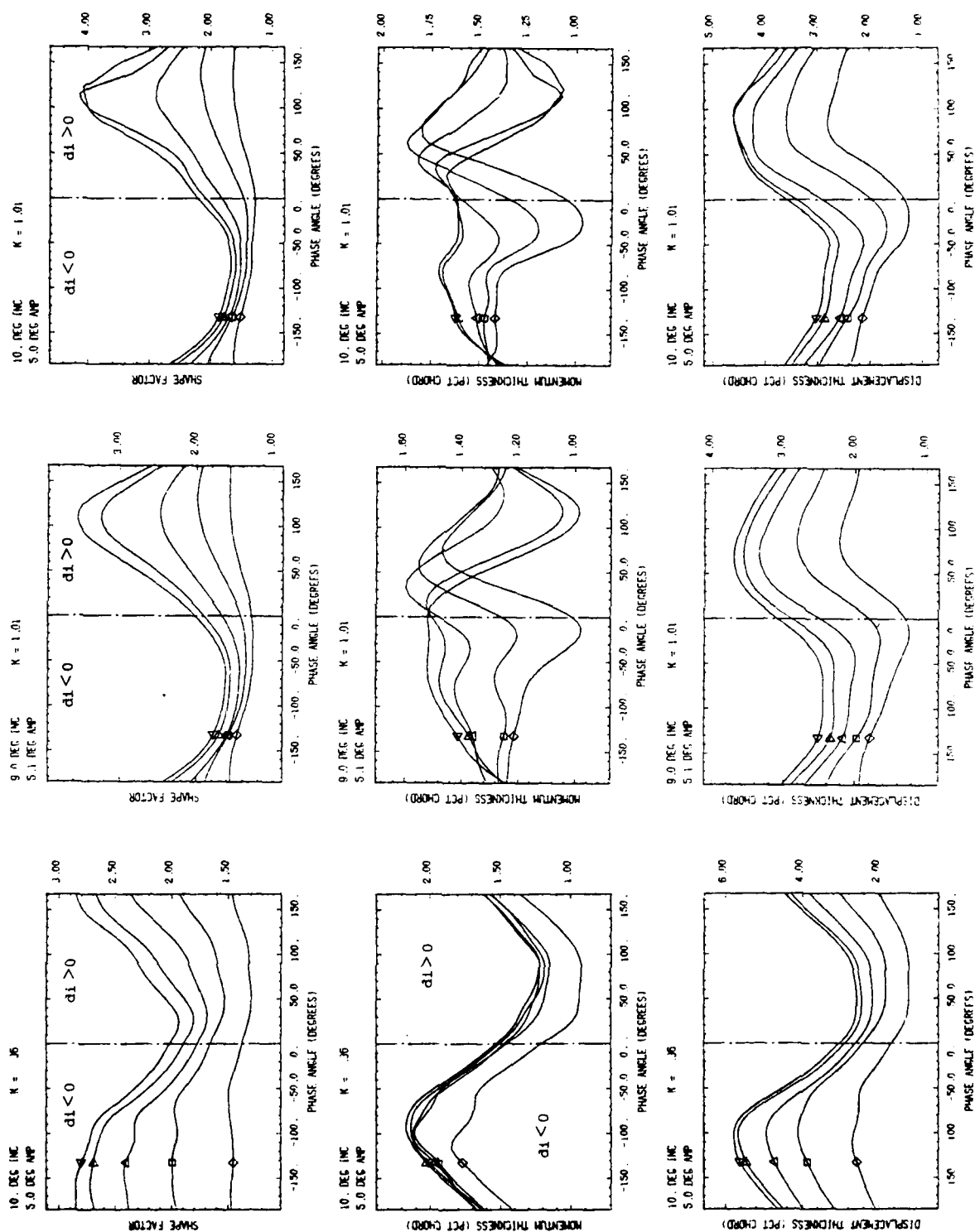


FIGURE 51 : WLA5, WH95 and WHA5

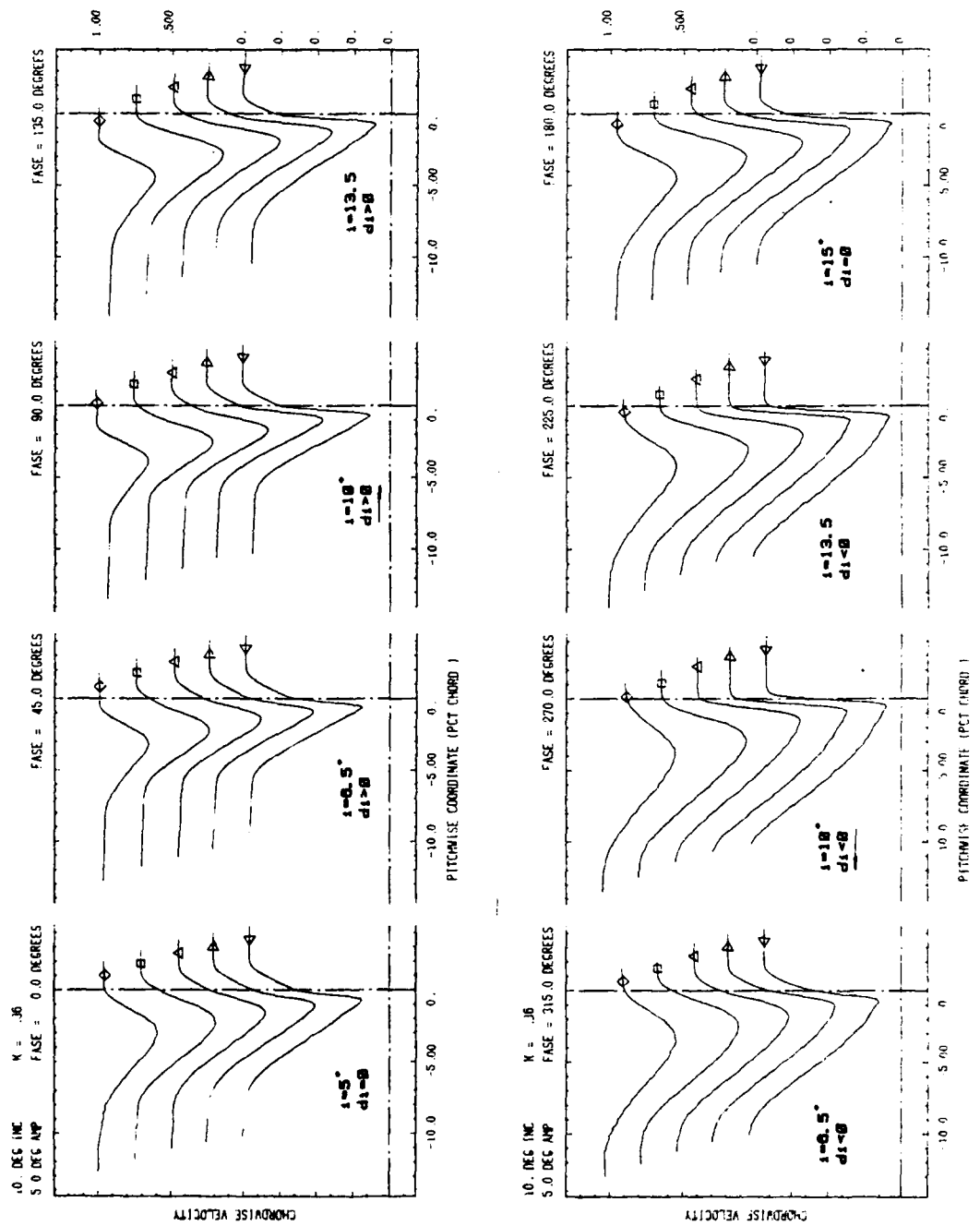


FIGURE 52 : WLAS

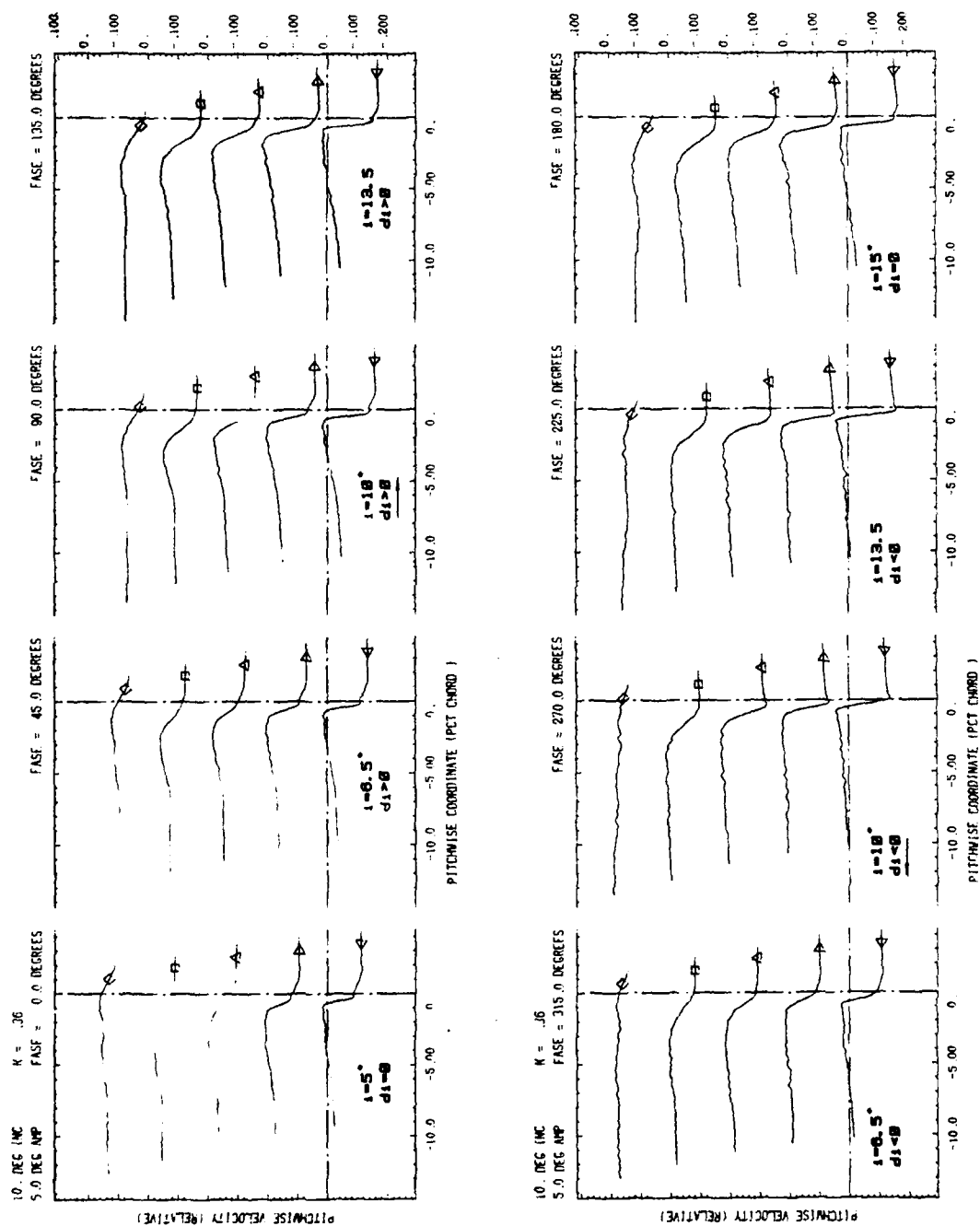


FIGURE 53 : WLAS

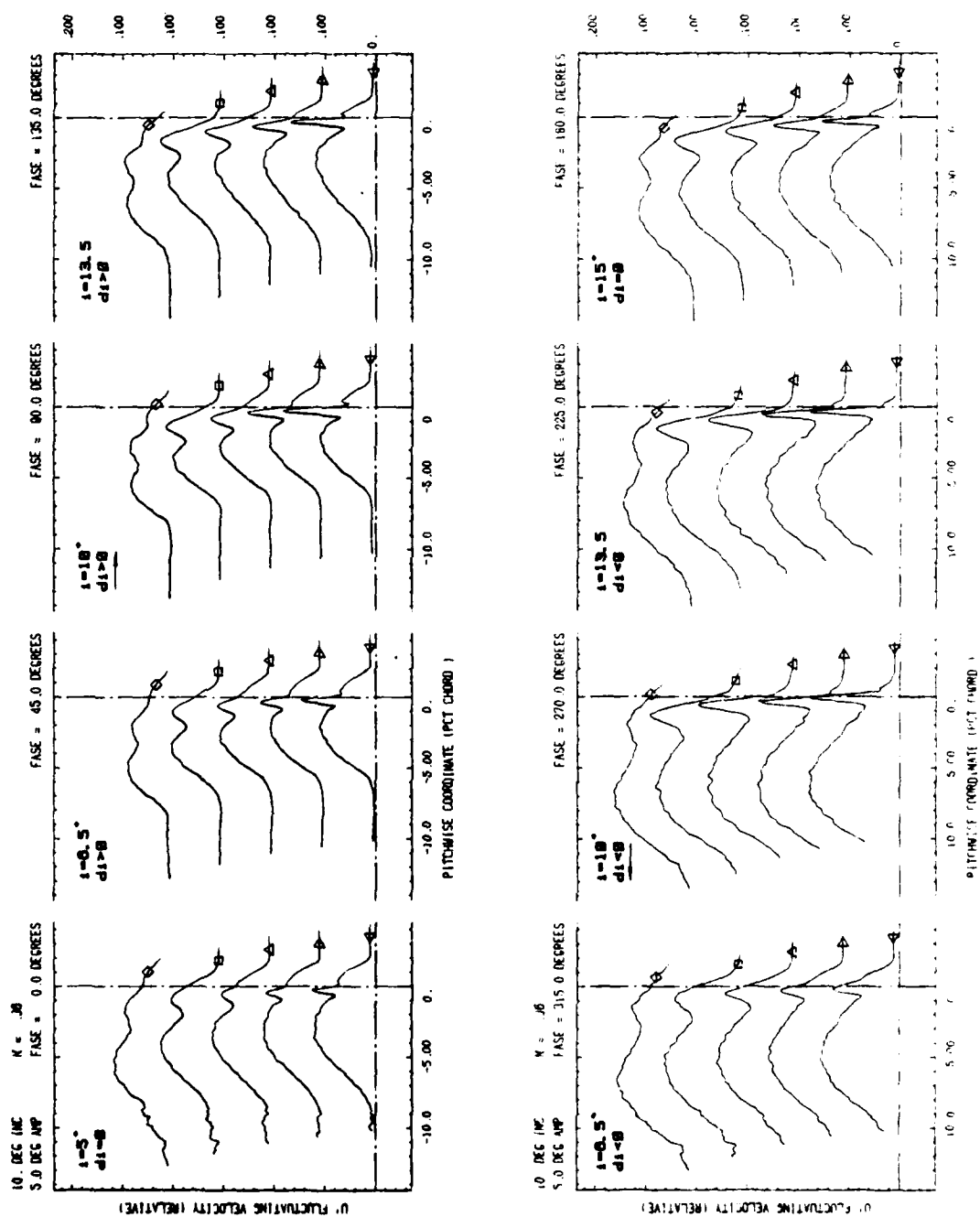


FIGURE 54 : WLAS

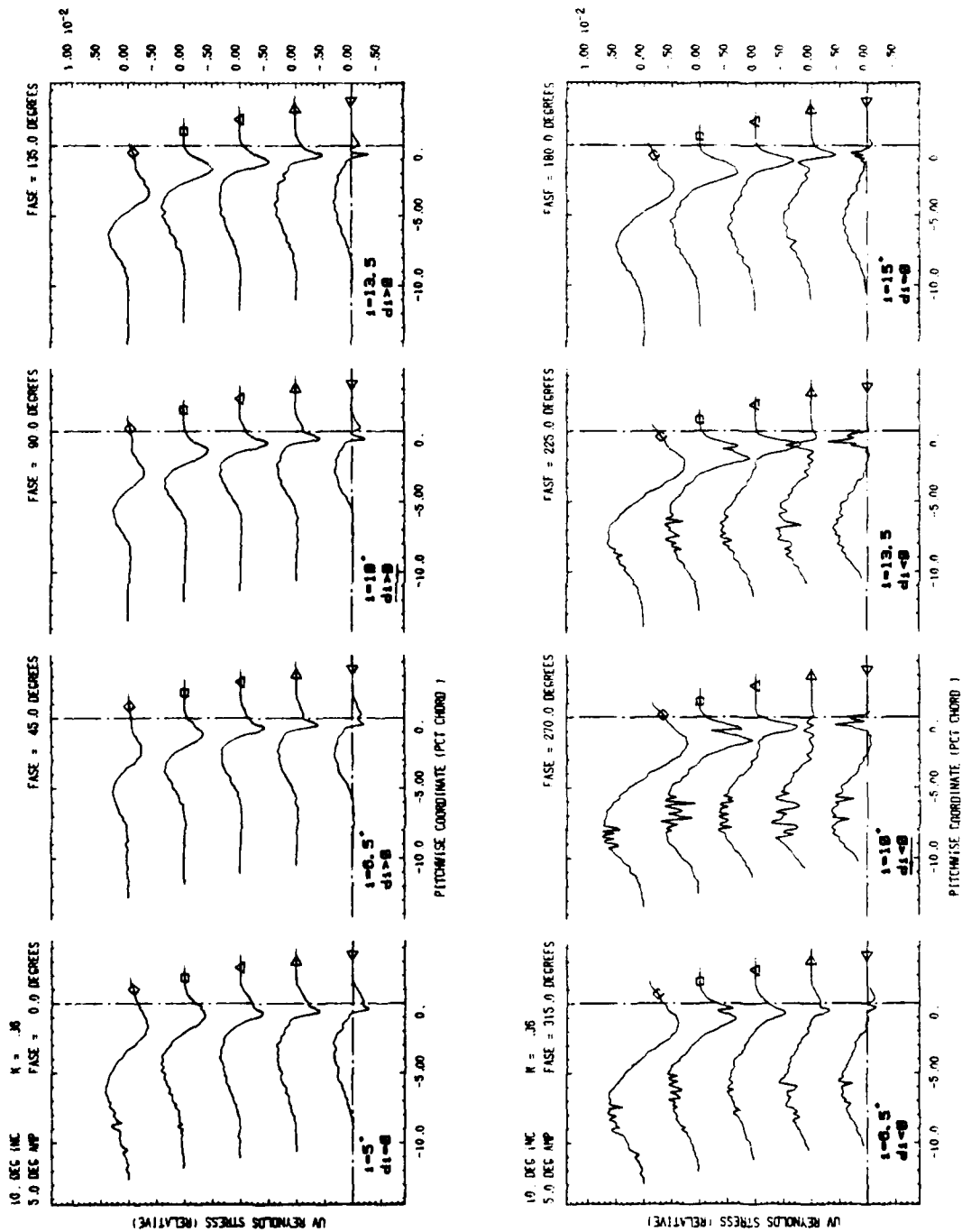


FIGURE 55 : WLA5

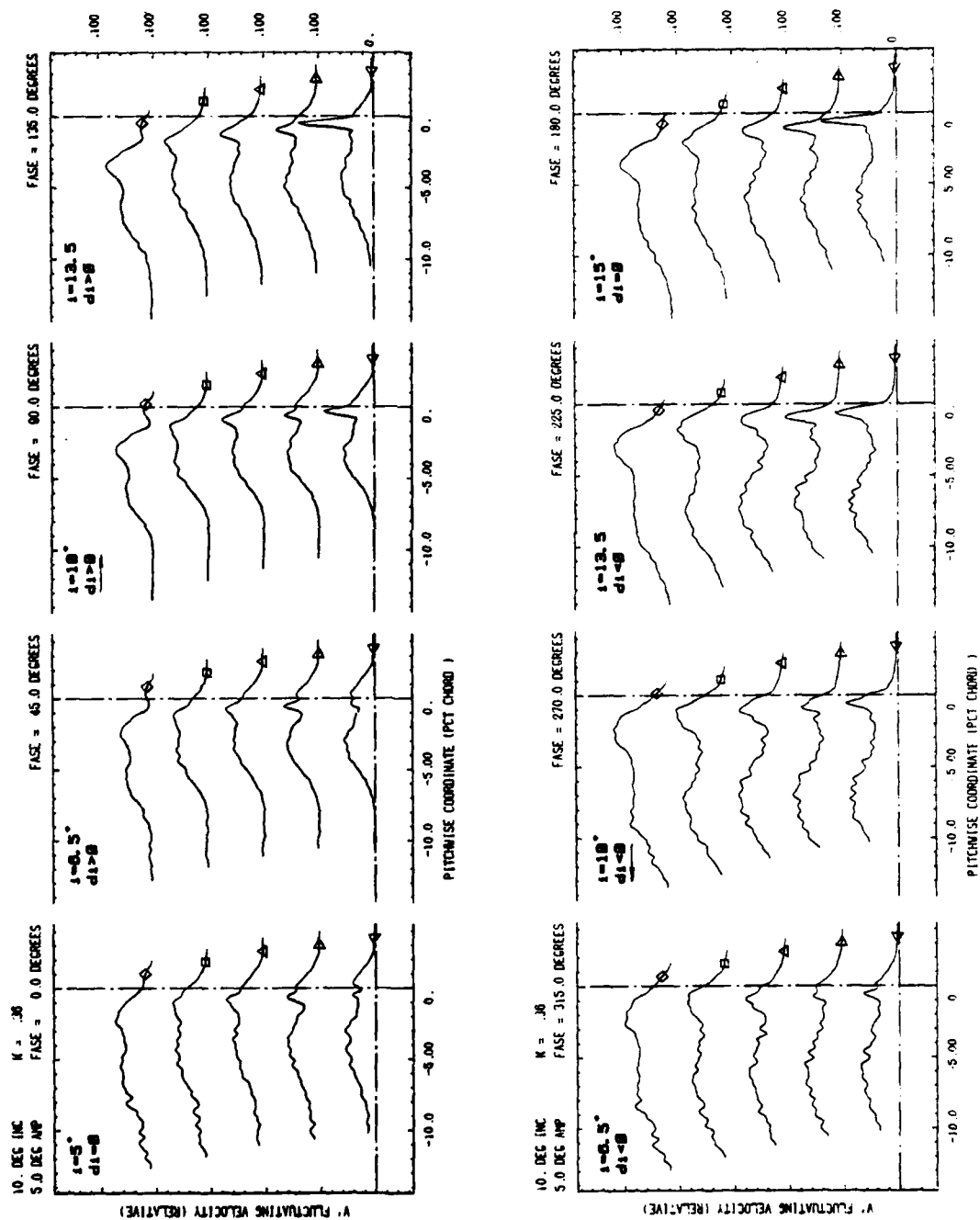


FIGURE 56 : WLAS

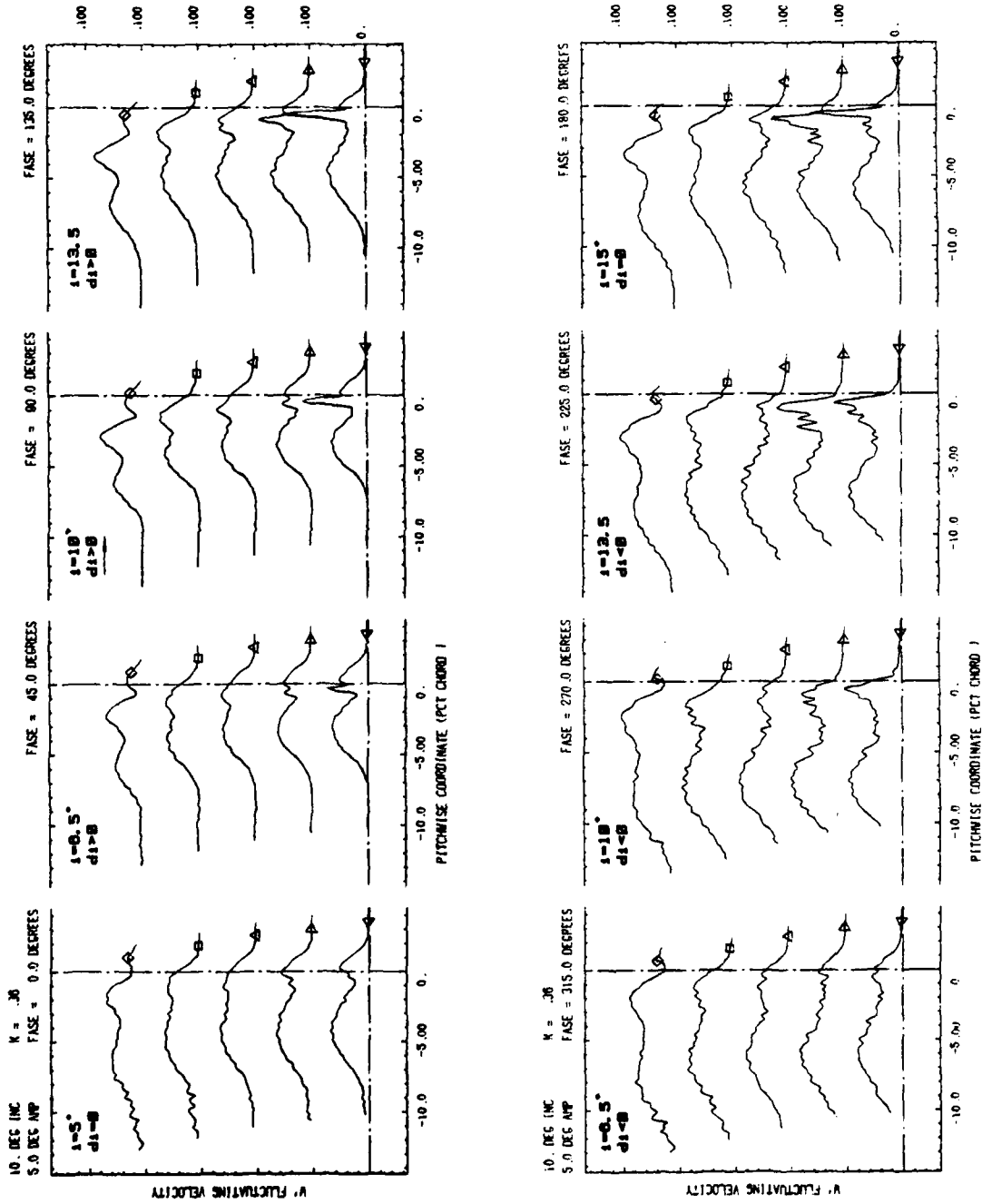


FIGURE 57 : WLAS

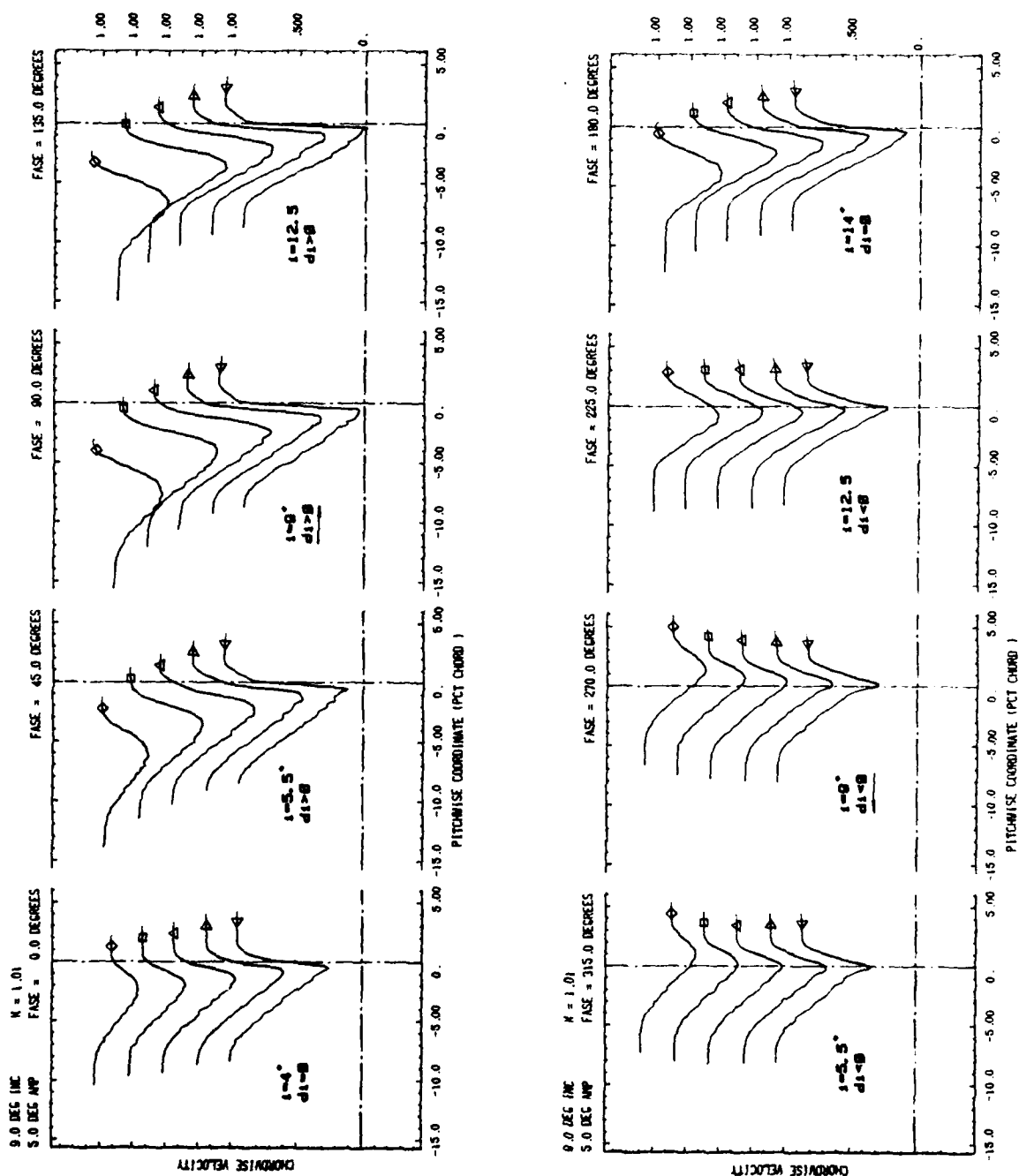


FIGURE 58 : WH95



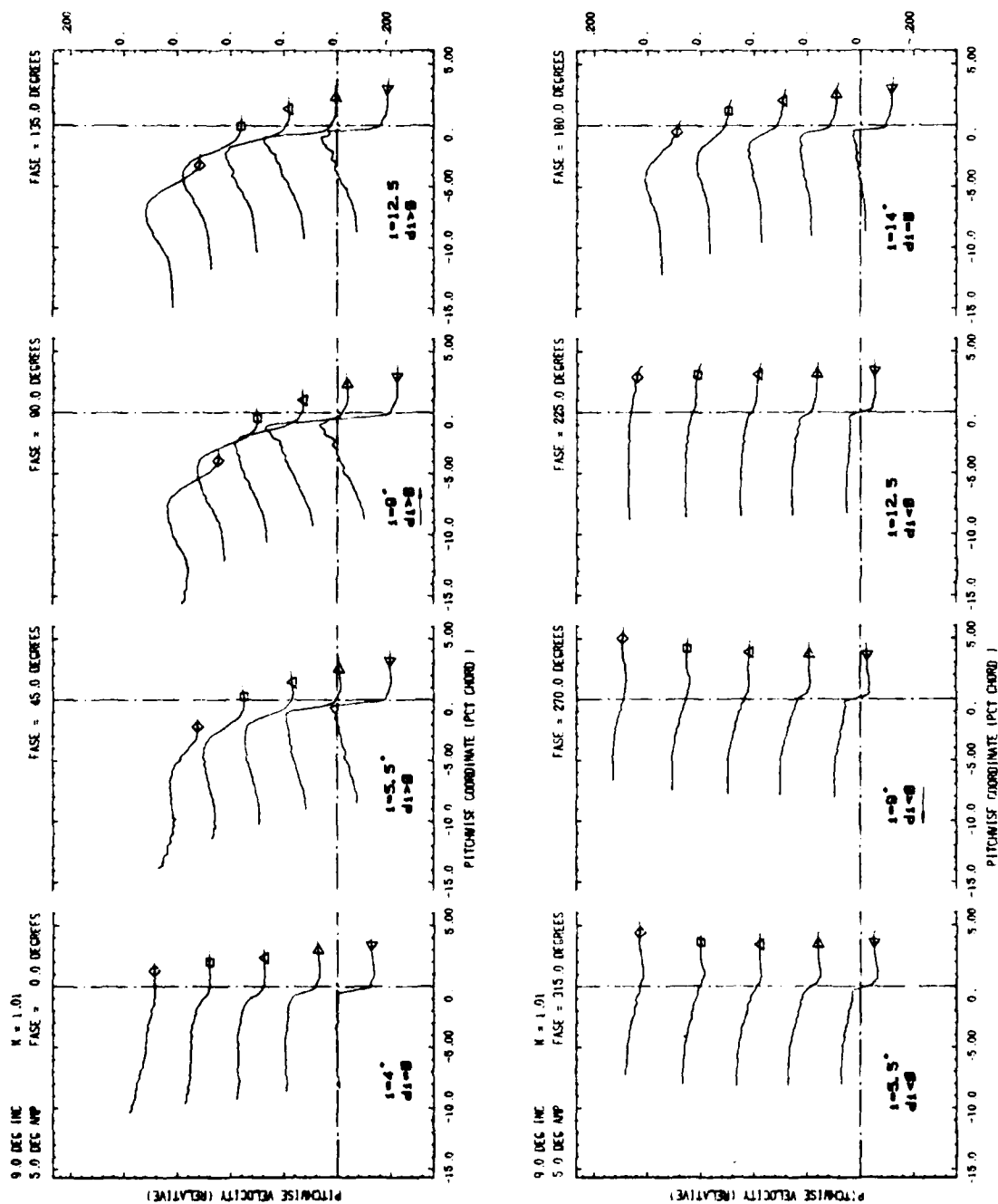


FIGURE 59 : WH95

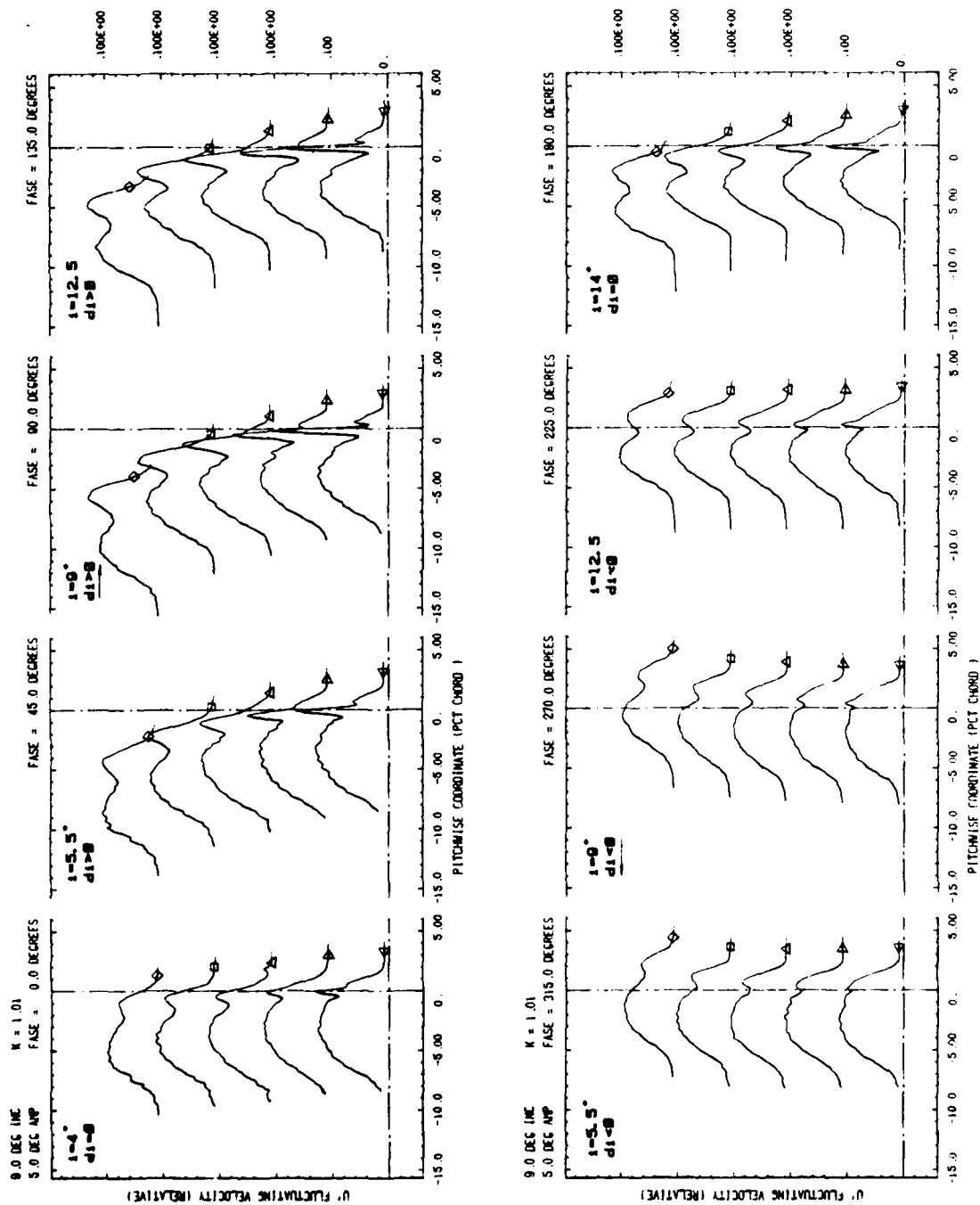


FIGURE 60 : WH95

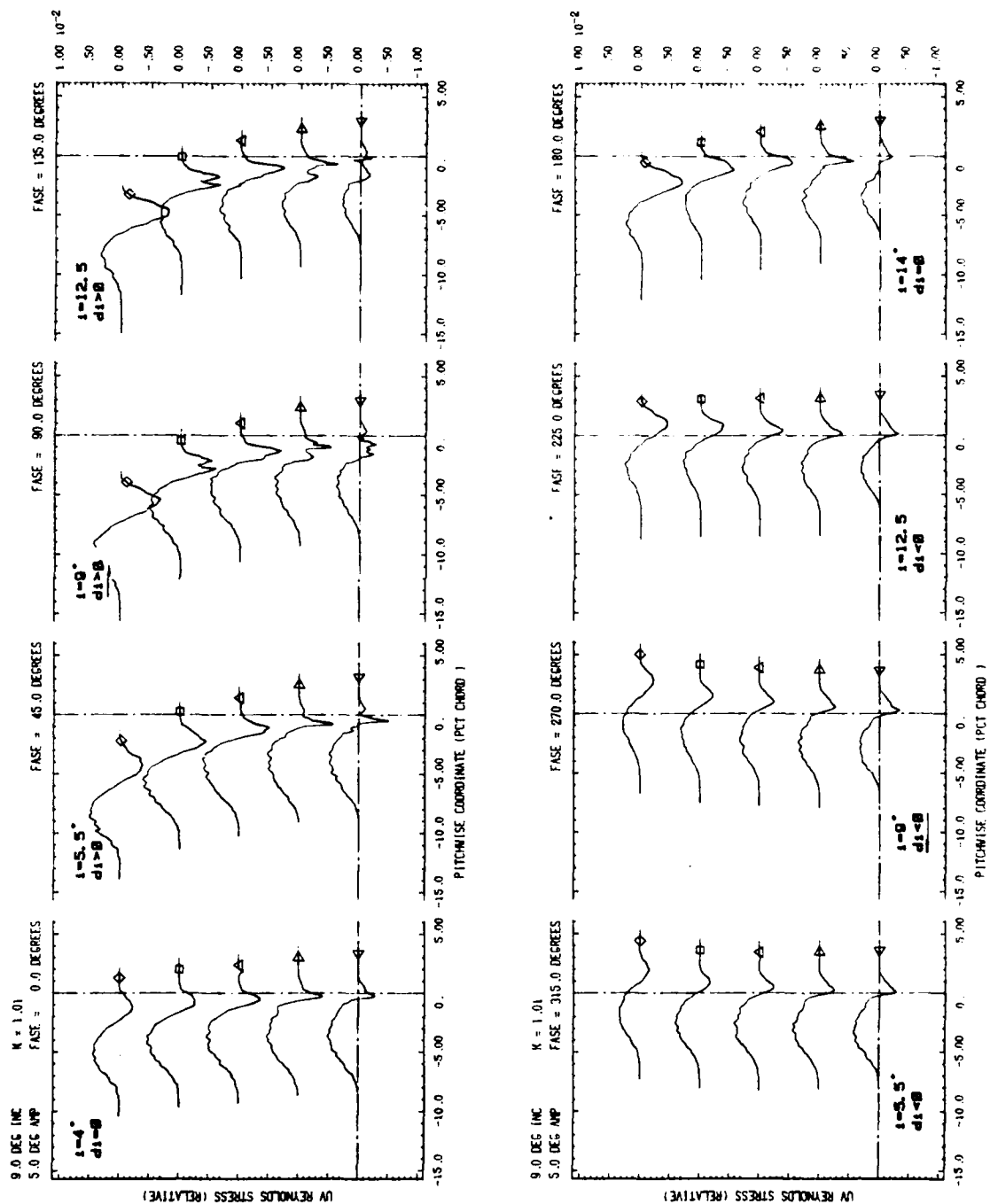


FIGURE 61 : WH95

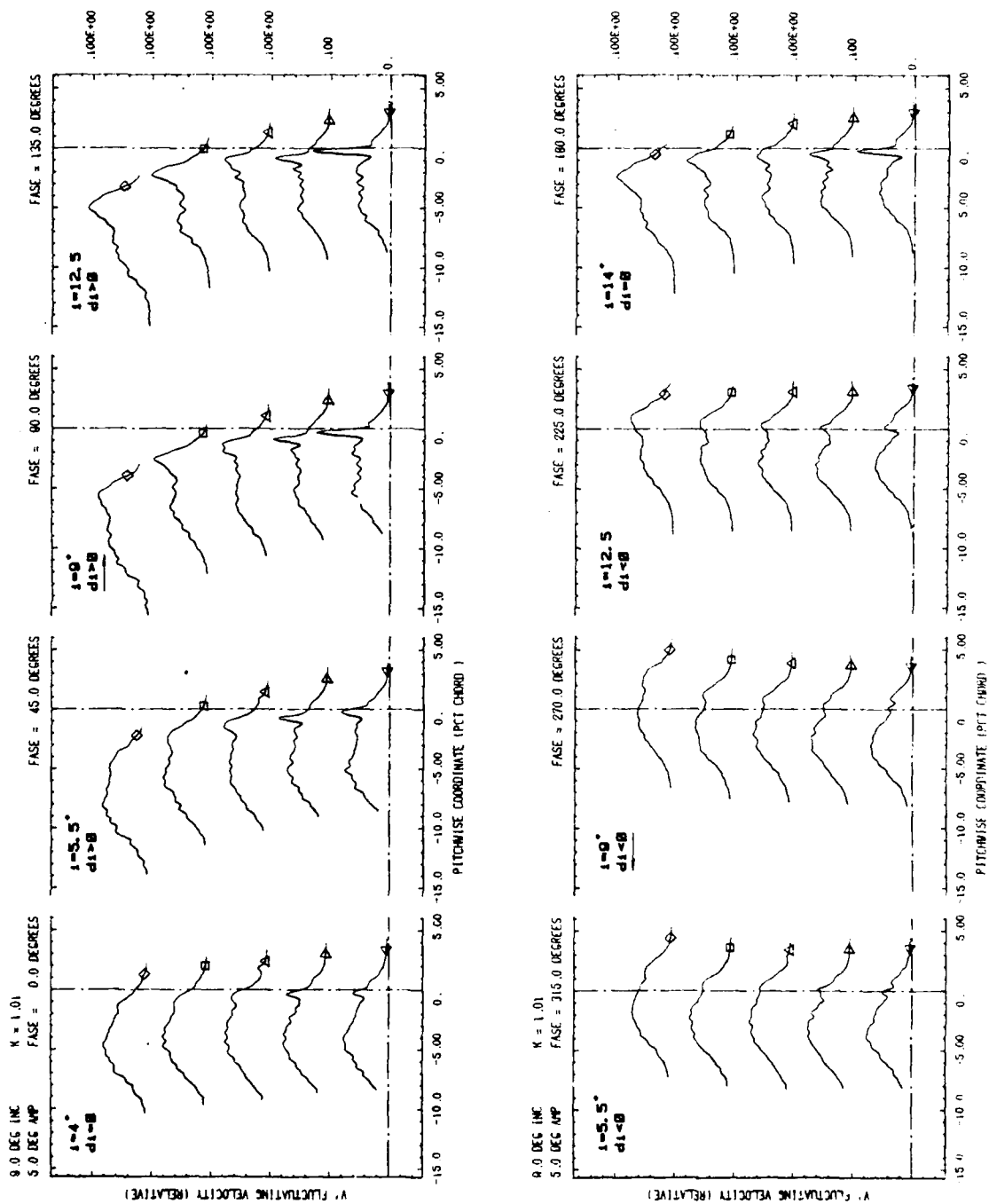


FIGURE 62 : WH95

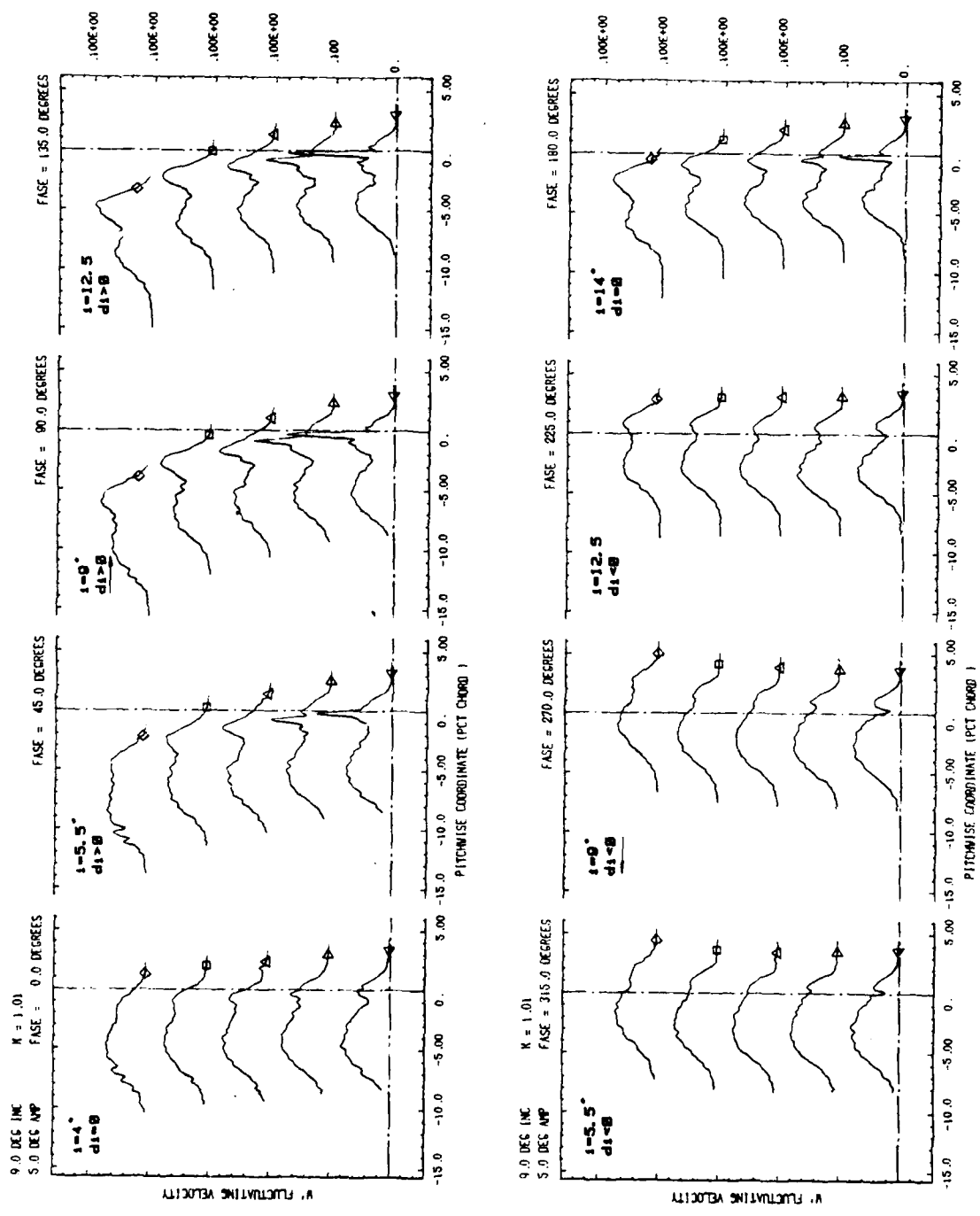


FIGURE 63 : WH95

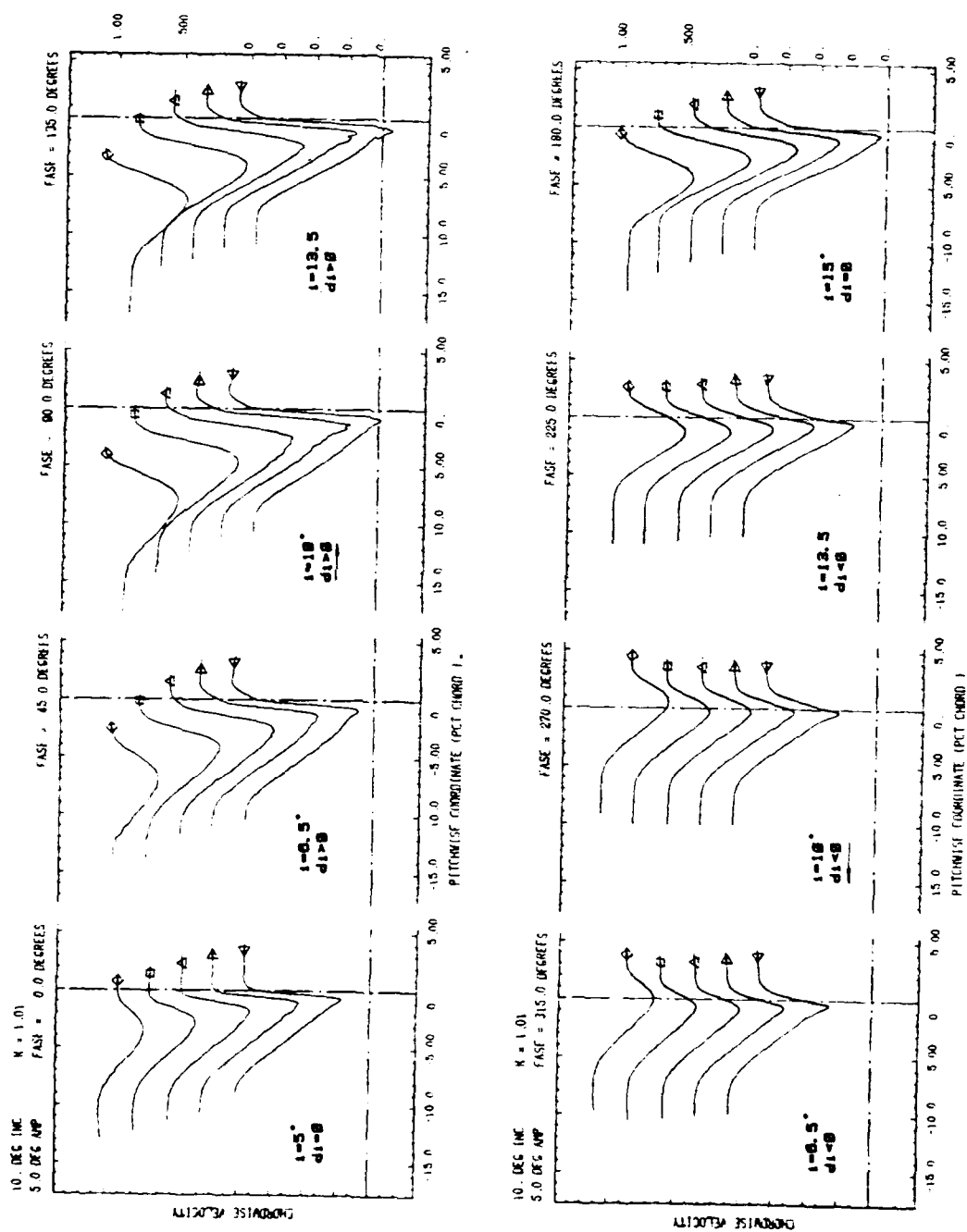


FIGURE 64 : WHAS

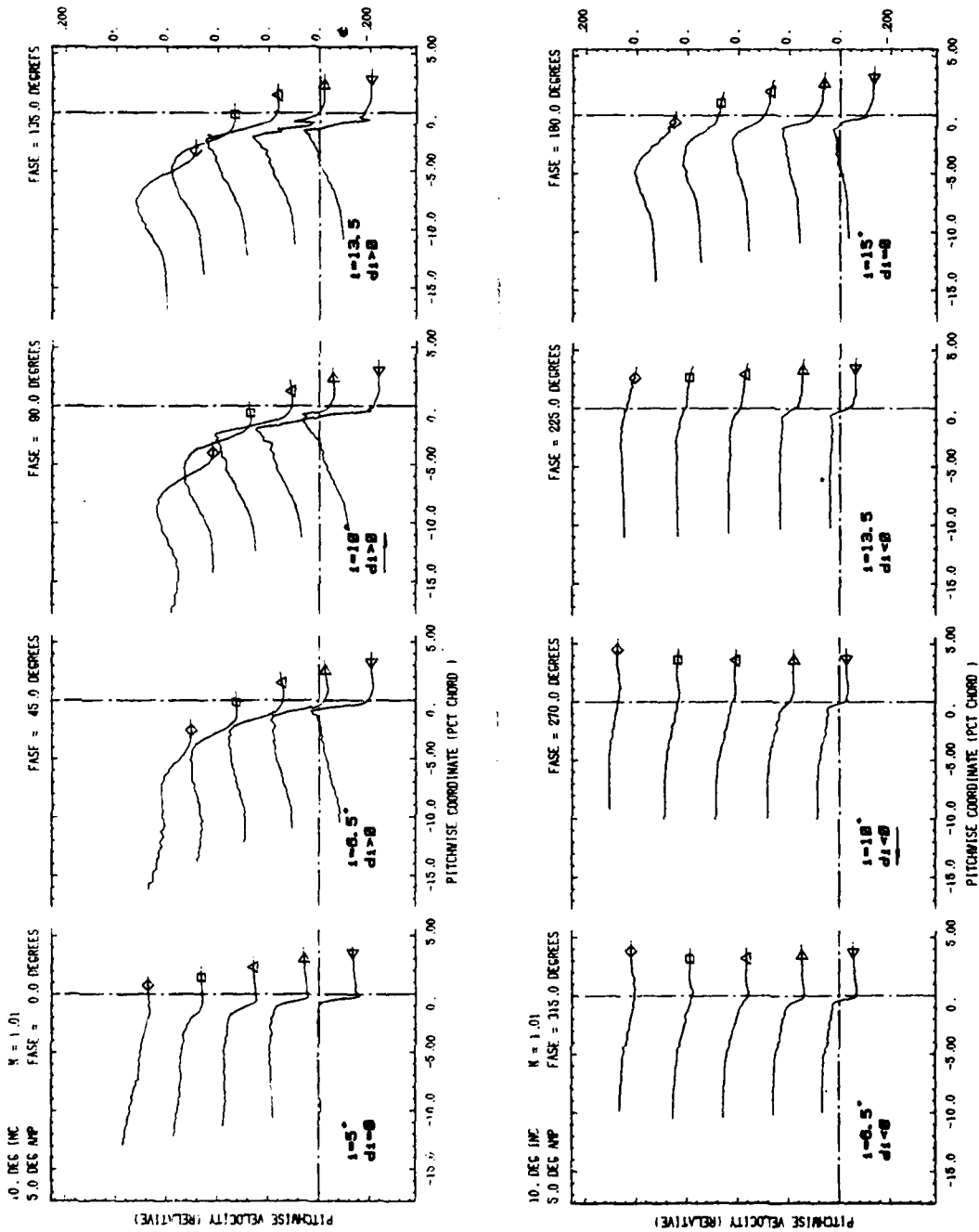


FIGURE 65 : WHA5

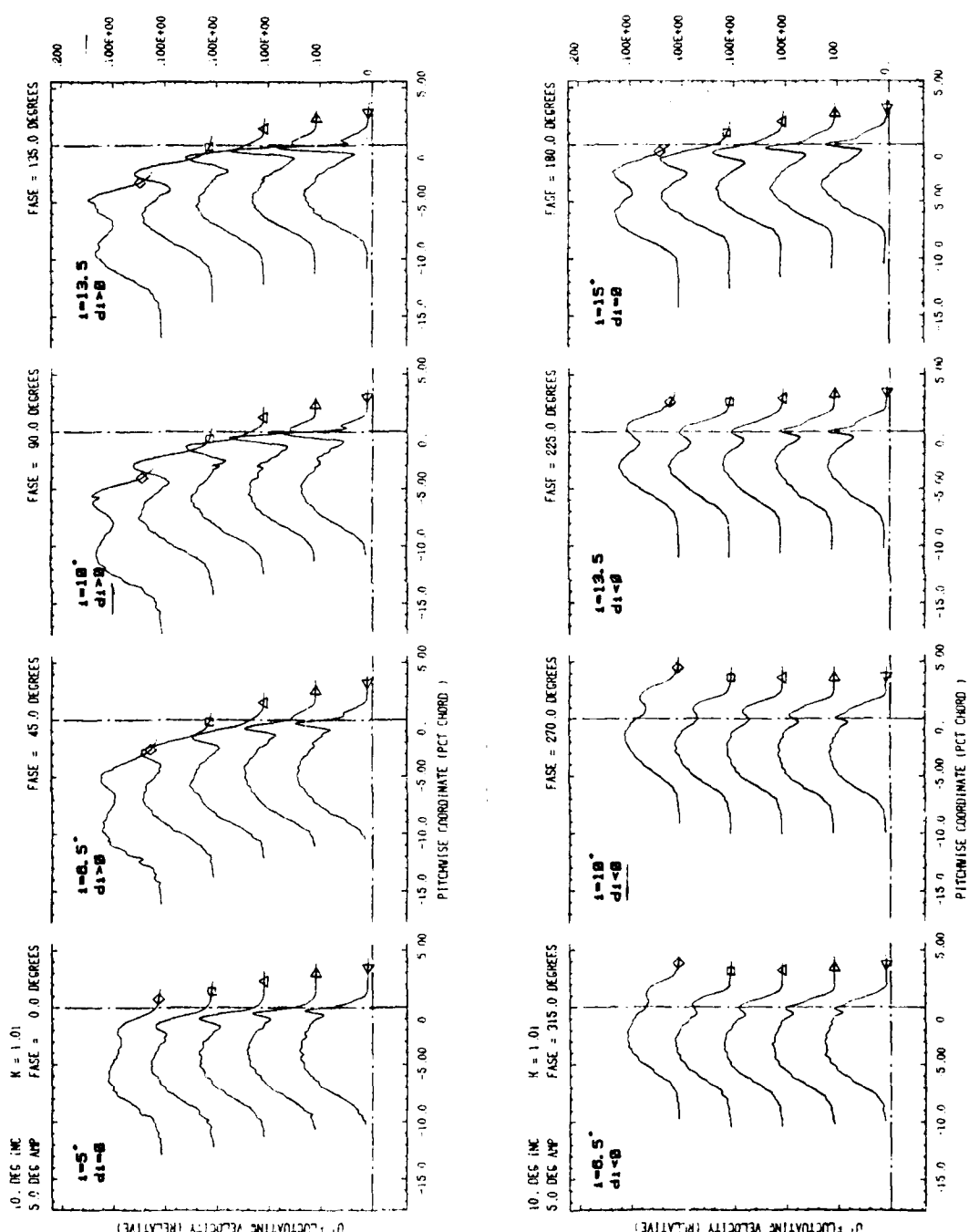


FIGURE 66 : WHAS



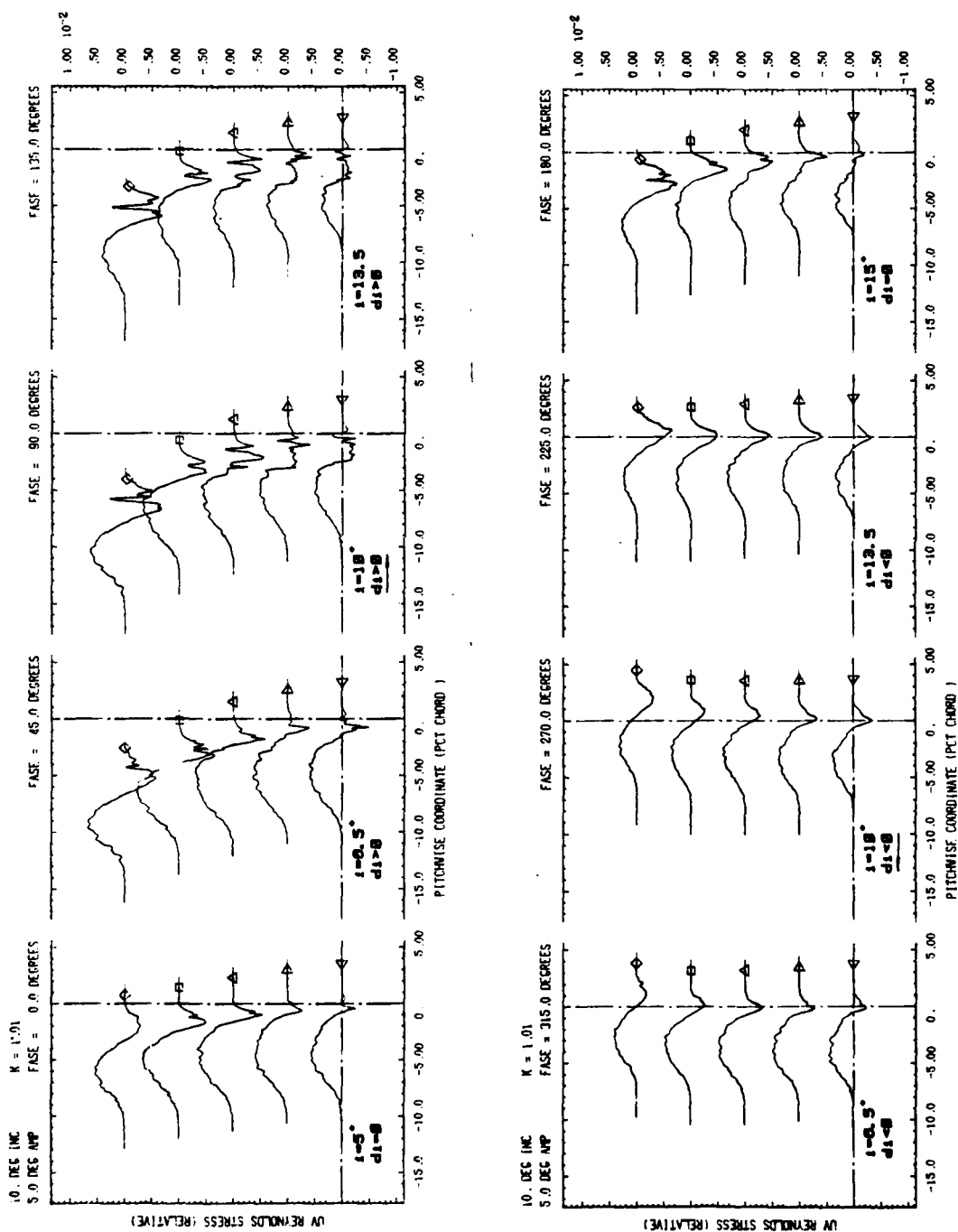


FIGURE 67 : WHA5

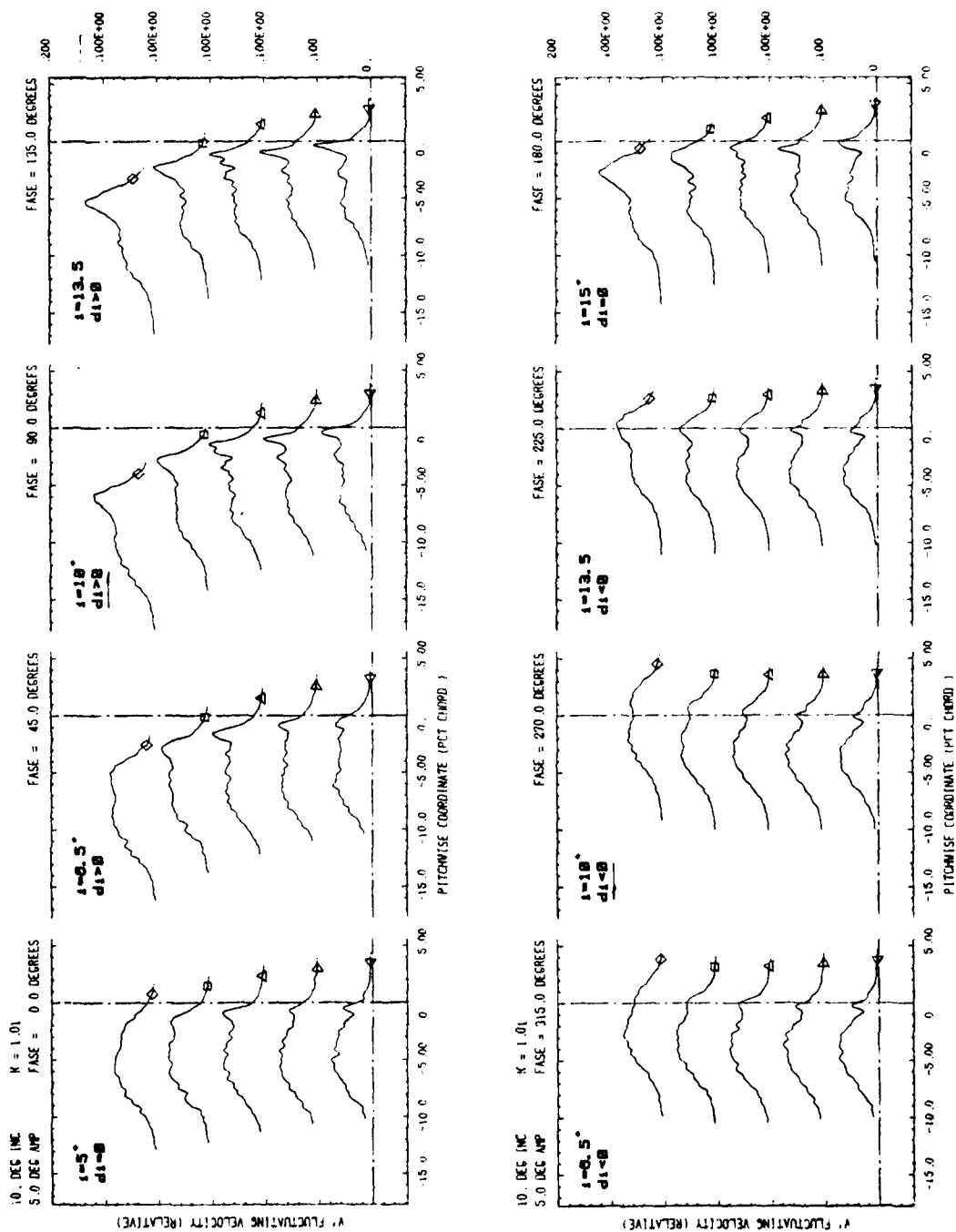


FIGURE 68 : WHA5

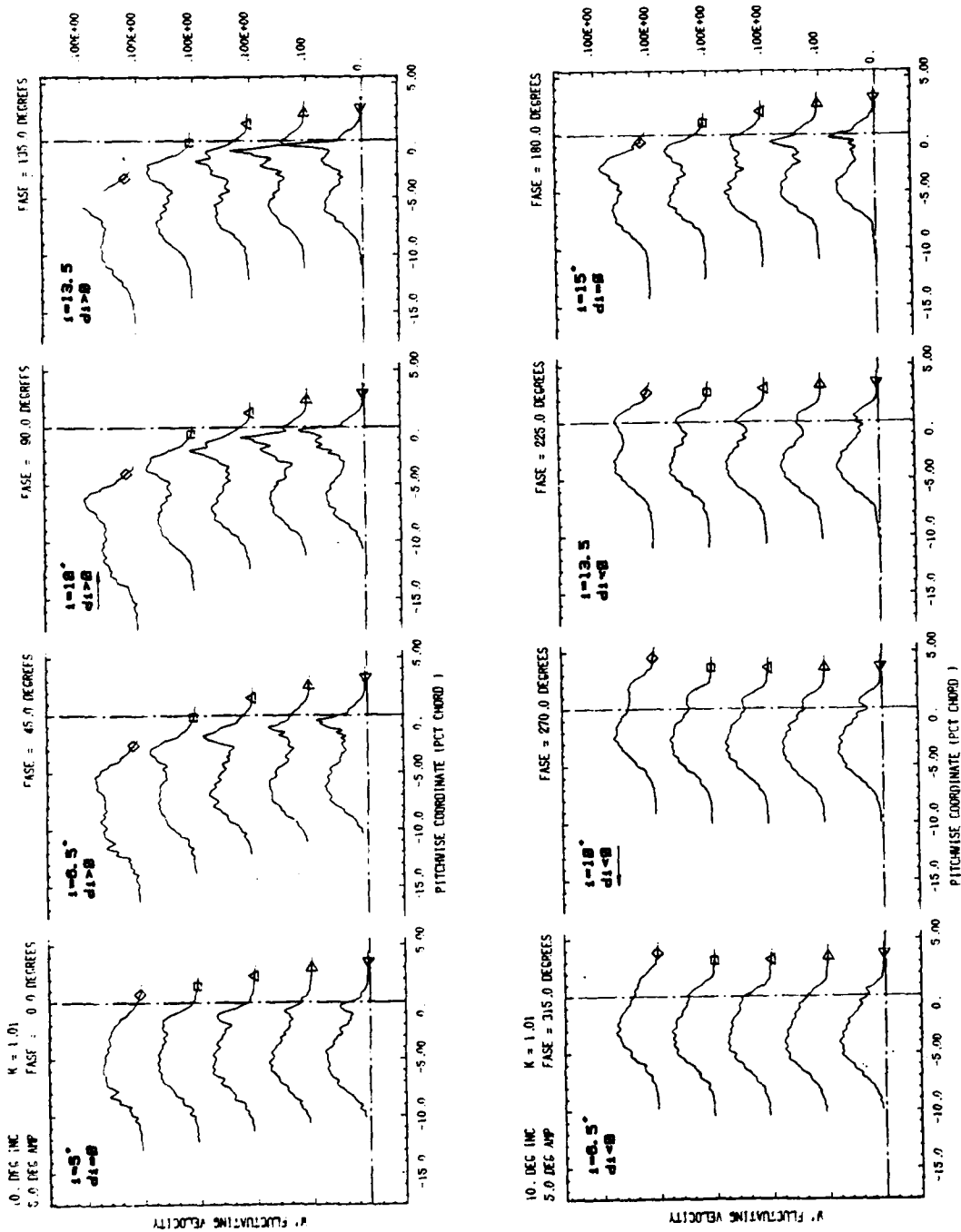


FIGURE 69 : WHA5

